# ARTIFICIAL INTELLIGENCE-BASED INVERSE ANALYSIS OF FLEXIBLE PAVEMENT DETERIORATIONS UNDER MOVING LOADS

A Dissertation

by

YONG DENG

Submitted to the Office of Graduate Studies of
Texas A&M University
in partial fulfillment of the requirements for the degree of

DOCTOR OF PHILOSOPHY

| | |
|---|---|
| Chair of Committee, | Robert L. Lytton |
| Committee Members, | Bjorn Birgisson |
| | Charles Aubeny |
| | Theofanis Strouboulis |
| Head of Department, | Robin Autenrieth |

August 2020

Major Subject: Civil Engineering

# ABSTRACT

Fatigue damage and aging are two typical deterioration modes in flexible pavements. Fatigue damage is mainly caused by load repetitions. It results in the degradation of pavement materials and structures which significantly influences the riding quality and safety, and reduces the service life of pavements. As the loading application continues, microcracks in the asphalt layer initiate, develop and connect to form visible macrocracks. Macrocracks further deteriorate to potholes, which finally result in the moisture infiltration, the loss of strength and durability of the pavement. To avoid such problems, fatigue damage should be controlled before macrocracks form. An indicator to reflect the current deterioration condition of the pavement and provide an advance warning of the pavement failure is necessary.

Aging of flexible pavements is caused by physical and chemical processes in asphalt layers such as the oil volatilization, oxidation and steric hardening etc. Asphalt mixtures closer to the pavement surface are more susceptible to aging and have higher modulus. It is one essential reason to explain the modulus gradient in asphalt layers. Flexible pavements suffering from aging tend to deteriorate in terms of cracking such as the fatigue cracking and thermal cracking. Therefore, an effective method to evaluate the aging degree of a flexible pavement is also necessary.

By reviewing current technologies in determining degrees of fatigue damage and aging in flexible pavement materials and structures, motivations and objectives of this research are identified. The dissertation aims to propose methodologies in evaluating

these two deteriorations in flexible pavements from pavement responses under moving loads or equivalent dynamic loads, which benefit from fast developing nondestructive testing devices. To achieve this goal, the finite element model updating incorporating surrogate models and artificial intelligence algorithms were applied in the equivalency of moving vehicular loads and stationary dynamic loads, calibration of layer moduli, etc. Deteriorations in flexible pavements can be directly determined from field testing and information recorded in the database as well.

DEDICATION

To my parents

# ACKNOWLEDGEMENTS

I would like to express my deepest appreciate to my committee chair, Dr. Robert L. Lytton, for his invaluable support and guidance throughout my graduate studies at Texas A&M University. I have been fortunate to have an advisor who can give me advice whenever I have problems in my research. Also, his passion and academic attitudes will benefit me throughout my future career. It has been a privilege and great pleasure to work with him. I also want to extend my gratitude to my committee members and special guests, Dr. Bjorn Birgisson, Dr. Charles Aubeny, Dr. Theofanis Strouboulis, Dr. Xue Luo and Dr. Yuqing Zhang for their guidance and support throughout the course of this research. I am sincerely grateful to Dr. Xue Luo and Mr. Yazhou Zhang, who selflessly help me during these years. Many thanks go to all my friends and colleagues at Texas A&M University for their precious support and encouragement, which make my time here a great experience. Last but not least, I would like to thank my parents, who receive my deepest gratitude and love for their dedication and these many years of support.

TABLE OF CONTENTS

Page

LIST OF FIGURES

FIGURE Page

FIGURE Page

LIST OF TABLES

TABLE Page

# 1. INTRODUCTION

## 1.1 Background of Fatigue Damage and Aging

Cracking in flexible pavements, based on the contributing factors, can be divided into fatigue cracking and thermal cracking, which are induced by load repetitions and temperature cycling respectively (ARA-ERES, 2004). Fatigue damage, referring to fatigue cracking in this dissertation is a major distress and failure mode of pavements which results in the degradation of pavement materials and structures. Cracks initiate and propagate in the pavement, which finally cause the visible damage and material failure. Fatigue damage significantly influences the riding quality and safety to technicians and drivers, and reduces the service life of pavements (Cocurullo et al., 2008; Moreno-Navarro and Rubio-Gámez, 2016). A comprehensive understanding of the fatigue mechanism of materials and a precise fatigue criterion can play essential roles in the fatigue behavior evaluation and fatigue life prediction, and eventually contribute to the pavement design, maintenance and rehabilitation (Kim et al., 2003).

Aging of flexible pavements is caused by physical and chemical processes in asphalt mixtures such as the oil volatilization, oxidation and steric hardening etc., which increase the stiffness and brittleness of asphalt layers (Li and Nazarian, 1995; Luo et al., 2019). The aging rate and aging degree are mainly controlled by climatological factors such as the ultraviolet radiation, air temperature, precipitation and material properties such as the asphalt binder and air void contents (Hagos, 2008; Yin et al., 2017). Asphalt

mixtures closer to the pavement surface are more susceptible to aging and have higher modulus, which results in the modulus gradient of the asphalt layer.

## 1.2 Problems in Flexible Pavement Deterioration Condition Determination

### *1.2.1 Fatigue Damage*

Over the years, analysis has been conducted on numerous fatigue tests (Di Benedetto et al., 2003; Kim et al., 2003; Cocurullo et al., 2008; Tapsoba et al., 2012; Boudabbous et al., 2013; Ahmed and Khalid, 2015; Poulikakos et al., 2015; Tapsoba et al., 2015; Qabur, 2018) evaluating the fatigue performance of asphalt mixtures, which are the materials of flexible pavement surfaces.

By analyzing test results, a typical method to characterize the specimen in the fatigue test was proposed based on the modulus and the phase angle with load cycles. Three distinct phases were identified according to different curve shapes and explained by different processes within the materials (Tapsoba et al., 2012; Di Benedetto et al., 2003; Poulikakos et al., 2015; Tapsoba et al., 2015; Moreno-Navarro and Rubio-Gámez, 2016). In the first phase, the modulus undergoes a rapid decrease and the phase angle undergoes a rapid increase, which are caused by the heating and thixotropy due to the initial loading process (Di Benedetto et al., 2011). In the second phase, the decrease in the modulus and the increase in the phase angle are quasi-linear with load cycles, which result from the initiation and propagation of micro-cracks. Following that, the coalescence of the micro-cracks creates macro-cracks, which propagate in the third

phase. Both the modulus and the phase angle begin to drop quickly when entering the third phase.

Nowadays, four types of criteria are widely used to evaluate the material condition (Tapsoba et al., 2012) in laboratory fatigue tests:

1. Modulus/Stiffness

The values of modulus and stiffness decrease continuously with load repetitions in fatigue tests. A 50% or 30% decrease in the modulus or stiffness from its initial value is assumed to be the failure of the material (Kim et al., 2003; Tapsoba et al., 2012).

2. Phase Angle

Since the phase angle has its peak value before the macrocracks occur in the material. It can serve as an indicator for the fatigue damage degree of the material. Reese (1997) proposed this criterion based on the phase angle evolution.

3. Homogeneity

With the occurrence of macro-cracks, the material is not homogeneous anymore (Tapsoba et al., 2012). Accordingly, the material responses measured at different locations of the sample vary significantly. The strain amplitude and phase angle were used as the indicators (Tapsoba et al., 2012).

4. Dissipated Energy

The dissipated energy is the energy done by the external work, which is calculated from the area under the strain-stress curve in fatigue tests (Shen et al., 2006). The criterion for the fatigue failure of the material were defined based on the change in

the evolution of the dissipated energy (Pronk and Hopman, 1991) or the dissipated energy ratio (Carpenter et al., 2003) with load cycles.

In flexible pavements, considering the variety of distress modes and the complexity of intrinsic mechanism, studies on fatigue cracking are conducted from individual distress modes or overall pavement performance. For an individual distress mode, fatigue cracking is evaluated either from field measurements directly or a mechanistic-empirical (ME) model developed from intrinsic mechanism, laboratory tests and field measurements (Zhou et al., 2016; Luo et al., 2018b; Lytton et al., 2018; Ling et al., 2019a; Ling et al., 2019b; Luo et al., 2019; Ling et al., 2020). Indicators representing the deterioration condition are very specific. The crack depth, for example, is typically used in the top-down cracking model to represent the current condition and predict the remaining service life of the pavement. On the other side, the overall pavement performance used in the deterioration determination benefits from fast developing in-situ testing technologies. Representative indicators are the deflection, friction and roughness (Elbagalati et al., 2016; Susanna et al., 2017). Sometimes the modulus reduction can be used as an indicator of fatigue damage as well (Collop and Cebon, 1996).

The fact is that indicators in the first category (individual distress mode) are always associated with the final phase where pavement deteriorations are quite severe. While indicators in the second category (overall pavement performance) such as the modulus are sensitive to the temperature and loading frequency, which are two specific factors bothering the analysis and design of flexible pavements.

### *1.2.2 Aging*

Current methods to characterize aging effects can be summarized as comparing material compositions and mechanical properties before and after some level of aging (Li and Nazarian, 1995). For asphalt binders, the carbonyl content or carbonyl area (CA) measured from the Fourier Transform Infrared Spectroscopy (FTIR) test can serve as an indicator of the aging degree since the measured sulfoxide is the product of the sulfur oxidation (Petersen et al., 1993). The Gaestel Index (GI) is then used to quantify the relative amounts of saturates, asphaltenes, aromatics and resins in asphalt binders. The gel-permeation chromatography (GPC) test can measure the molecular size distribution change in asphalt binders. They are representatives to characterize aging effects in terms of material compositions (Oliver, 2009; Lee et al., 2009). Indicators such as the retained penetration, viscosity, ductility, dynamic modulus, phase angle, tensile and creep strength of asphalt binders are also significantly affected by aging and used to evaluate the aging degree (Hagos, 2008). For asphalt mixtures, modulus tests and fatigue tests can characterize aging effects on viscoelasticity, stiffness and fatigue performance of asphalt mixtures (Baek et al., 2012).

Recently, a direct tension test designed for the complex modulus of asphalt mixtures (Luo and Lytton, 2010) was modified to characterize the modulus gradient of asphalt mixtures (Koohi et al., 2012; Ling et al., 2017a; Ling et al., 2017b). In the test, six linear variable displacement transducers (LVDT) were placed to measure vertical displacements at the surface, center and bottom of the rectangular specimen. Despite that the tensile load was applied at the centerline of the specimen, the nonuniform stiffness

distribution due to aging resulted in distinct strain responses at three locations. Complex modulus gradient of the asphalt mixture caused by aging was obtained from test results (Koohi et al., 2012; Ling et al., 2017b).

Based on the studies introduced above, several models characterizing and predicting aging effects have been proposed and implemented into the pavement design and evaluation frameworks. In the Global Aging System, aging time, air void content, air temperature and pavement depth are model parameters to characterize both short-term and long-term aging effects on the binder viscosity (Mirza and Witczak, 1995). The viscosity can be further incorporated into models determining the dynamic modulus of asphalt mixtures in the Pavement ME Design Guide (ARA-ERES, 2004). Besides, the morphology-based aging model (Das, et al., 2015), kinetics-based aging model (Luo et al., 2015; Luo et al., 2019; Zhang et al., 2019a; Luo et al., 2020) and their combination (Zhang et al., 2019b) were proposed to interpret and predict aging effects on asphalt mixtures and flexible pavements. Aging time, air void content, air temperature and pavement depth are always indispensable factors.

In these methods, the aging condition was either simulated in the laboratory or considered in field cores. In AASHTO Provisional Protocols PP1-98 and PP2-99 (AASHTO, 1999), test procedures to simulate aging conditions for asphalt binders and asphalt mixtures are specified. Pressurized air and elevated temperature are applied to accelerate the aging process in order to simulate both short-term and long-term aging as in the field (Ling et al., 2017a). The limitation of simulating aging conditions in the laboratory is that certain processes such as the precipitation and ultraviolet radiation

cannot be reproduced in the laboratory (Houston et al., 2005). Alternatively, materials from the field can be used directly. In addition to the direct tension test which is conducted on field cores, binders can be extracted from field cores following the standard (ASTM, 2017) and then used for the aging characterization. Apparently, these methods cause damages to pavements. An ideal methodology to characterize aging effects in asphalt layers of flexible pavements should be nondestructive and straightforward (Li and Nazarian, 1995).

### 1.3 Problems in Applications of Nondestructive Testing

The nondestructive (NDT) testing devices applied to evaluate flexible pavement conditions can be divided into two categories according to their applied loads. The most common NDT device is the Falling Weight Deflectometer (FWD) which applies stationary dynamic loads. Typically, the dynamic load with the load magnitude 40 kN and the duration 0.03 s is delivered by a circular loading plate of 0.15 m in radius. It is dropped to the pavement surface while the vertical deflections are recorded by the sensors mounted along the centerline direction of the loading plate. The FWD is of wide applications for the variety of the information it collects. For example, the deflection peaks at different sensor locations can be seen as direct indicators of the pavement strength and used to calculate indices evaluating pavement structural conditions (Elbagalati et al., 2017). In flexible pavements, the load and deflection histories can be used to backcalculate the time/frequency-dependent moduli of pavement layers (Lytton 1989). Structural and material parameters such as the layer thickness (Terzi et al., 2013;

Sangghaleh et al., 2014), the Poisson's ratio (Saltan et al., 2011) and the nonlinearity of supporting layers (Li and Wang, 2019) can be obtained from FWD tests as well.

The second load type is the moving vehicular load. As the name implies, the testing devices move along pavements as traffic vehicles. Moving vehicle loads ideally represent the loading conditions of pavements in service life. Typically, they can be characterized by contact stresses between the pavement surface and rolling tires, which are significantly affected by the weight, the moving speed and the tire configuration of the vehicle (Wang and Al-Qadi, 2009). Representative devices are the Rolling Wheel Deflectometer (RWD) and the Traffic Speed Deflectometer (TSD). In RWD tests, the pavement deflects under a standard 80-kN (18-kip) load induced by the dual-tire at the rear single axle of a semitrailer which can move at a speed up to 105 km/h (65 mph) (Steele and Vavrik, 2004; Carlson et al., 2017). The pavement deflections measured by laser sensors mounted between tires can be directly used to evaluate the structural capacity of the pavement in terms of the structural number (SN) (Elseifi et al., 2015) and the structural condition index (SCI) (Elbagalati et al., 2017). In TSD tests conducted in US, the nominal rear axle load is 89 kN (20 kips) and the moving speed can be up to 80 km/h (50 mph) (Maser et al., 2017). Different from the RWD, the TSD uses velocity-sensing lasers to measure the vertical pavement deflection velocity and the horizontal vehicle velocity at six locations on the pavement surface (Flintsch et al., 2012). The measured velocities are used to either obtain a deflection basin (Muller and Roberts, 2013; Zofka et al., 2014) or calculate deflection and deflection slope indices (Nasimifar et al., 2016).

Overall, both types of devices have their applications. However, limited researches were conducted on the relationships between the loads they apply or the data they collect. It results in the difficulties in comparisons and validations of these NDT tests. Besides, indices associated with the deflection are applied in both types of tests. Whether conditions of flexible pavements can be evaluated from deflections as in the current practice is questionable. For example, as viscoelastic materials, asphalt layers of flexible pavements are sensitive to the temperature and loading frequency, which vary with the layer depth. Moreover, deflections of flexible pavements are affected by both aging and fatigue damage, of which the effects are opposite. Many issues are required to be addressed before applying NDT devices at the network level of the pavement evaluation, maintenance and rehabilitation.

### 1.4 Research Objectives

The goal of this dissertation is to address the problems mentioned above and propose methodologies in determining fatigue damage and aging degrees in flexible pavements from their responses under moving loads. The research will focus on achieving the following objectives:

- Propose methodologies in simulating flexible pavements under moving vehicular loads and stationary dynamic loads using finite element (FE) simulations and build relationships between them using Artificial Intelligence (AI)-based finite element updating;

- Simulate flexible pavements at different degrees of fatigue damage and propose a potential indicator for the fatigue damage degree from pavement responses under moving vehicular loads and equivalent stationary dynamic loads;
- Propose methodologies in determining the aging degree of flexible pavements from pavement responses in NDT tests; and
- Propose methodologies in determining the deterioration degree of flexible pavements from information recorded in an open database and discuss the modulus and associated terms in evaluating flexible pavement conditions.

## 1.5 Dissertation Outline

This dissertation is organized as follows:

Section 2 first presents simulations of flexible pavements under moving loads using 3D FE models. The simulation procedures for pavement structures, materials, tire configurations, distributions and movements of contact stresses are introduced. 3D FE models are applied to represent flexible pavements in RWD and TSD tests. Similarly, simulations of flexible pavements under stationary dynamic loads using 2D axisymmetric models are then introduced, which aim for flexible pavements in FWD tests.

Load characteristics and pavement responses in FE models provide necessary inputs and outputs for the relationship between moving vehicular loads and stationary dynamic loads. The FE model updating implemented with AI algorithms makes the relationship built in an intelligent and efficient way, which is also included in Section 2.

With this relationship, deterioration conditions of flexible pavements can be evaluated from their responses under either moving vehicular loads or equivalent stationary dynamic loads.

In Section 3, an indicator is defined from flexible pavement responses under moving vehicular loads and equivalent stationary dynamic loads for the fatigue damage degree. Required information for the indicator can be obtained from NDT tests on real pavements. The basic idea of the indicator along with its sensitivities to the fatigue damage degree, load characteristics and layer properties of pavements are discussed then.

Section 4 starts from descriptions of complete time histories of FWD loads and their transformations into the frequency domain via the Fast Fourier Transformation (FFT). Following that, a calibration method for the modulus gradient in the asphalt layer of flexible pavements is proposed. The aging degree of flexible pavements can be then obtained from calibrated modulus gradients.

In Section 5, the deterioration degree of flexible pavements is determined from an open database and a series of calibration processes. A comprehensive consideration of factors affecting behaviors of flexible pavements such as the temperature and loading frequency is achieved in the proposed method. Some issues in current evaluations of flexible pavement conditions are discussed and addressed.

Section 6 summarizes main findings and contributions of the work in this dissertation. Suggested directions of future researches and applications of proposed methods are also listed.

# 2. DEVELOPMENT OF EQUIVALENT RELATIONSHIP BETWEEN MOVING VEHICULAR LOADS AND STATIONARY DYNAMIC LOADS

## 2.1 Current Researches on the Equivalent Relationship between Moving Vehicular Loads and Stationary Dynamic Loads

The main purpose of the equivalent relationship between moving vehicular loads and stationary dynamic loads is to connect two types of NDT devices and FE models. Currently, no overwhelming evidence indicates one type can totally replace the other in the practice. Compared with stationary dynamic loads, pavement responses such as stresses, strains and deflections under moving vehicular loads should be more representative for the pavement condition in service. Also, with higher production and no interruption to the traffic, NDT devices applying moving vehicular loads significantly improve the safety to technicians and costs of the pavement rehabilitation and maintenance. However, factors limiting their applications are the accuracy and stability. With high speeds, random noise accompanies the data collected by the RWD and the TSD (Flintsch et al., 2012). Therefore, in the current network-level projects, only averaged deflections and deflection slopes over a certain length are utilized to evaluate pavement conditions. Meanwhile, obtained information such as maximum deflections and deflection slops from the RWD and the TSD are recommended to compare with those from the FWD to check the accuracy and stability.

In a previous research (Elseifi et al., 2011), both the FWD and the RWD were used on the same pavement to compare their collected deflections. The moving speeds of

the RWD were 32 km/h, 48 km/h, 64 km/h, 80 km/h and 96 km/h. Significant discrepancies between two devices were observed as expected. It was found that deflections collected from the RWD were at a similar level with deflections from the FWD when the moving speed was 80 km/h. Other methods to correlate the FWD and the RWD such as theoretical models (Madsen and Pedersen, 2019) and statistical models (Gedafa et al., 2012) were applied as well, in which the deterioration rank or the deflection variation (Elseifi et al., 2011) served as indicators. Similar issues occurred in the comparison between the TSD and the FWD. In general, no quantitative relationships can be built from field tests. Researchers had to use theoretical models and statistical models which were calibrated and trained by limited test data to validate or predict deflection and deflection slope indices (Katicha et al., 2014; Levenberg et al., 2018).

In addition to measurements from pavements in service, the equivalency between two load types was studied from tests on instrumented pavements, in which pavement responses were recorded by embedded sensors. Loulizi et al. (2002) compared vertical compressive stress pulses within the pavement surface layer induced by the standard FWD load and moving loads with the pressure magnitude 724 kPa and four different speeds (8 km/h, 24 km/h, 40 km/h and 72 km/h). It was found that effects of the moving speed varied with the layer depth. Qin (2010) compared the magnitude and duration of longitudinal tensile stresses at the bottom of the surface layer under the FWD load and moving loads at four different speeds (8 km/h, 40 km/h, 72 km/h and 88 km/h). At the same level, the moving load at the speed 88 km/h caused similar strain magnitude as the FWD load. However, strain durations caused by moving loads were longer than those by

the FWD load. Leiva-Villacorta and Timm (2013) compared loading pulses of the FWD load and the moving load. Measured loading pulse of the moving load at 72 km/h was two to three times longer than those of the FWD load.

As alternative tools to evaluate and predict pavement conditions, FE models can provide pavement responses with reliability and consistency. Therefore, stationary dynamic loads and moving vehicular loads are also applied and compared in the pavement FE models in current researches. The model type can either be three-dimensional (3D) or two-dimensional (2D) axisymmetric. 3D models ideally represent pavement structures in service conditions in terms of the structural configuration, the movement of traffic/test loads (Wang and Al-Qadi, 2012) and nonuniformity of contact stresses between tires and the pavement surface (Wang and Al-Qadi, 2009). Pavement responses from 3D pavement FE models with moving loads have been validated with field tests and used to evaluate pavement deteriorations (Wang and Al-Qadi, 2010a).

2D axisymmetric models are typically applied to represent pavements in FWD tests. According to the model assumption, 2D axisymmetric models actually represent cylindrically shaped structures. The movement of loads cannot be achieved and the model size has to be adjusted to eliminate boundary effects (Kim, 2007; Li et al., 2017). However, they have limited effects on FWD tests, in which loads are stationary and uniformly distributed on a circular loaded area. Pavement responses from 2D axisymmetric FE models with the FWD load are also used to evaluate pavement conditions based on a common assumption that the standard FWD load can induce similar responses as traffic loads at highway speeds (Wang and Li, 2016). Moreover, 2D

axisymmetric models require much less storage space and computational time compared with 3D models (Kim, 2007).

A comprehensive comparison between FWD loads and moving vehicular loads was conducted using FE models (Wang and Li, 2016). Several conclusions were drawn from this study. The first one was that by comparing the compressive stress duration, the equivalent relationship between FWD loads and moving loads was affected by the pavement structure, layer depth and environment conditions. The second one was that the relationship aiming for compressive stress durations was not valid when applied in other responses such as the tensile and shear strains. Similar findings were presented in other researches (Al-Qadi et al., 2008; Ulloa et al., 2013). The third one was that at the similar load level, the FWD load cannot represent highway-speed moving loads in terms of the tensile and shear strains at critical locations of the pavement. It indicated the assumption only worked for certain pavement structures.

From the studies described above, a clear understanding of the relationship between stationary dynamic loads and moving vehicular loads is of importance and necessity. Such understanding includes quantitative formula correlating characteristics of stationary dynamic loads (load magnitude, load cycle, etc.) and moving vehicular loads (load magnitude, moving speed, etc.). Also, pavement responses the relationship aims for and factors the relationship depends on should be clarified. From the viewpoint of field tests, a solid and targeted relationship makes it possible for direct comparisons between field tests applying stationary dynamic loads and moving vehicular loads. For example, a relationship aiming for the vertical deflection magnitude can directly connect

deflections collected from the FWD and the RWD. The accuracy of the deflection value rather than the rank or variation can be checked. From the viewpoint of FE simulations, 2D axisymmetric FE models with equivalent stationary dynamic loads can replace 3D FE models with moving loads. Similar pavement responses can be obtained but with higher efficiency, which provides much more convenience for rapid pavement evaluation, maintenance and rehabilitation.

## 2.2 A 3D Pavement FE Model with Moving Vehicular Loads

A typical flexible pavement under dual tires of a vehicle is built in the commercial FE software ABAQUS (2012). The geometric parameters and material properties of the pavement are presented in Figure 2.1 and Table 2.1. The flexible pavement consists of three layers: 0.1-m (4-in) surface layer made of asphalt mixtures, 0.15-m (6-in) base layer and 1.78-m (70-in) subgrade. The base and subgrade are assumed to be linear elastic and the surface layer is assumed to be viscoelastic. For viscoelastic materials, ABAQUS applies the Prony series to characterize their time-varying moduli $E(t)$, which is represented in Equation 2.1,

$$E(t) = E_\infty + \sum_{i=1}^{K} E_i e^{-t/\tau_i} \tag{2.1}$$

where $E_\infty$ is the long-term modulus; $E_i$ are Prony series coefficients; $\tau_i$ are relaxation times; and $K$ is the number of Prony series terms.

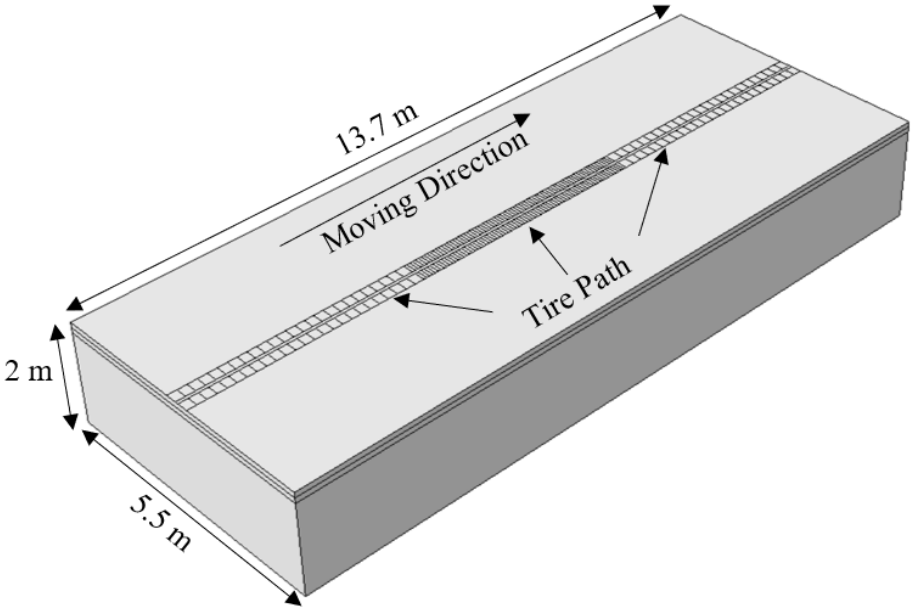


**(a) Geometry of the 3D Pavement FE Model**

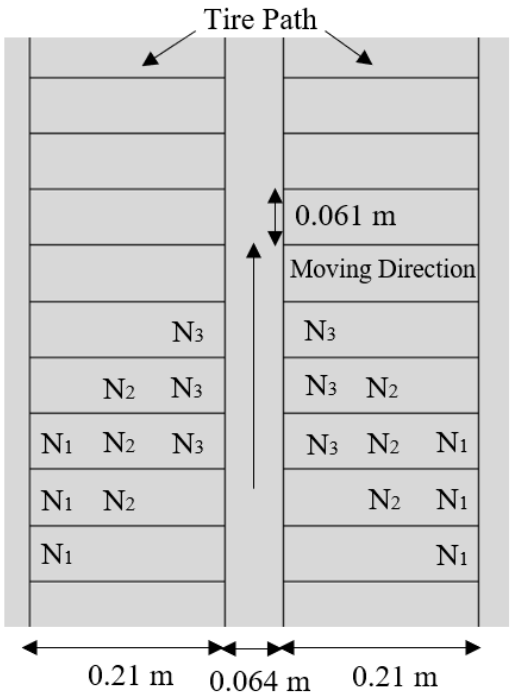


**(b) Magnified Tire Paths**

**Figure 2.1 The 3D Pavement FE Model**

**Table 2.1 Model Parameters of the 3D FE Pavement Model**

| Layer | Model Parameters | | | |
|---|---|---|---|---|
| Surface | Thickness, m | 0.10 | Density, kg/m3 | 2400 |
| | Poisson's Ratio | 0.35 | Damping Coefficient | 0.05 |
| | $E_i$, MPa | | $\tau_i$, s | |
| | $E_\infty$ | 41.71 | $\tau_1$ | 4.09E-06 |
| | $E_1$ | 6564.22 | $\tau_2$ | 2.56E-04 |
| | $E_2$ | 6582.36 | $\tau_3$ | 7.71E-03 |
| | $E_3$ | 3200.51 | $\tau_4$ | 2.10E-01 |
| | $E_4$ | 1341.86 | $\tau_5$ | 3.88E+00 |
| | $E_5$ | 299.20 | $\tau_6$ | 6.53E+01 |
| | $E_6$ | 103.36 | | |
| Base | Thickness, m | 0.15 | Density, kg/m3 | 1800 |
| | Poisson's Ratio | 0.35 | Damping Coefficient | 0.05 |
| | Elastic Modulus, MPa | 250 | | |
| Subgrade | Thickness, m | 1.78 | Density, kg/m3 | 1600 |
| | Poisson's Ratio | 0.4 | Damping Coefficient | 0.05 |
| | Elastic Modulus, MPa | 100 | | |

As shown in Figure 2.1(a), two tire paths in the horizontal direction are created for contact stresses between the pavement surface and two tires. The width of each path is 0.213 m (8.4 in), which equals the width of the contact area between the pavement surface and each tire. The length of each contact area 0.183 m (7.2 in) is divided into three equal parts in the direction of the vehicle movement. The vehicle movement is simulated as the contact stress moves one part forward at each analysis step. The duration of one analysis step is therefore calculated by dividing the length (0.061 m) of each part by the vehicle's moving speed. Figure 2.1(b) shows the contact areas at three successive analysis steps, where the contact stress acts from $N_1$ to $N_3$. For simplicity,

the contact stress between the tire and the pavement surface is assumed to be a 0.7-MPa (100-psi) constant pressure distributed uniformly on the contact area. The simulation method of the vehicle movement and parameters of the structural geometry, material properties and tire configuration are applied in previous a research on pavements under moving loads (Herr et al., 1995).

### 2.3 A 2D Axisymmetric Pavement FE Model under Stationary Dynamic Loads

To simulate the same pavement, parameters such as the layer depth and material properties of the 2D axisymmetric pavement model shown in Figure 2.3(a) are identical to those in the 3D pavement model in Section 2.2. Stationary dynamic loads applied in the 2D axisymmetric model follow the standard FWD test. A circular area with a 0.15-m (6-in) radius is created as in Figure 2.2(b) to represent the loading area in the standard FWD test. The time history of the dynamic load also follows the standard FWD test, of which the shape is semi-sinusoidal with the load magnitude F and duration T as in Figure 2.2(c). Since the loading area is known and fixed, the load can also be represented by the pressure magnitude P and the cycle T as in the following text. In order to eliminate boundary effects and achieve a balance between the accuracy and computational time, the radius of the model is determined by a simple sensitivity analysis. The load with the load magnitude 40 kN and duration 0.03 s is applied in models with increasing model radii. The maximum deflections at the loading center are compared. As the radius increases from 2.54 m (100 in) to 7.62 m (300 in), the relative error of the maximum deflection decreases from 2.72% to 0.17%., which indicates a

convergence. Therefore, the 7.62 m is selected as the model radius for all 2D axisymmetric models in this section.

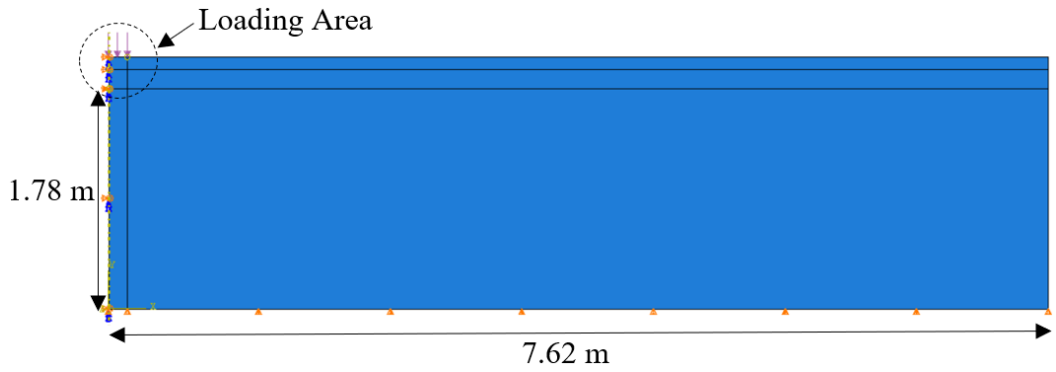


**(a) Cross Section of the 2D Axisymmetric Pavement Model**

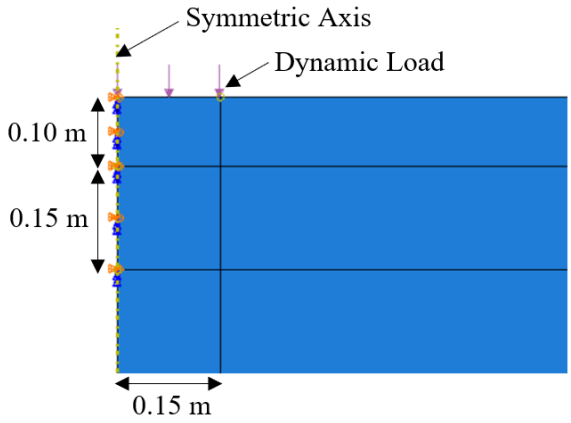


**(b) Magnified Loading Area**

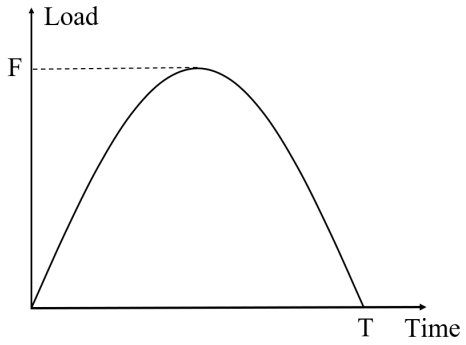


**(c) Applied Dynamic Load**

**Figure 2.2 The 2D Axisymmetric FE Pavement Model**

In this section, different load types are applied in different FE model types. Therefore, selected pavement response as indicator for the equivalency should be available in both model types. Moreover, selected pavement response should be representative and sensitive to parameters of both load types such as the load magnitude, the frequency of stationary dynamic loads and the speed of moving loads, etc.

Based on the measured responses from field tests and previous researches on the load equivalency, the magnitude and the duration of the deflection history are selected for the load equivalency. In 3D FE models, the deflection history of the pavement center as the moving load passes by can be obtained. Figure 2.3(a) shows an example that the deflection at the pavement center initiates and increases as the load approaches and vanishes as the load leaves. To isolate effects of the moving load on the deflection, the deflection history is processed by extracting and rescaling the deflected part. In 2D axisymmetric FE models, the deflection history of the load center under the stationary dynamic load has a similar shape which is shown in Figure 2.3(b). The deflection histories obtained from 3D and 2D axisymmetric models are comparable since they represent the same response of a specified location on the pavement surface to a traffic-like load. The difference is that effects of the moving load vary with the relative distance between the load and the specified location. While in the stationary dynamic load, such variation reflects on the load (pressure) changing with time.

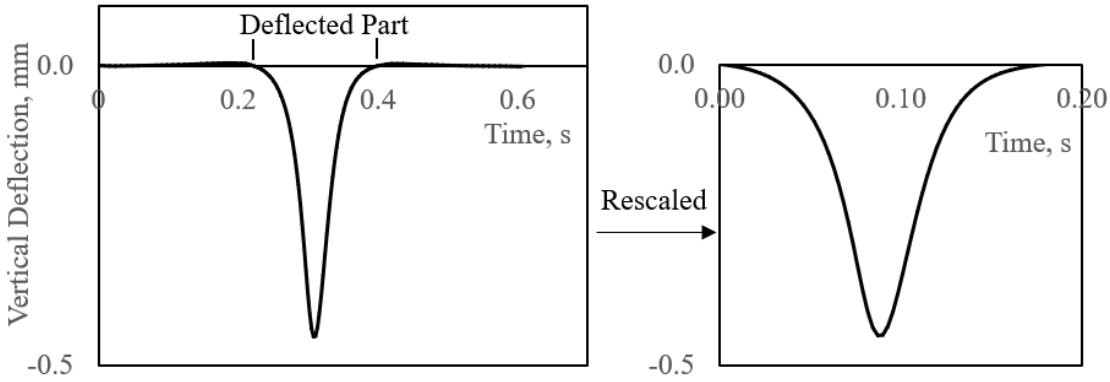


**(a) Complete Deflection History and Rescaled Deflected Part at the Pavement Center under the Moving Vehicular Load**

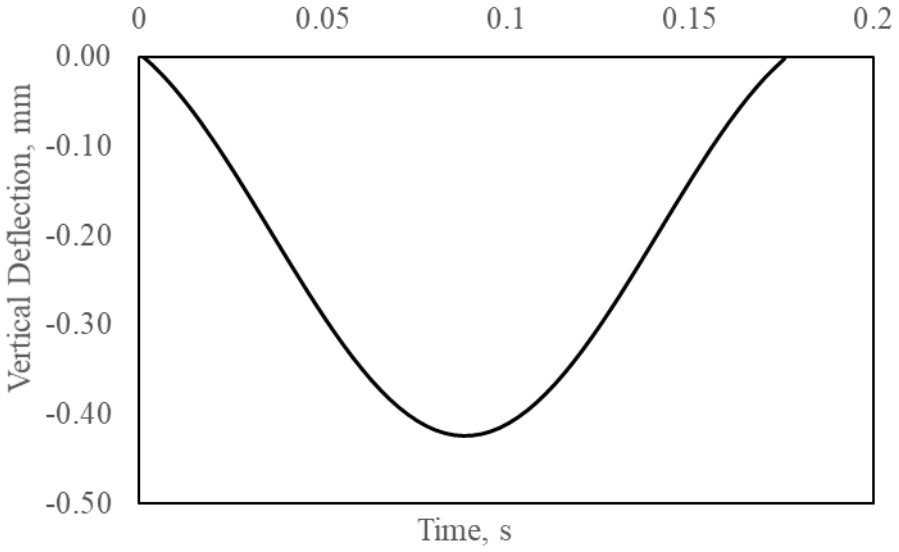


**(b) Complete Deflection History at the Load Center under the Stationary Dynamic Load**

**Figure 2.3 Pavement Responses from 3D and 2D Axisymmetric Models**

## 2.4 FE Model Updating

The FE model updating is a process widely used in the construction, maintenance and health monitoring of infrastructures, of which real-time conditions are required

(Friswell and Mottershead, 2013). The initial FE model is usually built based on design parameters of the structure. As the structure deteriorates, changes in its properties result in changes in its behaviors, which widens differences between structural responses measured in field tests and predicted by the initial FE model. By adjusting FE model parameters to match predicted responses with ones measured in field tests, deterioration locations and conditions of the structure can be determined from the comparison between the initial and adjusted FE model parameters (Qin et al., 2018b).

In this section, FE model updating is used to determine the equivalent stationary dynamic load for a certain moving load by treating responses of the 3D FE model as "field measurements". Since the equivalent dynamic load should cause similar responses in the 2D axisymmetric model as the moving load does in the 3D model, parameters of the equivalent dynamic load can be calibrated by matching responses of two FE models. The FE model updating process is described as follows and illustrated in Figure 2.4.

Step 1: build a 3D FE pavement model under the moving vehicular load at a specified speed $v$. Obtain the magnitude $d_0$ and duration (which is represented by the time to reach the deflection magnitude, $t_0$) of the revised deflection history at the pavement center as in Figure 2.3;

Step 2: build a 2D axisymmetric FE pavement model under the stationary dynamic load with the pressure magnitude $P_i$ and cycle $T_i$. Obtain the magnitude $d_i$ and duration (which is also represented by the time to reach the deflection magnitude, $t_i$) of the deflection history at the load center;

Step 3: compare responses $d$ and $t$ from 3D and 2D axisymmetric FE models using the objective function $f$ as Equation 2.2;

Step 4: check the stop criterion. If the criterion is satisfied, record $P_i$ and $T_i$ as the magnitude and cycle of the equivalent dynamic load for the moving load at the speed $v$. If not, use the AI algorithm described in following text to determine $P_i$ and $T_i$ for the next round of Step 2 – Step 4.

$$f(P_i, T_i) = \sqrt{(d_i - d_0)^2 + (t_i - t_0)^2} \tag{2.2}$$

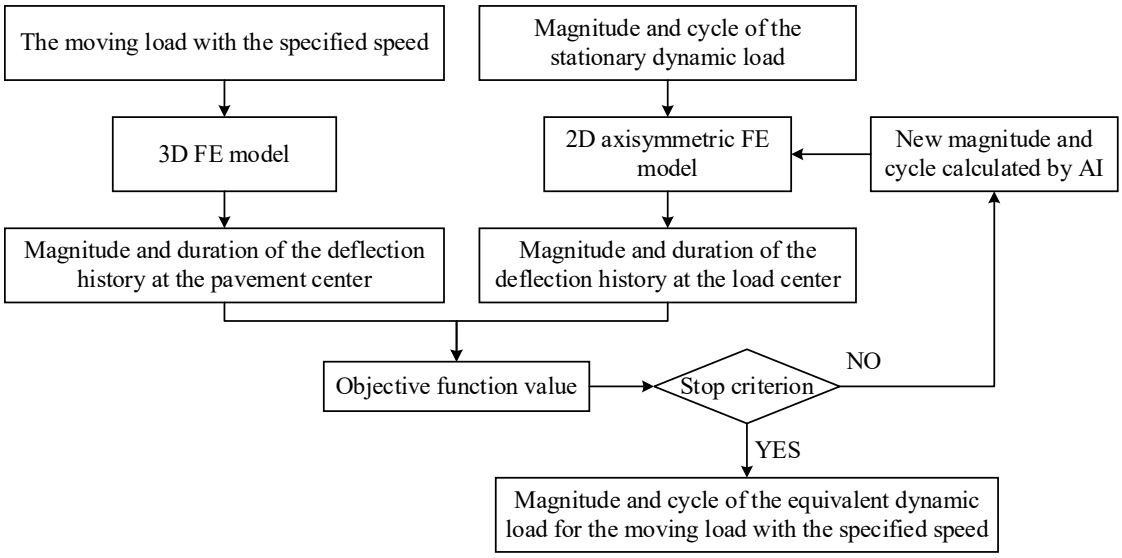


**Figure 2.4 Flow Chart of the FE Model Updating**

By adopting the FE model updating, the original problem in this study has been turned into the optimization of the objective function $f$. Therefore, AI algorithms are implemented into the process for an intelligent and efficient search for the optimal solution of the optimization problem.

## 2.5 Four AI Algorithms

### *2.5.1 Particle Swarm Optimization*

The particle swarm optimization (PSO) is one of the evolutionary algorithms (Qin et al., 2018b). It was developed in 1995 and used to improve the solution of an optimization problem iteratively by simulating the social behaviors of the swarm such as fishes, bees and birds (Eberhart and Kennedy, 1995). The behaviors of an individual in the swarm rely on both the individual and group knowledge. Similarly, in the PSO, the movement of each particle in the solution space is determined by the fitness of all particles according to the objective function (Shabbir and Omenzetter, 2015).

As illustrated in Figure 2.5, in the k-th iteration, the i-th particle holds a position $\mathbf{x}_i^k$ in a two-dimensional solution space, which represents the pressure magnitude and cycle of the dynamic load in this problem. Meanwhile, the best position of the i-th particle in the past k iterations $\mathbf{p}_i^k$ and the best position of all particles in the past k iterations $\mathbf{g}_i^k$ are determined according to the objective function. The position of the i-th particle in the (k+1)-th iteration $\mathbf{x}_i^{k+1}$ is determined by $\mathbf{p}_i^k$, $\mathbf{g}_i^k$, and its initial velocity vector $\mathbf{v}_i^k$ using Equation 2.3,

$$\mathbf{x}_i^{k+1} = \mathbf{x}_i^k + \mathbf{v}_i^{k+1} \tag{2.3}$$

in which,

$$\mathbf{v}_i^{k+1} = w\mathbf{v}_i^k + c_1 r_{1,i}^k(\mathbf{p}_i^k - \mathbf{x}_i^k) + c_2 r_{2,i}^k(\mathbf{g}_i^k - \mathbf{x}_i^k) \tag{2.4}$$

where $w$ is the inertial weight; $c_1$, $c_2$ are the cognition and social coefficients, respectively; and $r_1$, $r_2$ are the random numbers.

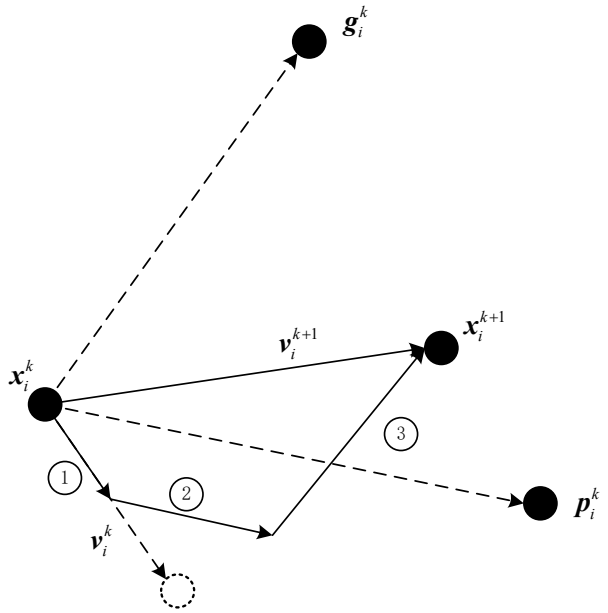


**Figure 2.5 Determination of the Particle Location in PSO**

The PSO takes advantages of search abilities of all particles that are spread out in the solution space, which improves the search efficiency for the global optimum solution and reduces the possibility to be stuck in a local minimum of the objective function. Moreover, its simple expression, eases of implementation and adjustment result in extensive use of the PSO in different areas of civil engineering (Lu et al., 2012; Gandomi et al., 2013).

### *2.5.2 Quantum-Behaved Particle Swarm Optimization*

To further address the issue that the global optimum solution of the problem may not be found by PSO (Bergh, 2001), the quantum-behaved particle swarm optimization (QPSO) was developed by determining the position of each particle in the solution space from a probability density function (Sun et al., 2004a).

The particle's position expressed as Equation 2.5 was developed from the Monte Carlo method, which solves problems by stochastic simulation (Sun et al., 2004b). As an improved algorithm for the PSO, the QPSO has fewer parameters to adjust since it replaces the velocity vector $\mathbf{v}$. And it is proven to have higher efficiency to find the global optimum solution in some complicated optimization problems (Sun et al., 2004a; Sun et al., 2004b; Yang et al., 2015). In this section, the QPSO was also applied as a comparison with the original PSO method.

$$\mathbf{x}_i^{k+1} = \begin{cases} \mathbf{P}_i^k + \alpha \left| \mathbf{x}_i^k - \mathbf{m}_i^k \right| \ln(1/u_i^k), & v_i^k \geq 0.5 \\ \mathbf{P}_i^k - \alpha \left| \mathbf{x}_i^k - \mathbf{m}_i^k \right| \ln(1/u_i^k), & v_i^k < 0.5 \end{cases} \tag{2.5}$$

in which,

$$\mathbf{m}_i^k = \frac{1}{N} \sum_{i=1}^{N} \mathbf{p}_i^k \tag{2.6}$$

$$\mathbf{P}_i^k = \varphi_i^k \mathbf{p}_i^k + (1 - \varphi_i^k) \mathbf{g}_i^k \tag{2.7}$$

$$\varphi_i^k = \frac{c_1 r_{1,i}^k}{c_1 r_{1,i}^k + c_2 r_{2,i}^k} \tag{2.8}$$

where $\alpha$ is the contraction-expansion coefficient; and $u$, $v$ are random numbers.

### *2.5.3 Genetic Algorithm*

The genetic algorithm is another branch of evolutionary algorithms which was inspired by the theory of evolution (Holland, 1992). Each potential solution is represented as a chromosome. The solution is iteratively updated by generations of genetic operations such as the mutation, crossover, inversion and selection (Serrano et al., 2018). Figure 2.6 illustrates procedures of the GA in this study. First, the initial

population of chromosomes is created. Considering the pressure magnitude $P$ and cycle $T$ of the dynamic load are floats with different orders of magnitude, the value-encoding method is used, which means two genes contained in each chromosome are values of the magnitude $P$ and cycle $T$. Then, the fitness of each chromosome is calculated according to the objective function, which is used to determine the probability of the chromosome to reproduce the next generation. As the "parents" are selected, the "children" are then created by genetic operations illustrated in Figure 2.7.

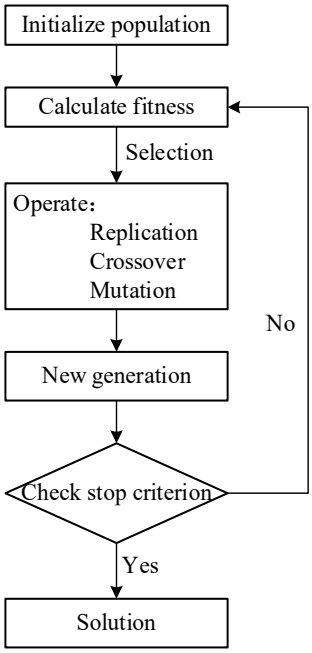


**Figure 2.6 Procedures of the GA Algorithm**

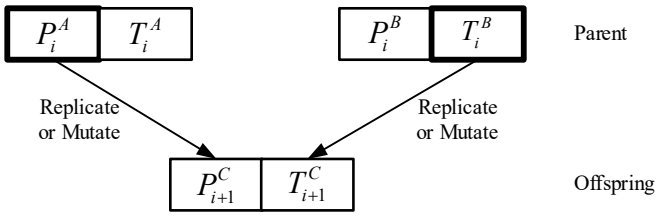


**Figure 2.7 Reproduction of the Chromosome**

Whether genes of the offspring are replicated or mutated from their parents is determined by a random process. The replicated gene contains the same information as its parent as Equation 2.9. While in the mutation function expressed as Equation 2.10, the value change in the offspring gene is determined by a random process and the current iteration number. Such non-uniform mutation operator is usually applied in the GA with float genes. It indicates the probability of the mutation decreases with the increasing evolution degree of the gene.

$$P_{i+1}^{C} = P_{i}^{A} \tag{2.9}$$

$$P_{i+1}^{C} = \begin{cases} P_{i}^{A}\left[1 + r_{1,i}\left(1 - \dfrac{i}{N}\right)^{2}\right], & r_{2,i} \le 0.5 \\ P_{i}^{A}\left[1 - r_{1,i}\left(1 - \dfrac{i}{N}\right)^{2}\right], & r_{2,i} > 0.5 \end{cases} \tag{2.10}$$

where $N$ is the total number of iterations; and $r_1$, $r_2$ are random numbers.

Similar with the PSO, the GA has advantages of the neat concept and easy implementation. The chromosome population contain and update solutions from the whole solution space, which contributes to obtaining the global optimum of the problem. So far, the GA has had many successful applications in civil engineering such as the structural optimization design and damage detection (Hao and Xia, 2002).

### *2.5.4 Steady-State GA for MGA*

As described above, genetic operations are conducted on the entire population at each iteration in the GA, which requires tremendous computational time. To improve the search efficiency and find all possible solutions for complex optimization problems, a

new method coupling the steady-state genetic algorithm (SSGA) and the technique of modeling to generate alternatives (MGA) was proposed and applied in civil engineering problems (Caicedo and Yun, 2011).

The SSGA was first proposed to fasten the convergence of traditional GA by operating genetic processes on a portion of the population (Syswerda, 1991). The generated offspring replace parents with lower fitness to form a new population. The MGA technique was developed for the complex and incompletely defined problems (Brill et al., 1990). Unlike mathematical problems, solutions with poorer performance in terms of the objective function value may provide better descriptions of engineering properties (Caicedo and Yun, 2011). These alternatives are maximally different with each other in the solution space and require evaluations based on the engineering judgement. The MGA gains a wide application in design and management problems (Baugh et al., 1997; Loughlin et al., 2001). The SSGA-MGA method is applied as a comparison with traditional GA.

The core idea of the SSGA-MGA is the group separation for reproduction. The first group is the MGA group, in which chromosomes should satisfy two criteria. Equation 2.11 and Equation 2.12 express the distance criterion and the fitness criterion respectively, which require chromosomes in the MGA group to locate differently in the solution space and to have desirable fitness. As shown in Figure 2.8(a), the first MGA chromosome $(P_1, T_1)$ is determined for its highest fitness among all chromosomes in the current iteration. Following that, each newly-determined MGA chromosome should check its relative fitness with $(P_1, T_1)$ and its relative distance with all previously-

determined MGA chromosomes. The second group is the pair group. As the name implies, each chromosome in the pair group is determined by the corresponding one in the MGA group. As illustrated in Figure 2.8(b), the pair chromosome is the one with the highest fitness within the range determined by Equation 2.13. The offspring are then produced by chromosomes in the MGA group with their pairs.

$$\cos(\theta_{k+1,i}) \le \alpha,\ i = 1,2,...,k \tag{2.11}$$

where $\theta_{k+1,i}$ is the angle between the (k+1)-th and the i-th MGA solutions; and $\alpha$ is the tolerance.

$$\left| \frac{f(P_1,T_1) - f(P_i,T_i)}{f(P_1,T_1)} \right| \le \beta,\ i = 2,...,k+1 \tag{2.12}$$

where $f(P_i,T_i)$ is the objective function value of the i-th MGA solution; and $\beta$ is the tolerance.

$$\cos(\alpha_i) \ge \alpha,\ i = 1,2,...,k+1 \tag{2.13}$$

where $\alpha_i$ = the angle between the i-th MGA solution and its pair; and $\alpha$ is the tolerance.

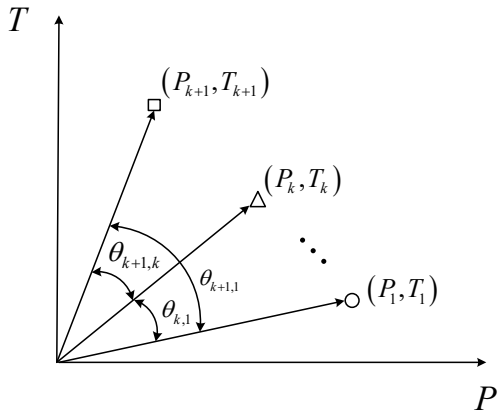


**(a) The MGA Group**

**Figure 2.8 The Group Selection in the SSGA-MGA Algorithm**

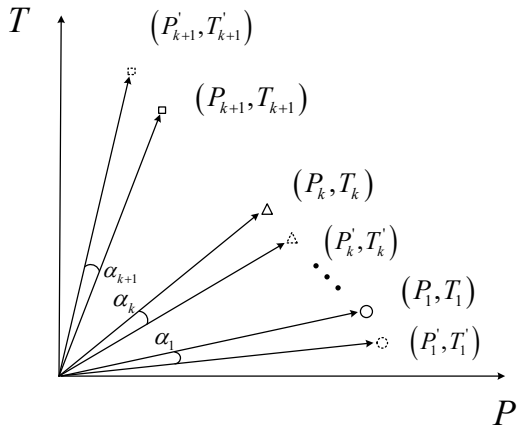


**(b) The MGA Group and Its Pair Group**

**Figure 2.8 Continued**

### *2.5.5 Comparison of Four AI Algorithms*

In order to compare four AI algorithms described above, they are applied in the FE model updating to find the pressure magnitude $P$ and cycle $T$ of the equivalent dynamic load for the moving load at the speed 80.5 km/h (50 mph). The performance of these AI algorithms is compared in terms of the accuracy and convergence rate. The value of the objective function at each iteration is calculated and recorded until the stop criterion in Figure 2.4 is satisfied, which requires the total iteration number to reach 40.

Figure 2.9 shows convergence patterns of four applied AI algorithms. It can be seen that the PSO, the QPSO and the GA finally reach similar degrees of optimization. The QPSO cannot obtain as desirable results as the PSO after 40 iterations. Similar results were obtained in a previous research (Omkar et al., 2009), which found the convergence pattern of the QPSO had a long plateau and the QPSO reached a similar degree of optimization as the PSO after additional hundreds of iterations. From the

figure, it also can be seen that two improved algorithms the QPSO and the SSGA-MGA fasten the convergence rate at the initial stage compared with the PSO and the GA.

Despite with the worst initial guess, the SSGA-MGA first reaches a desirable degree of optimization. However, it automatically stops after 24 iterations due to a defect in the algorithm. The population size in the SSGA-MGA has to be set by users according to the complexity of the problem and better helps to achieve a balance in the tradeoff between the computational time and accuracy. As described above, each chromosome in the pair group is selected for its highest fitness among chromosomes near the MGA chromosome. One special case is ignored that no single satisfied pair chromosome can be found in the current iteration. Whether the algorithm stops or not depends on the user setting instead of the solution accuracy, which should be addressed in the future. Overall, considering the stability and accuracy, the PSO is selected to deal with the rest cases in this study.

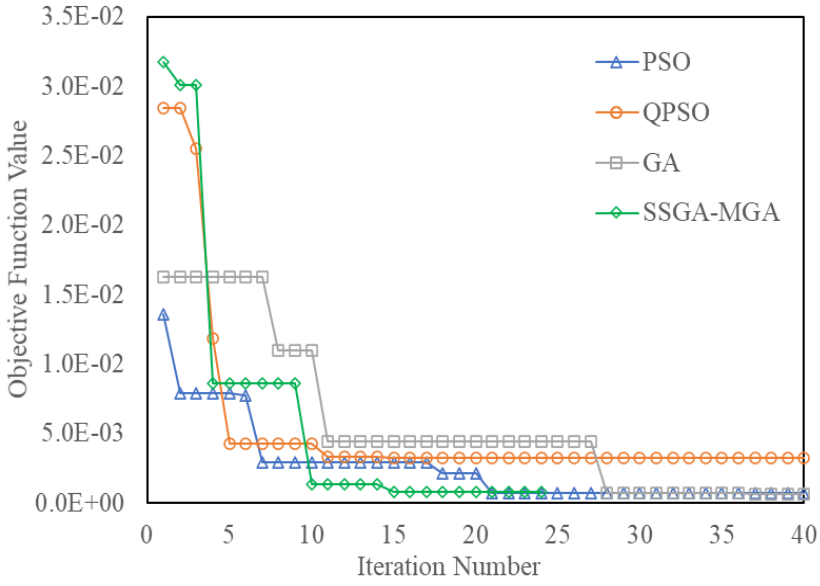


**Figure 2.9 Comparison of the Applied AI Algorithms**

## 2.6 Validations and Applications of the Equivalent Relationship

### *2.6.1 Validations of the Equivalent Relationship*

As a key characteristic of the moving load, the moving speed affects flexible pavement responses, of which the shape and magnitude of the deflection basin are changed under different speeds of loads. Obtained equivalent stationary dynamic loads for moving loads at different speeds are presented in Table 2.2, which can represent a typical dual-tire load moving at normal speeds. It can be seen that with the increase of the speed, the magnitude of the equivalent load remains at the same level while the cycle decreases significantly. Compared with the standard FWD load with the load cycle 0.03 s, magnitudes of equivalent dynamic loads in Table 2.2 are smaller and cycles are excessively larger, which shows the standard FWD load cannot represent traffic loads moving at highway speeds in terms of the magnitude and duration of the deflection history.

To validate obtained equivalent dynamic loads, pavement responses from 3D FE models with moving loads and 2D axisymmetric models with equivalent dynamic loads are directly compared and results are presented in Table 2.3. The relative errors in Table 2.3 show the accuracy of the relationship in Table 2.2 and the PSO algorithm.

**Table 2.2 Equivalent Dynamic Loads for Moving Loads at Different Speeds**

| Speed of the Moving Load, km/h (mph) | Equivalent Dynamic Load | |
|---|---|---|
| | Pressure Magnitude P, MPa | Load Cycle T, s |
| 40.23 (25) | 0.489 | 0.318 |
| 56.33 (35) | 0.485 | 0.223 |
| 80.47 (50) | 0.478 | 0.149 |

**Table 2.2 Continued.**

| Speed of the Moving Load, km/h (mph) | Equivalent Dynamic Load | |
|---|---|---|
| | Pressure Magnitude P, MPa | Load Cycle T, s |
| 112.65 (70) | 0.473 | 0.104 |
| 160.93 (100) | 0.471 | 0.062 |

**Table 2.3 Validations of Equivalent Dynamic Loads in Table 2.2**

| Speed of the Moving Load, km/h (mph) | Maximum Deflection, mm | | | Time to Reach the Maximum Deflection, s | | |
|---|---|---|---|---|---|---|
| | 3D FE Model | 2D Axisymmetric Model | Relative Error, % | 3D FE Model | 2D Axisymmetric Model | Relative Error, % |
| 40.23 (25) | 0.4905 | 0.4911 | 0.1248 | 0.1790 | 0.1778 | -0.7100 |
| 56.33 (35) | 0.4734 | 0.4727 | -0.1480 | 0.1265 | 0.1273 | 0.6629 |
| 80.47 (50) | 0.4515 | 0.4486 | -0.6419 | 0.0889 | 0.0874 | -1.6600 |
| 112.65 (70) | 0.4269 | 0.4266 | -0.0795 | 0.0637 | 0.0629 | -1.3779 |
| 160.93 (100) | 0.3960 | 0.3957 | -0.0910 | 0.0404 | 0.0400 | -0.9478 |

Similar with the moving speed, the magnitude of the moving load also affects flexible pavement responses. Moving loads of five different magnitudes moving at a common speed 80.47 km/h (50 mph) are applied in FE models. The magnitude and duration of the deflection are obtained and used to determine equivalent dynamic loads.

Table 2.4 shows equivalent dynamic loads for moving loads of five different magnitudes. As the magnitude increases, the pressure magnitude of the equivalent dynamic load also increases while the load cycle of the equivalent dynamic load nearly stays. The accuracy of results in Table 2.4 is validated in Table 2.5, which compares pavement responses from different FE models.

**Table 2.4 Equivalent Dynamic Loads for Moving Loads of Different Magnitudes**

| Magnitude of the Moving Load, MPa (psi) | Equivalent Dynamic Load | |
|---|---|---|
| | Pressure Magnitude P, MPa | Load Cycle T, s |
| 0.3447 (50) | 0.239 | 0.147 |
| 0.5171 (75) | 0.359 | 0.147 |
| 0.6895 (100) | 0.478 | 0.148 |
| 0.8618 (125) | 0.598 | 0.147 |
| 1.0342 (150) | 0.717 | 0.149 |

**Table 2.5 Validations of Equivalent Dynamic Loads in Table 2.4**

| Magnitude of the Moving Load, MPa (psi) | Maximum Deflection, mm | | | Time to Reach the Maximum Deflection, s | | |
|---|---|---|---|---|---|---|
| | 3D FE Model | 2D Axisymmetric Model | Relative Error, % | 3D FE Model | 2D Axisymmetric Model | Relative Error, % |
| 0.3447 (50) | 0.2258 | 0.2241 | -0.7594 | 0.0877 | 0.0863 | -1.6500 |
| 0.5171 (75) | 0.3387 | 0.3361 | -0.7529 | 0.0877 | 0.0860 | -1.9200 |
| 0.6895 (100) | 0.4515 | 0.4486 | -0.6419 | 0.0889 | 0.0874 | -1.6600 |
| 0.8618 (125) | 0.5645 | 0.5593 | -0.9221 | 0.0877 | 0.0861 | -1.8393 |
| 1.0342 (150) | 0.6775 | 0.6706 | -1.0187 | 0.0878 | 0.0871 | -0.7826 |

The relationship between the moving load and the dynamic load is built in terms of the magnitude and moving speed. The relationship can be summarized that the cycle and magnitude of the equivalent dynamic load are mainly affected by the speed and magnitude of the moving load, respectively. The quantitative relations are illustrated in Figure 2.10(a) and Figure 2.10(b) based on results presented in Table 2.2 and Table 2.4.

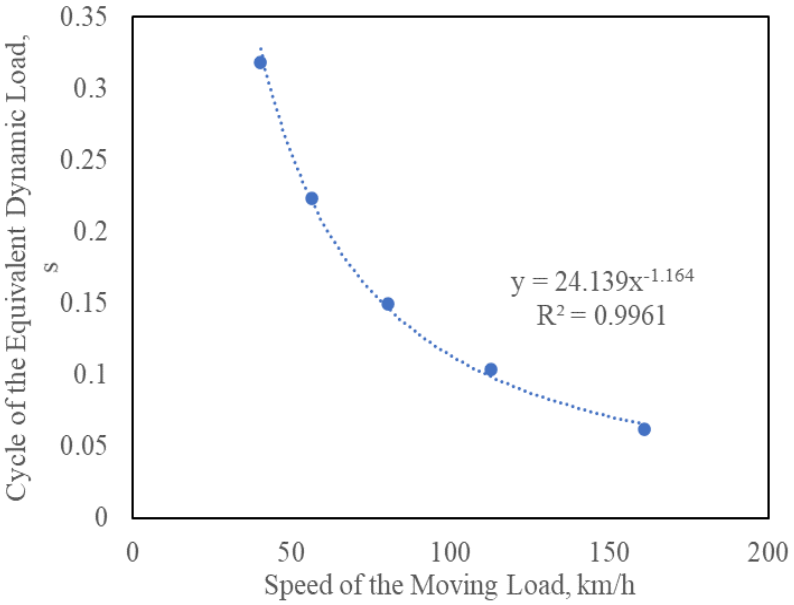


**(a) Relationship between the Speed of the Moving Load and the Cycle of the Dynamic Load**

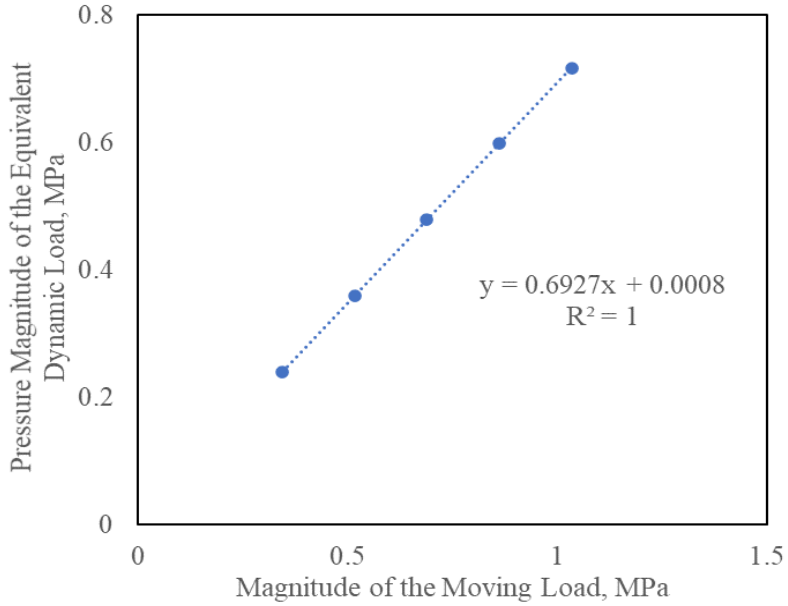


**(b) Relationship between Magnitudes of the Moving Load and the Dynamic Load**

**Figure 2.10 Relationship between the Moving Load and the Dynamic Load**

### *2.6.2 Applications of the Equivalent Relationship*

Next, obtained equivalent dynamic load for the moving load with the magnitude 0.6895 MPa (100 psi) and the speed 80.47 km/h (50 mph) is applied in various pavements of which the layer thickness or the layer material is different. Pavement responses from 3D FE models and 2D axisymmetric FE models are compared to check if this relationship is applicable in different pavements.

First, material properties of supporting layers and structural parameters of the pavement are adjusted. Table 2.6 describes 8 cases in which the modulus of the base and subgrade and the thickness of all three layers are adjusted. The comparisons of pavement responses are presented in Table 2.6 and Figure 2.11. All relative errors of the time to reach the maximum deflection are less than 3% and maximum deflections in all adjusted cases are near the equality line. Basically, it can be concluded that this relationship is independent of the thickness of all layers and the stiffness of supporting layers.

**Table 2.6 Applications of the Relationship in Pavements with Different Structural and Supporting Layer Material Properties**

| Case | Time to Reach the Maximum Deflection, s | | | Case Description |
|---|---|---|---|---|
| | 3D FE Model | 2D Axisymmetric Model | Relative Error, % | |
| Softer Base | 0.0872 | 0.0886 | 1.6319 | Reduce Base Modulus by 100 MPa |
| Stiffer Base | 0.0877 | 0.0869 | -0.9150 | Increase Base Modulus by 100 MPa |
| Softer Subgrade | 0.0881 | 0.0874 | -0.8519 | Reduce Subgrade Modulus by 20 MPa |
| Stiffer Subgrade | 0.0871 | 0.0880 | 1.0532 | Increase Subgrade Modulus by 100 MPa |

**Table 2.6 Continued**

| Case | Time to Reach the Maximum Deflection, s | | | Case Description |
|---|---|---|---|---|
| | 3D FE Model | 2D Axisymmetric Model | Relative Error, % | |
| Thinner Base | 0.0858 | 0.0879 | 2.4615 | Reduce Base Thickness by 50.8 mm (2 in) |
| Thicker Base | 0.0898 | 0.0873 | -2.7145 | Increase Base Thickness by 50.8 mm (2 in) |
| Thinner Surface | 0.0859 | 0.0841 | -2.0561 | Reduce Surface Thickness by 50.8 mm (2 in) |
| Thicker Surface | 0.0913 | 0.0900 | -1.5194 | Increase Surface Thickness by 50.8 mm (2 in) |

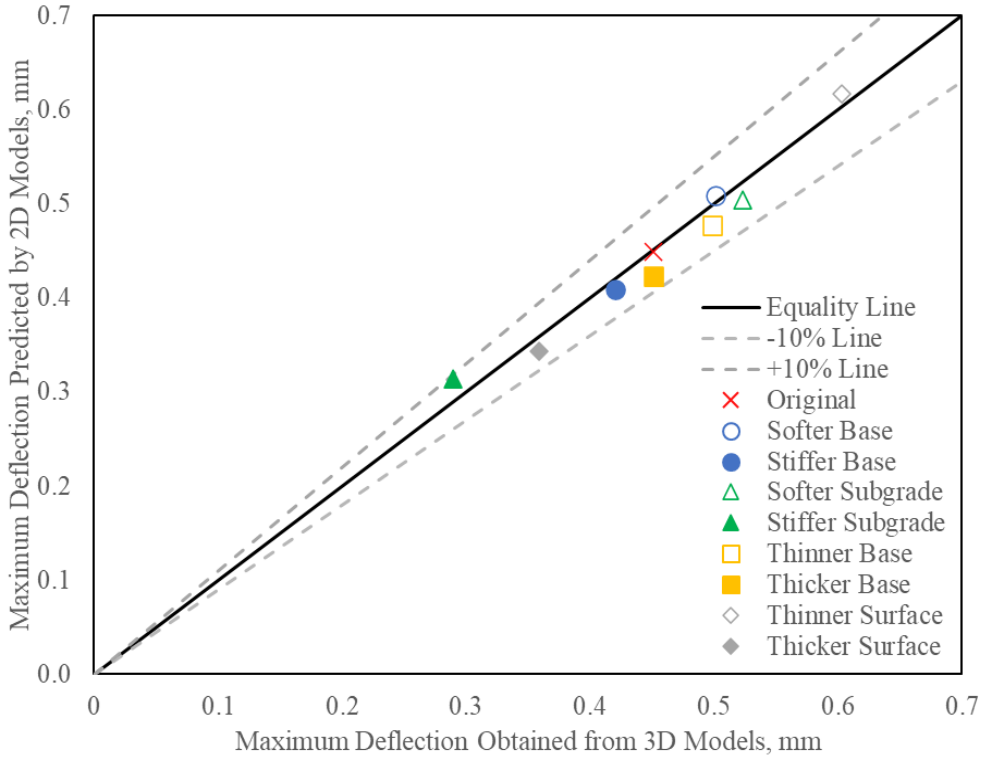


**Figure 2.11 Applications of the Relationship in Pavements with Different Structural and Supporting Layer Material Properties**

The aim of this conclusion is to simplify the future FE model updating for the load equivalency, in which any typical value within the normal range can be selected as the modulus of supporting layers without affecting the obtained equivalent dynamic load. Additionally, the obtained equivalent dynamic load can be directly used in 2D axisymmetric FE models implemented with complicated base/subgrade models (Gu et al., 2016; Zhang et al., 2018) for the model calibration. It will save considerable computational time compared with 3D FE models implemented with similar user-defined materials.

Different from supporting layers, stiffness of the surface layer is sensitive to the frequency/speed of the applied load (Al-Qadi et al., 2008; Ulloa et al., 2013), which affects the magnitude of the vertical deflection. Similarly, the phase angle of the surface layer is sensitive to the frequency/speed of the applied load as well, which affects the lag time between magnitudes of the load and responses (Reese, 1997). It seems that two inputs of the objective function are impacted by the surface layer. Therefore, it is well worth a study whether the obtained relationship can be applicable in pavements with different surface layer materials.

Zhang et al. (2016) conducted dynamic modulus tests on asphalt mixtures and obtained their Prony series parameters. The asphalt mixtures contained the same kind of asphalt binder but were with different aging periods and air void contents. Accordingly, their behaviors under dynamic/moving loads are supposed to be different. Table 2.7 presents 6 asphalt mixtures of 3 aging periods and 2 air void contents. These materials are simulated in 3D and 2D axisymmetric FE models and their pavement responses are

compared. The relative errors of the time to reach the maximum deflection in Table 2.7 are at the same level as in Table 2.6. However, maximum deflections in Figure 2.12 from two FE models are not as close to the equality line as in Figure 2.11.

**Table 2.7 Validations of the Relationship in Pavements with Different Surface Material Properties**

| Case Number | Time to Reach the Maximum Deflection, s | | | Case Description |
|---|---|---|---|---|
| | 3D FE Model | 2D Axisymmetric Model | Relative Error, % | |
| 1 | 0.0910 | 0.0894 | -1.7969 | Aging Period: 0 Month; Air Void: 4% |
| 2 | 0.0902 | 0.0897 | -0.4932 | Aging Period: 0 Month; Air Void: 7% |
| 3 | 0.0911 | 0.0898 | -1.4654 | Aging Period: 3 Months; Air Void: 4% |
| 4 | 0.0899 | 0.0875 | -2.6477 | Aging Period: 6 Months; Air Void: 4% |
| 5 | 0.0896 | 0.0876 | -2.1799 | Aging Period: 3 Months; Air Void: 7% |
| 6 | 0.0895 | 0.0877 | -2.0379 | Aging Period: 6 Months; Air Void: 7% |

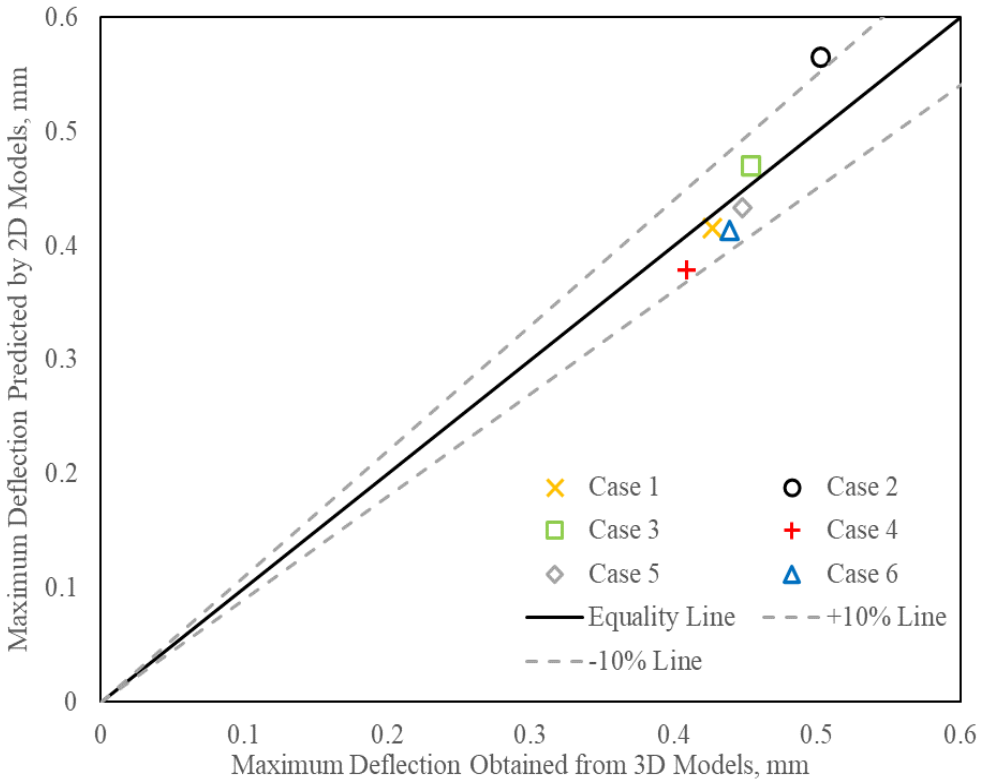


**Figure 2.12 Validation of the Relationship in Pavements with Different Surface Material Properties**

# 3. INVERSE ANALYSIS OF FATIGUE DAMAGE IN FLEXIBLE PAVEMENTS*

## 3.1 Introduction

The review of common NDT devices in previous sections reveals advantages of continuous deflection profiles and the importance of moving speeds in obtaining complete and accurate pavement responses. However, the operation of highway-speed NDT devices, like the TSD, is usually expensive and limited. To justify its use on pavement networks, it must provide comprehensive pavement network asset information which can be used to make cost-effective maintenance and rehabilitation decisions. This requires the ability to analyze the measured results objectively and, if possible, provide timely advanced warning of impending costly levels of future distress. This objective analysis can be achieved through the use of the numerical computations to simulate pavement responses in real conditions. The purpose of the numerical simulation is to provide a sound and consistent mechanics-based method of interpreting the results. The FE models have been widely used due to its low expenses, high efficiency and desirable matches with in-service pavements. Many techniques have been developed and incorporated in the FE codes and softwares for simulation of loading, geometry and material characterization (Howard and Warren, 2009). The simulated responses of pavements are then compared with field data from NDT devices or instrumented

*Reprinted with permission from "3D simulation of deflection basin of pavements under high-speed moving loads" by Deng Y. et al., 2019. *Construction and Building Materials*, Vol. 226, pp 868-878, Copyright 2019 Elsevier Ltd.

pavement sections to evaluate the accuracy of FE models. A few examples are reviewed herein.

Zaghloul and White (1993) built a three-dimensional (3D) elastic multilayer system in ABAQUS to simulate uncracked pavements under moving loads. The moving load was represented by a step function of which the duration was controlled by the moving speed. Numerical results were compared with discrete field measurements including horizontal strains and surface deflections. The numerical results showed good matches with the field data. Uddin et al. (1994) built a three-layer elastic system to simulate both uncracked and cracked pavements under static and dynamic loads. The moduli of the layers were obtained from the FWD backcalculation; the dynamic load of the FWD was simulated using a uniform pressure of which the magnitude varies with time.

Mulungye et al. (2005) built a 2D model in the software ANSYS using a viscoelastic surface layer to predict responses of flexible pavements under single and multiple axle loads. The moving loads were simulated as cyclic loads distributed uniformly on the pavement. A good agreement between predicted and measured strains at the bottom of the surface layer showed the applicability of FE models in flexible pavements. Li et al. (2017) applied an improved 2D axisymmetric model for flexible pavements with a stress-dependent supporting layer. Effects of viscoelasticity and nonlinearity of materials on pavement responses under dynamic FWD loads were discussed.

Based on the studies on tire-pavement contact stresses (De Beer et al., 2002; Al-Qadi and Wang, 2009), Al-Qadi et al. (2005) and Li et al. (2016) applied continuously moving loads distributed nonuniformly on flexible pavements in the FE models. Predicted responses of pavements such as tensile strains at the bottom of the surface and stresses in the base layer were compared with the measured data. Results showed the loading configuration had significant effects on pavement responses.

The studies described above highlight the development of FE models in terms of material properties and loading configurations of pavements. There are few studies that focus on generating continuous deflection profiles with highway speeds. Thus, it is the goal of this section to investigate characteristics of continuous deflection profiles of a pavement under high-speed moving loads. Furthermore, characteristics of continuous deflection profiles to different materials, structures and moving speeds are investigated. The 3D computational simulation is an effective technique for this purpose with the combination of different pavement types, conditions, and moving speeds. The technical background regarding viscoelastic pavement responses under a moving load is first introduced. Then the construction of a 3D pavement model with a moving load is presented. The simulation results for different pavement types, conditions, and moving speeds are subsequently presented and discussed. Furthermore, a case study is given to validate the simulated pavement deflections using measured continuous deflections by the RWD and the TSD in the field. Finally, similar analysis using equivalent stationary dynamic loads is presented, which aims for potential applications in NDT with stationary dynamic loads such as the FWD.

### 3.2 Characterization of Pavement Responses under Moving Loads

In order to obtain more representative continuous deflection profiles of a pavement under traffic loading, traffic loads and pavement responses need to be more accurately characterized. Two types of characteristics – the moving speed and dynamic properties of vehicles (period of vibration, etc.) are modeled as combinations of springs and dampers such as the quarter-car suspension model (Gillespie, 1992). In analytical and computational applications of layered pavement systems, traffic loads are usually simplified as haversine-shaped stationary dynamic loads (Huang, 2004). The impact of the traffic speed on flexible pavements was examined by adjusting the period of the haversine function (Hardy and Cebon, 1994). It was concluded that the structural inertial damping caused a lag distance between the maximum deflection and the traffic load. It also demonstrated that higher moving speeds decreased magnitudes of strains for all pavement layers while making the response peak lag further behind the load (Hardy and Cebon, 1994). The pavement responses are usually regarded as the response model to a dynamic load, which include both the stiffness and inertial damping of the structure. However, some existing pavement response models use an elastic modulus and ignore the effect of inertial damping of the structure (Lytton, 1989; Hardy and Cebon, 1994). Also, for flexible pavements the viscoelasticity of pavement materials is an important factor affecting the responses of the pavement. In a recent study (Khazanovich and Booshehrian, 2015), the inertia and viscoelastic properties of the surface and supporting layers were taken into consideration for some rigid and flexible pavements. The analytical model was evaluated using measured data from the FWD. The good match

showed both viscoelasticity and inertia of pavement materials had effects on responses of pavements to dynamic loads applied by the FWD.

Considering both the inertial damping of the structure and viscoelasticity of pavement materials, this section proposes a hypothesis for the pavement responses under high-speed moving loads: an asymmetric deflection basin with a steep leading edge and a shallow trailing edge as shown in Figure 3.1. There is a lag angle between the traffic load and the maximum deflection point in the basin. The location where the maximum deflection occurs falls behind the contact point of the tire and the pavement surface.

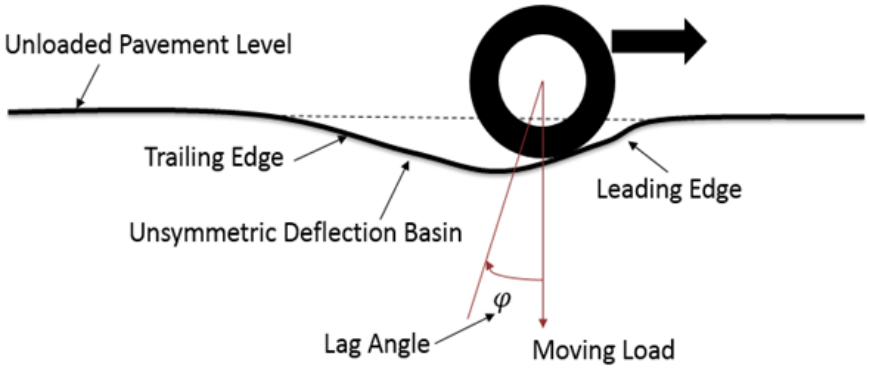


**Figure 3.1 Illustration of Deflection Basin of a Pavement under a High-speed Moving Load**

The phenomenon of the lag between the load and response is usually observed in the dynamic modulus test on viscoelastic materials, in which oscillatory loads are applied. The time lag between peaks of the stress and strain is used to obtain the phase angle and dynamic modulus which represent viscoelasticity of materials (Lakes, 2009). The phase angle between the stress and strain is similarly defined as Equation 3.1,

$$\delta = 2\pi\Delta t / T \tag{3.1}$$

where $\delta$ is the phase angle between the stress and strain of the material; $\Delta t$ is the time lag between peaks of the stress and strain within one cycle; and $T$ is the period of an oscillatory load. Similarly, the lag phase between the traffic load and maximum deflection is defined as Equation 3.2,

$$\varphi = 2\pi\Delta t' / T' \tag{3.2}$$

in which,

$$T' = L / v \tag{3.3}$$

where $\varphi$ is the lag angle between the traffic load and maximum deflection; $\Delta t'$ is the time lag between the center line of the traffic load and maximum deflection within one deflection basin; $T'$ is the period of a deflection basin; $L$ is the length of the deflection basin; and $v$ is the speed of the traffic load.

To simulate real conditions of a pavement, two 3D pavement structures are built in ABAQUS: (1) a 0.152 m (6-in) surface layer, a 0.304 m (12-in) base course, and a 1.778 m (70-in) subgrade; and (2) a 0.152 m (6-in) surface layer, a 0.152 m (6-in) treated base, a 0.152 m (6-in) unbound base, and a 1.778 m (70-in) subgrade. The adjacent layers are considered as fully bonded with each other. The former pavement structure is shown in Figure 3.2 as an example, in which Poisson's ratio and density of each layer are presented. The entire model is meshed using hexahedron elements, as shown in Figure 3.3. The mesh size in the vertical direction is based on the thickness of each layer. In the lateral and horizontal directions, finer meshing is applied in the two loading paths, representing loads applied by dual tires.

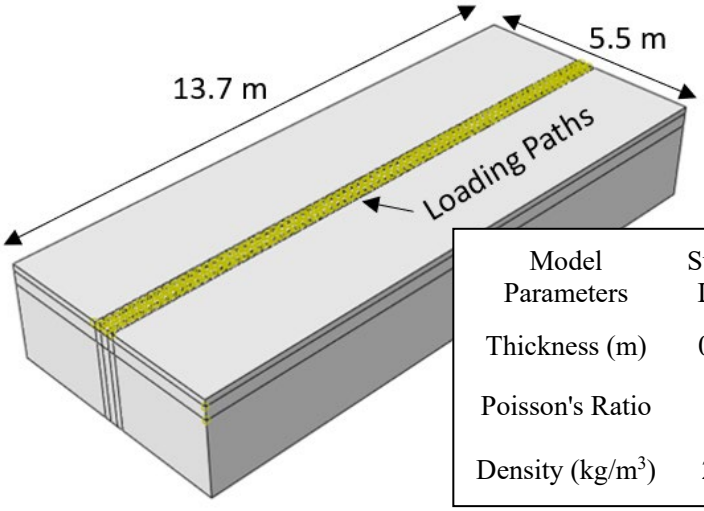


| Model Parameters | Surface Layer | Base Layer | Subgrade |
|---|---|---|---|
| Thickness (m) | 0.152 | 0.304 | 1.778 |
| Poisson's Ratio | 0.35 | 0.35 | 0.4 |
| Density (kg/m$^3$) | 2243 | 1922 | 1922 |

**Figure 3.2 3D Pavement Structure and Parameters Used in ABAQUS**

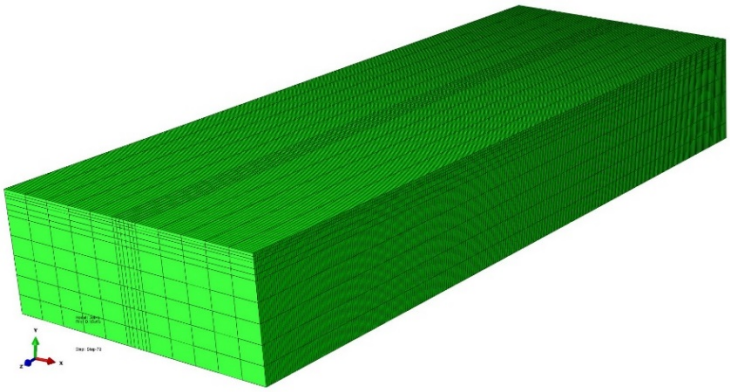

**(a) Entire Pavement Structure**

**Figure 3.3 The Meshed Models in ABAQUS**

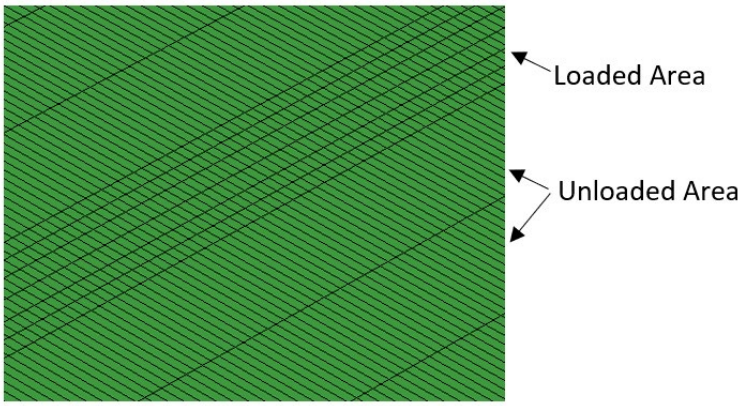


**(b) Pavement Surface**

**Figure 3.3 Continued**

Different from 3D FE models in Section 2 which applies moving loads with constant contact stresses, nonuniform contact stresses between tires and pavement surfaces are considered in this section. A 315/80R22.5 dual-tire vehicle is selected as a typical traffic loading (Ling et al., 2017c). The contact load is 40 kN and tire inflation pressure is 689.5 kPa. The tire-pavement interactions are represented based on a comprehensive study by De Beer et al. (2002), which characterized typical contact stress distributions based on the simultaneous measurements of moving tires and pavement interface contact stresses. When tires act on the surface of the pavement, the contact stress between each tire and the pavement surface is composed of stresses in vertical, longitudinal and transverse directions. The magnitude and distribution of the contact stress rely on the tire type, tire inflation pressure and constant load on the tire. Figure 3.4 shows the distributions of the contact stresses of the selected vehicle load in three directions on the pavement surface. The magnitudes of the vertical, longitudinal and

transverse stresses are 1350.7 kPa, 193.7 kPa and 247 kPa respectively. The values of vertical and longitudinal contact stresses change along the direction of tire length and keep constant in the direction of tire width, while the value of transverse contact stress changes along both directions.

Figure 3.5 shows two loading paths of 157.5-mm (6.2-in) in width and 190.5-mm (7.5-in) in length which are created symmetrically along the longitudinal direction with a 193.0-mm (7.6-in) space between wheel paths. The simulation of the movement is similar as Figure 2.1(b). In each step, the load moved forward one tire path.

Figure 3.6 shows nonuniform contact stresses in three directions built in ABAQUS. The load moves along the loading paths and passes through the entire pavement model in the way introduced in Section 2.2. The deflections of the entire model are collected when the load is at the center of the pavement model. The finer mesh along the loading path allows generating more data of the deflection basin for precise analysis.

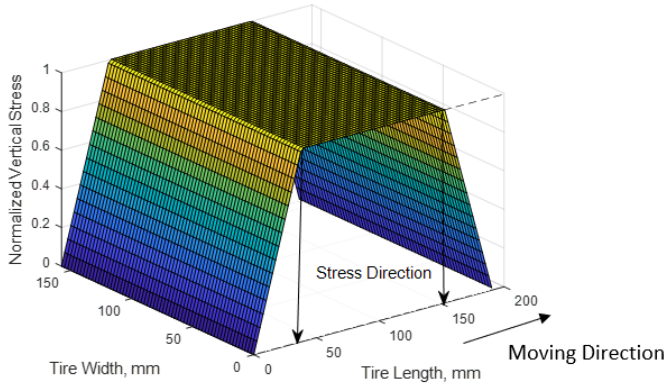


**(a) Vertical Contact Stress**

**Figure 3.4 The Contact Stress between a 315/80R22.5 Tire and the Pavement**

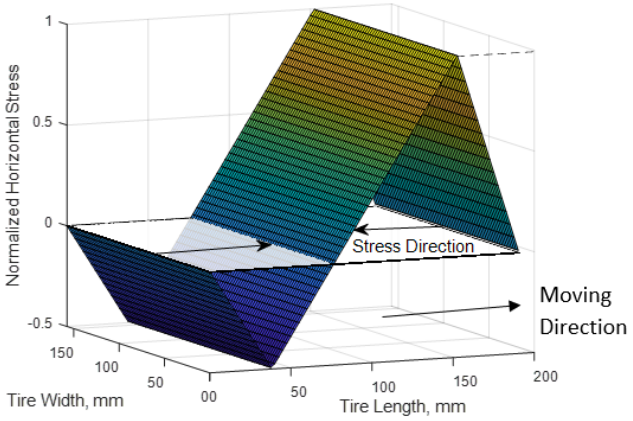


**(b) Longitudinal Contact Stress**

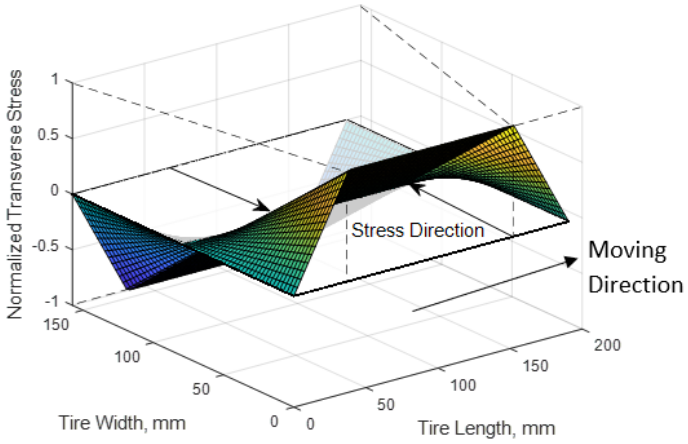


**(c) Transverse Contact Stress**

**Figure 3.4 Continued**

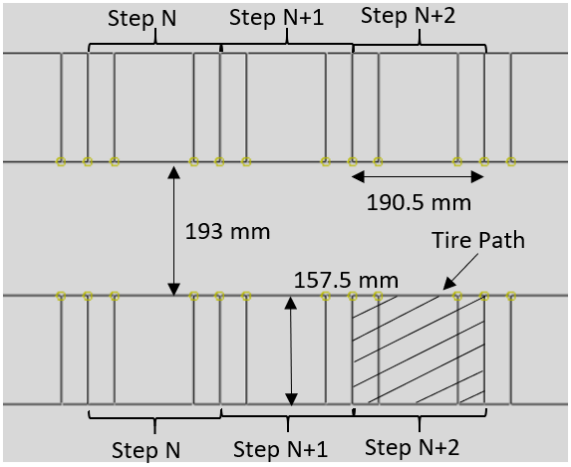


**Figure 3.5 Simulation of Moving Loads in FE Analysis**

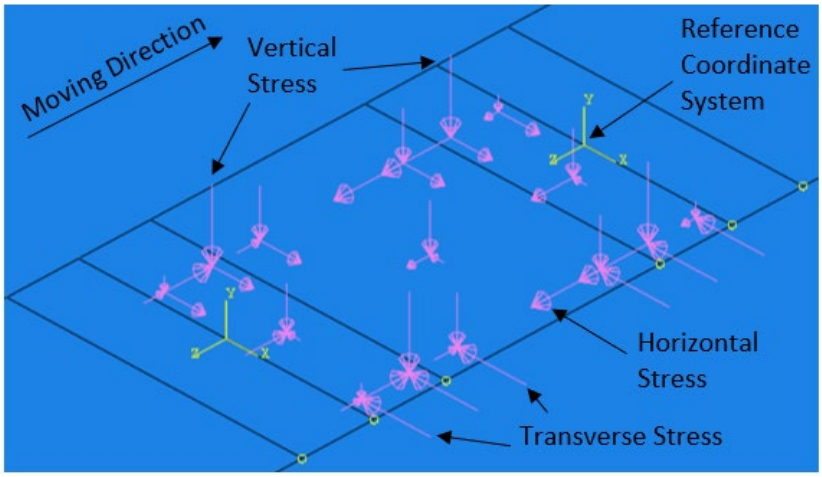


**Figure 3.6 The Contact Stress between Tires and the Pavement Surface in ABAQUS**

In this section, 3D FE simulations are performed for 5 different pavement types in the field of light or heavy duty: asphalt surface over unbound base course, asphalt surface over stabilized base, concrete surface unbound base, concrete surface over stabilized base, and asphalt surface over asphalt-treated base, as listed in Table 3.1. For

each pavement type, 4 different velocities of the moving load (24 km/h, 40 km/h, 64 km/h, and 80 km/h) are selected. The material properties of each pavement type are given in Table 3.2.

For the selected pavement types and materials, the asphalt mixtures in the surface layer are modeled as viscoelastic materials. In addition, as the asphalt treated base course gains more applications (Mohammad et al., 2013), the asphalt-treated base course is applied in this study and characterized as surface materials (Yoo and Al-Qadi, 2008; Gu et al., 2019). The concrete surface and aggregate materials in the base course and subgrade are considered as elastic materials. Since the shapes of deflection basins are affected by both viscoelasticity and inertial damping (Deng, 2017), a typical structural inertial damping factor 5% is selected for surface materials in both flexible and rigid pavements. For materials in the base course and subgrade which are usually in unsaturated conditions, it was found that the viscoelastic characteristics of soils measured in the laboratory experiment were more obvious as the moisture content increased (Kondner and Ho, 1965). As the water flows through the voids in the base and subgrade with the increase of load cycles, the viscous response of the base course and subgrade materials is intensified. Hence, a typical structural inertial damping factor 5% is also introduced in these underlying materials for energy dissipation as viscoelastic materials (Al-Qadi et al., 2008). For bound materials in the base course and subgrade, the inertial damping factor is eliminated to compare with unbound materials and evaluate the individual effect of inertial damping factor.

**Table 3.1 Information of Pavement Type 1-5 in the 3D FE Simulation**

| Pavement Type | | 1 | 2 | 3 | 4 | 5 |
|---|---|---|---|---|---|---|
| Pavement Structure | | Asphalt over unbound base | Asphalt over stabilized base | Concrete over unbound base | Concrete over stabilized base | Asphalt over asphalt-treated base |
| Material | Surface | Viscoelastic | Viscoelastic | Elastic | Elastic | Visco-elastic |
| | Base | Damped elastic | Elastic | Damped elastic | Elastic | Visco-elastic and damped elastic |

**Table 3.2 Information of Material Properties and Moving Speeds in the 3D FE Simulation**

| Pavement Type | | 1 | | 2 | | 3 | | 4 | |
|---|---|---|---|---|---|---|---|---|---|
| Layer | Surface | $E_1$, MPa | 428 | $E_1$, MPa | 428 | E, MPa | 28000 | E, MPa | 28000 |
| | | m | 0.363 | m | 0.363 | | | | |
| | | $\delta$ ($^\circ$) | 32.67 | $\delta$ ($^\circ$) | 32.67 | | | | |
| | Base | E, MPa | 517 | E, MPa | 517 | E, MPa | 517 | E, MPa | 517 |
| | Subgrade | E, MPa | 31 | E, MPa | 31 | E, MPa | 31 | E, MPa | 31 |

**Table 3.2 Continued**

| Pavement Type | | 5 | | | | | |
|---|---|---|---|---|---|---|---|
| Deterioration Stage | | I | | II | | III | |
| Layer | Surface | $E_1$ , MPa | 428 | $E_1$ , MPa | 220 | $E_1$ , MPa | 141 |
| | | m | 0.363 | m | 0.401 | m | 0.447 |
| | | $\delta$ ( $^\circ$ ) | 32.67 | $\delta$ ( $^\circ$ ) | 36.09 | $\delta$ ( $^\circ$ ) | 40.23 |
| | Asphalt-treated base | $E_1$ , MPa | 119 | $E_1$ , MPa | 70 | $E_1$ , MPa | 17 |
| | | m | 0.202 | m | 0.259 | m | 0.351 |
| | | $\delta$ ( $^\circ$ ) | 18.18 | $\delta$ ( $^\circ$ ) | 23.31 | $\delta$ ( $^\circ$ ) | 31.59 |
| | Unbound base | E, MPa | 517 | E, MPa | 517 | E, MPa | 517 |
| | Subgrade | E, MPa | 31 | E, MPa | 31 | E, MPa | 31 |
| Moving Speed | | 24 km/h, 40 km/h, 64 km/h, and 80 km/h | | | | | |

In addition to the Prony series as Equation 2.1, a fractional power of time can also describe the modulus varying with time as Equation 3.4,

$$E(t) = E_1 t^{-m} \tag{3.4}$$

where $E(t)$ is the relaxation modulus; and $E_1$, $m$ are material coefficients. An approximate relationship between the power-law function coefficient m and the phase angle $\delta$ (radius) was developed for viscoelastic materials as in Equation 3.5 (Lytton, 1989).

$$\delta = \frac{\pi}{2} m \tag{3.5}$$

By using the curve fitting, models characterizing the same viscoelastic material can be transformed from one to another. Surface and asphalt-treated materials described by

Equation 3.4 with parameters listed in Table 3.2 are transformed into Equation 2.1 with calibrated model coefficients, which are then applied in ABAQUS.

The deflection basin of the pavement from the ABAQUS is composed of deflection data at discrete points, of which the number is controlled by the mesh size. Consequently, in order to accurately capture the maximum absolute value of the deflection basin, an appropriate continuous curve is needed to fit these discrete defection points. Therefore, a Fourier series function is applied to fit the discrete deflection data, which is expressed in Equation 3.6,

$$d(x) = a_0 + \sum_{i=1}^{N} a_i \cos(\omega x) + b_i \sin(\omega x) \tag{3.6}$$

where $d$ is the vertical deflection with the distance $x$ from the loading center; and $a_0$, $a_i$, $b_i$, $\omega$ are fitting parameters. Then the fitting curve of the deflection basin is used to determine the length of the basin and lag distance. Figure 3.7 shows an example of the comparison between the fitted deflection basin and deflection data from the ABAQUS. It is clear that the Fourier series function works well with the deflection basin.

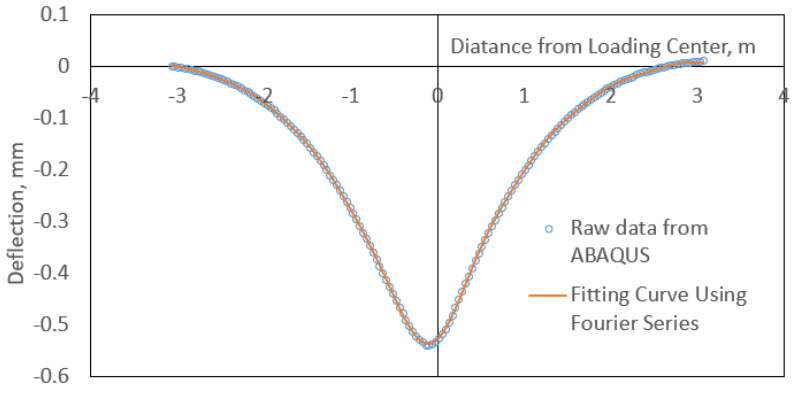


**Figure 3.7 Example of Comparison of Deflection Basins Using Data from ABAQUS and Fourier Series Function**

To illustrate effects of material properties on pavement responses under moving loads, the moving loads of the same speed are executed on pavement Types 1-4, of which Type 1-2 represent flexible pavements and Type 3-4 represent rigid pavements. The results are given in Table 3.3 and Figure 3.8. In both types of pavements, the asymmetry of the deflection basins is reflected with a steep leading edge and a shallow trailing edge. There are lag distances between the locations of the maximum deflection and the center of the loading which are shown clearly in flexible pavements. In addition, the lag distance increases and the magnitude of the deflection basin decreases as the damping factor of the base course is considered. It indicates that the asymmetry of the deflection basin is caused by both material viscoelasticity and damping factor, which in turn points out the significance of considering these two factors in the analysis of pavement systems.

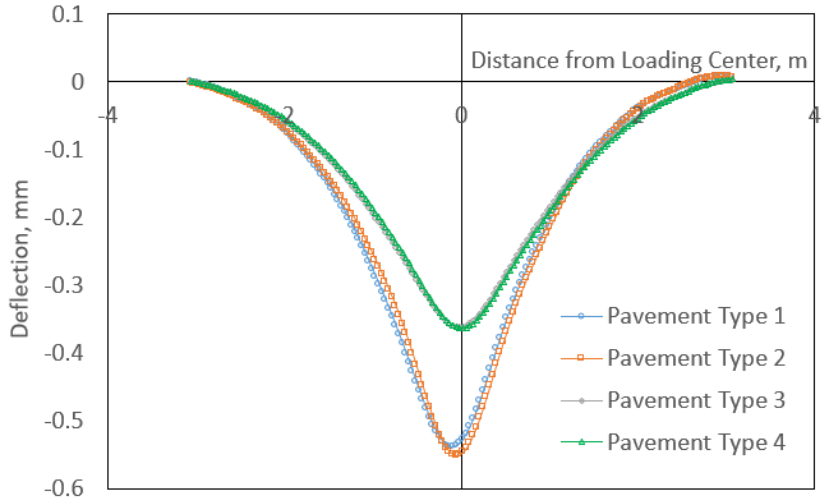


**(a) Moving Load v=80 km/h**

**Figure 3.8 Deflection Basins of Pavement Type 1-4 under Moving Loads**

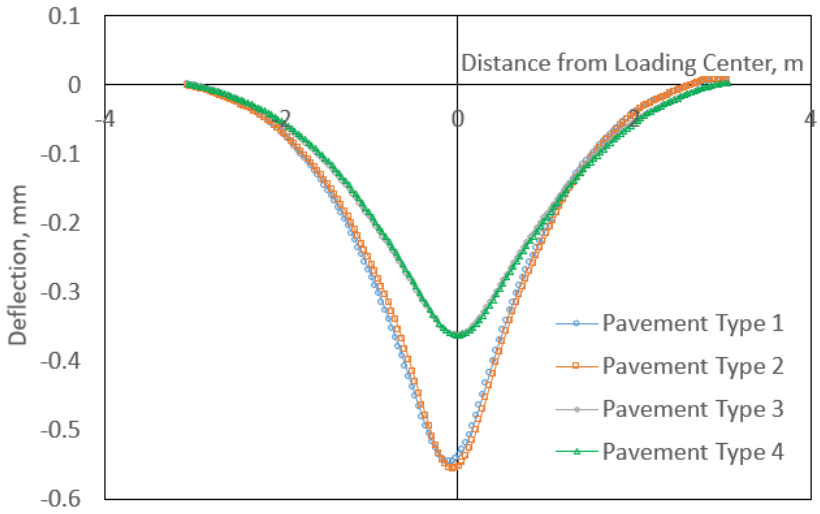


**(b) Moving Load v=64 km/h**

**Figure 3.8 Continued**

**Table 3.3 Lag Distance and Lag Angle of Pavement Type 1-4 under Moving Loads**

| Moving Speed, km/h | Pavement Type | 1 | 2 | 3 | 4 |
|---|---|---|---|---|---|
| 80 | Lag Distance, cm | 10.54 | 5.49 | 2.09 | 0 |
| | Lag Angle, degree | 6.66 | 3.45 | 1.28 | 0 |
| 64 | Lag Distance, cm | 9.06 | 4.86 | 1.29 | 0 |
| | Lag Angle, degree | 5.7 | 3.04 | 0.79 | 0 |

Since the viscoelasticity of materials and damping factor are considered in this study, the time-dependent properties such as modulus should be reflected in the pavement responses under different lengths of loading duration. Figure 3.9 shows deflection basins of the pavement model under different moving loads. As illustrated in Figure 3.9, the asymmetry of the deflection basins can be seen clearly from the steep leading edge and shallow trailing edge. The lag distance between the maximum

deflection and loading center exists in most deflection basins. Especially, when comparing the magnified bottom part of each deflection basin, an obvious trend shows that with the increase of the moving speed, the maximum deflection decreases and the lag distance increases, which is also seen from results in Table 3.4. Figure 3.9 and Table 3.4 demonstrate the sensitivity of the deflection basin to the speed of the moving load.

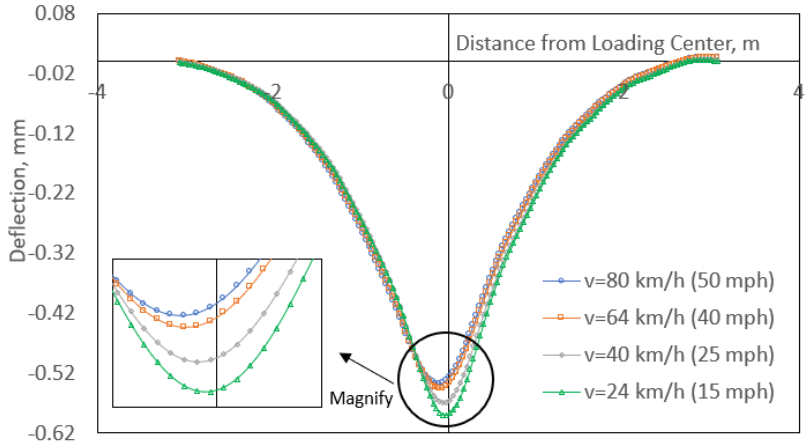


**(a) Pavement Type 1**

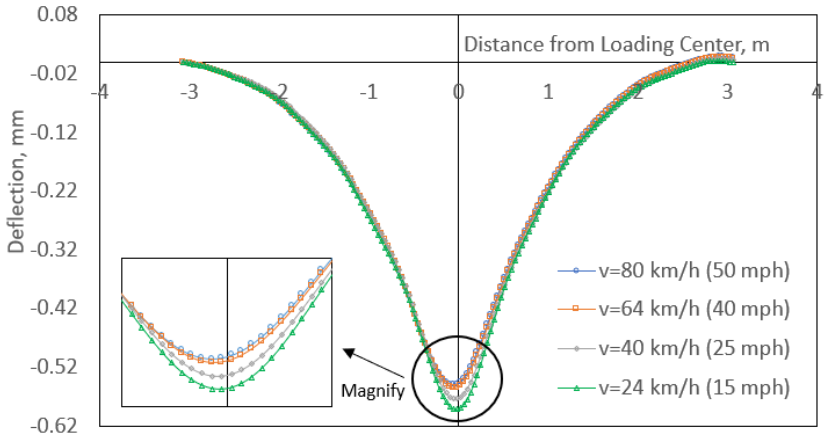


**(b) Pavement Type 2**

**Figure 3.9 Deflection Basins of Pavement Type 1-5 under Four Moving Loads**

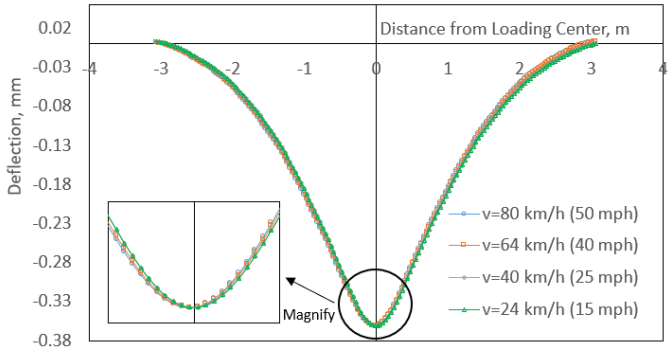


**(c) Pavement Type 3**

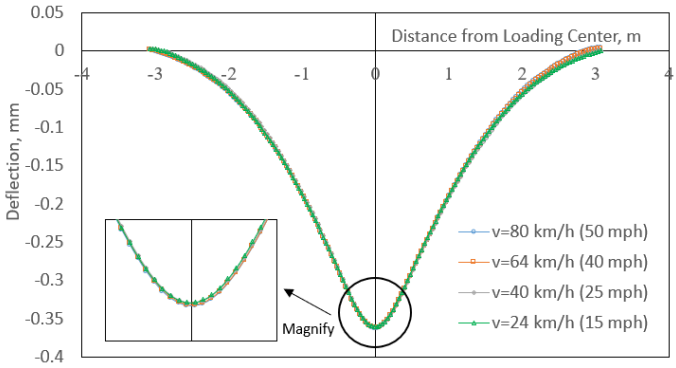


**(d) Pavement Type 4**

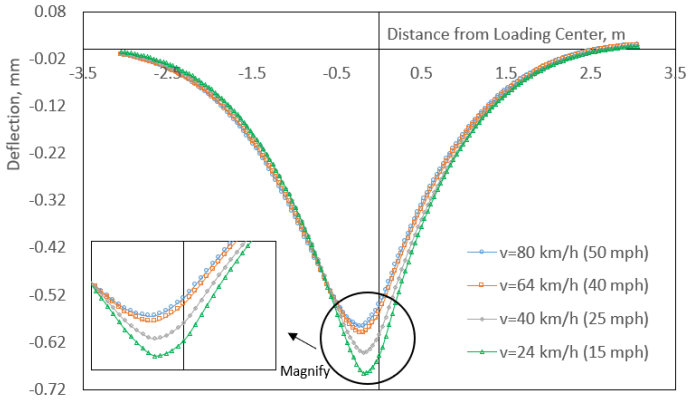


**(e) Pavement Type 5 at Deterioration Stage I**

**Figure 3.9 Continued**

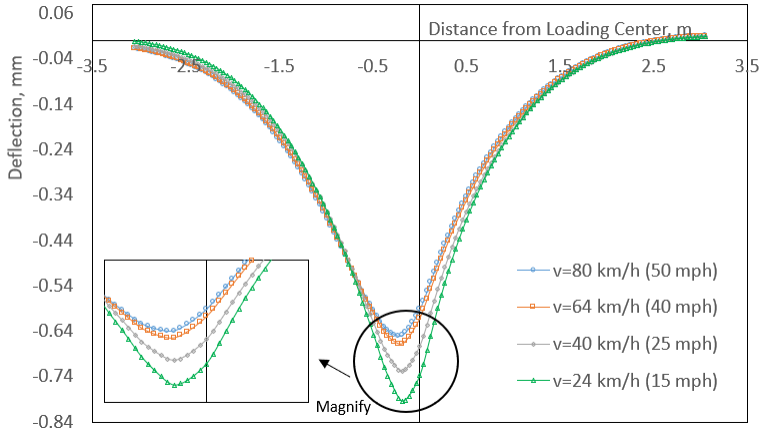


**(f) Pavement Type 5 at Deterioration Stage II**

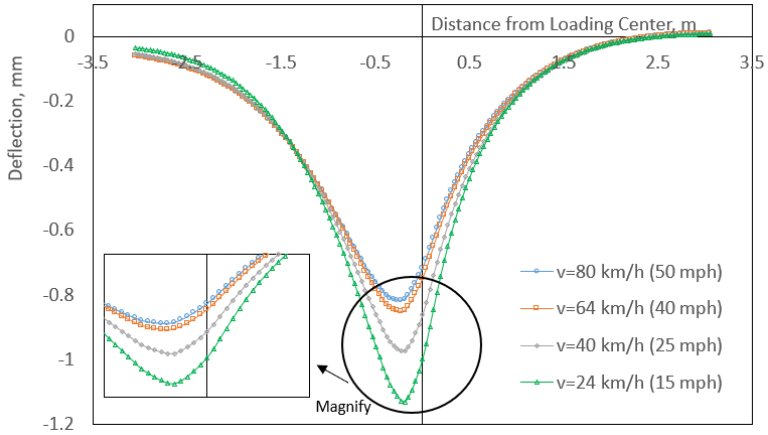


**(g) Pavement Type 5 at Deterioration Stage III**

**Figure 3.9 Continued**

**Table 3.4 Lag Distance and Lag Angle of Pavements under Four Moving Loads**

**(a) Pavement Type 1-4**

| Deflection Basin Parameter | | Lag Distance, cm | | | | Lag Angle, degree | | | |
|---|---|---|---|---|---|---|---|---|---|
| Pavement Type | | 1 | 2 | 3 | 4 | 1 | 2 | 3 | 4 |
| Speed of Load, km/h | 80 | 10.5 | 5.5 | 2.1 | 0 | 6.7 | 3.5 | 1.3 | 0 |
| | 64 | 9.1 | 4.9 | 1.3 | 0 | 5.7 | 3.0 | 0.8 | 0 |
| | 40 | 5.4 | 3.4 | 0.1 | 0 | 3.1 | 2.1 | 0.04 | 0 |
| | 24 | 3.4 | 2.7 | 0.1 | 0 | 1.9 | 1.6 | 0.07 | 0 |

**(b) Pavement Type 5**

| Deflection Basin Parameter | | Lag Distance, cm | | | Lag Angle, degree | | |
|---|---|---|---|---|---|---|---|
| Pavement Type | | 5 | | | 5 | | |
| Deterioration Stage | | I | II | III | I | II | III |
| Speed of Load, km/h | 80 | 23.3 | 24.2 | 28.1 | 14.9 | 15.4 | 17.8 |
| | 64 | 21.9 | 22.9 | 26.6 | 14.1 | 14.6 | 16.9 |
| | 40 | 18.3 | 19.6 | 23.6 | 12.0 | 12.8 | 15.5 |
| | 24 | 16.2 | 17.5 | 21.9 | 10.5 | 11.5 | 14.0 |

## 3.3 Determination of Fatigue Damage in Flexible Pavements Using Pavement Responses under Moving Loads

As described in Section 1.2, it is widely known that the dynamic modulus and phase angle can represent the current damaged condition of a pavement material, especially pointing out the specific stage during its whole service life. The dynamic modulus and phase angle varying with load cycles are shown in Figure 3.10. In the region of macro-crack formation, the value of the modulus goes through a rapid decrease. Reese (1997) has found that at the starting point of this region, the phase angle of the

mixture reached its maximum value, then it began to drop quickly. Such a pattern shows that the phase angle is a good indicator of fatigue damage and failure of the material.

As shown in Figure 3.10, the change of the dynamic modulus and phase angle reflects different stages of deterioration of the pavement material. A potential application of such features is the advance warning of pavement deterioration, which is necessary for optimal plans of preventive maintenance and rehabilitation. In the current state of practice, the deflection (e.g. from the FWD) is usually taken as an indicator of pavement conditions. However, the change of the deflection value is not only attributed to the loss of structural strength due to damage, but also the geometric discontinuity of the pavement. For instance, a large value of the deflection could be caused by the occurrence of cracking and rutting, or the existence of slab joints or softening due to moisture infiltration. As a result, a measurement that is directly and solely related to pavement deterioration conditions should be adopted for the purpose of advance warning. Given the similarity between the phase angle in Equation 3.1 and the lag angle in Equation 3.2, the lag angle is proposed herein as such a measurement. It is obtained easily from a moving deflection basin, and, as a hypothesis, it has a close relationship with the phase angle of the material, which is indicative of pavement conditions in terms of the initiation and growth of fatigue cracks.

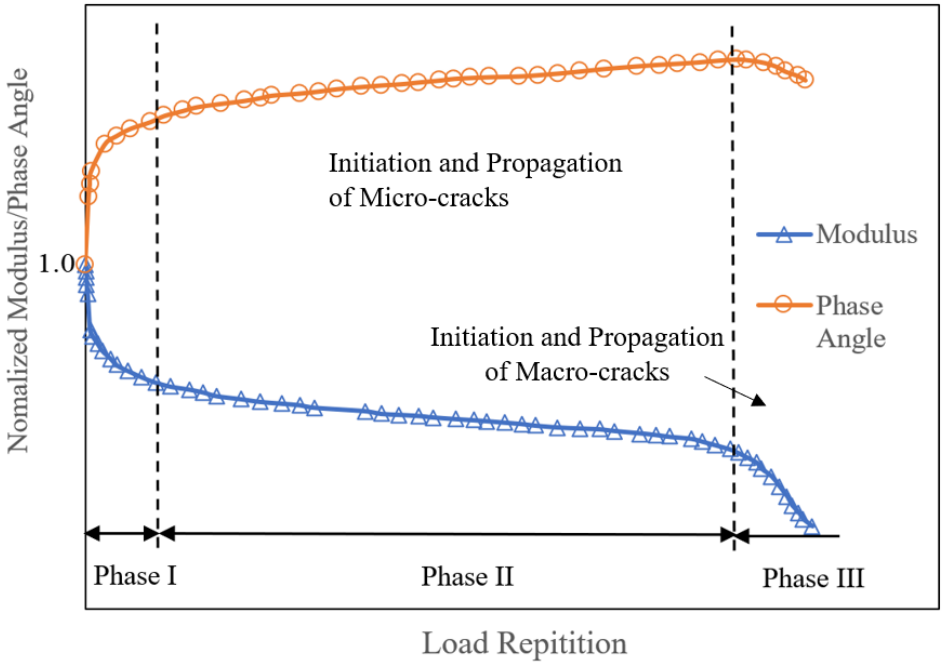


**Figure 3.10 Normalized Modulus and Phase Angle with Load Cycles in a Fatigue Test**

For viscoelastic surface and viscoelastic base (asphalt-treated base), the change of the material property is included to simulate the deterioration of the pavement surface with service time, as designated by Stage I, Stage II and Stage III for the pavement type 5 in Table 3.2.

To study the effects of deterioration condition of a pavement on deflection basins under moving loads, the deflection basins of the pavement model at three typical stages of its service life under the same moving load are illustrated in Figure 3.11. The variation of a pavement's fatigue cracking deterioration conditions is reflected in the values of the modulus and the phase angle as presented in Table 3.2. With the increase of load cycles, the modulus of pavement materials decreases while the phase angle increases. Similar to Figure 3.1, the two main points (steep leading edge and shallow

trailing edge; the lag distance between the maximum deflection and the loading center) are observed in each complete deflection basin. From the magnified lower parts in Figure 3.11, it can be concluded that the maximum deflection increases when the increasing number of load cycles causes damage to the pavement, which agrees with the common understanding. Furthermore, the change of the lag distance is obvious from Stage 1 to Stage 3. This is because the viscous response of pavement materials is enhanced, which is attributed to the growing cracks and voids in the pavement surface layer, and moisture accumulation and plastic deformation in the base course layer. Such changes will have effects on material properties of the layers and eventually be reflected in the deflection basins.

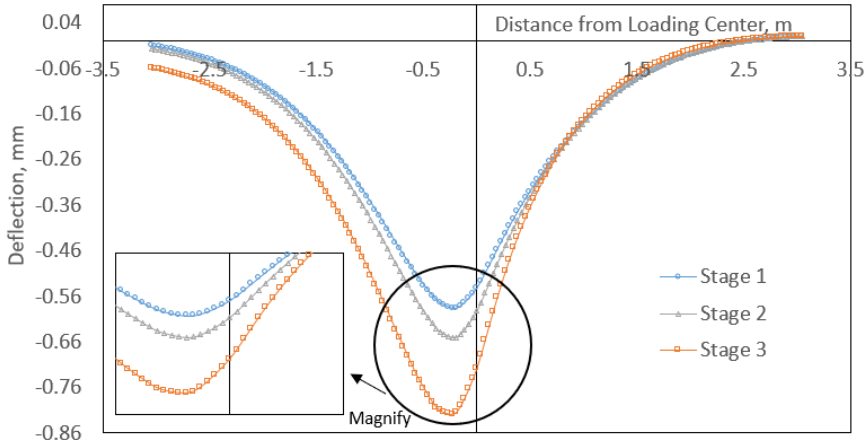


**(a) Moving Load v=80 km/h**

**Figure 3.11 Deflection Basins of Pavement at Different Deterioration Stages under Moving Loads**

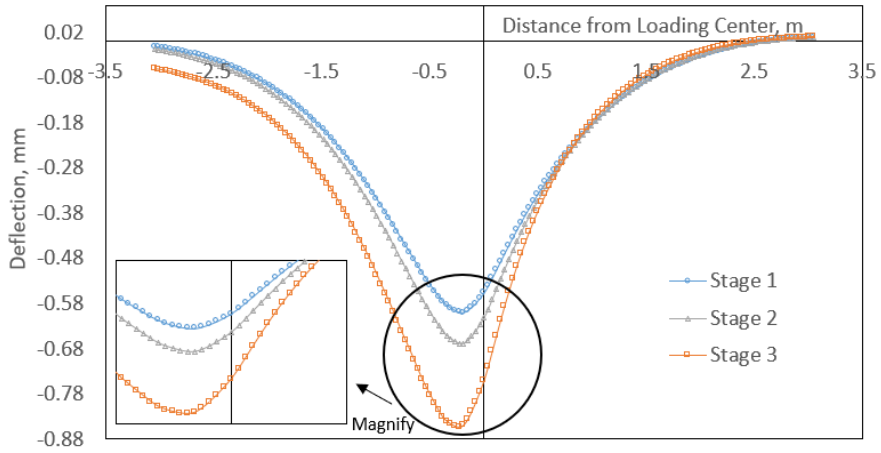


**(b) Moving Load v=64 km/h**

**Figure 3.11 Continued**

Figures 3.9(e), 3.9 (f), 3.9(g) and Figure 3.11 show that the deflection basins of the pavement model in different deterioration conditions and under different moving speeds. The results illustrate that the deterioration condition of the pavements affects the deflection basin in terms of its asymmetry and maximum deflection, which are also sensitive to the speed of the moving load. Therefore, it is natural to consider the possibility of visualizing the deterioration condition of a pavement directly from its deflection basin under a moving load. The lag angle defined in Equation 3.2 represents the characteristics of both the deflection basins (length and lag distance) and moving loads (speed). The relationship between the pavement lag angle and the material phase angle is studied herein. Figure 3.12 shows the correlations between the lag angles calculated from the deflection basins and phase angles of both the surface layer and asphalt-treated base course. The results provide evidence for a potential relationship

between the newly defined lag angle and the viscoelastic properties of pavement materials.

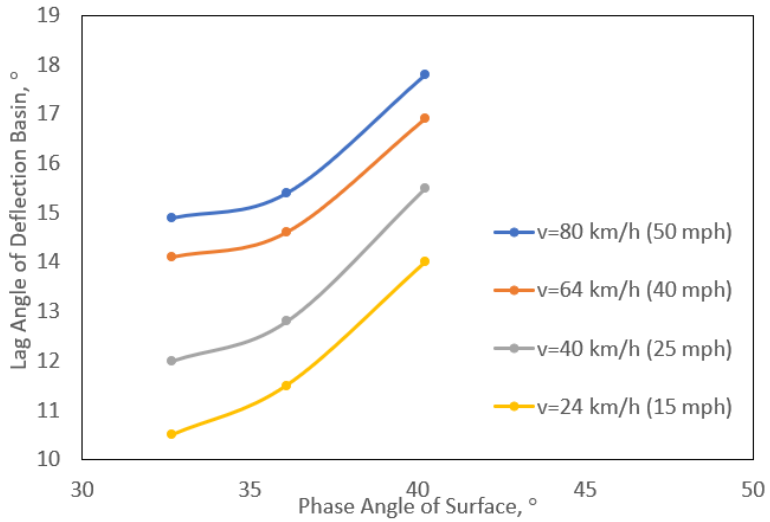


**(a) Surface Layer**

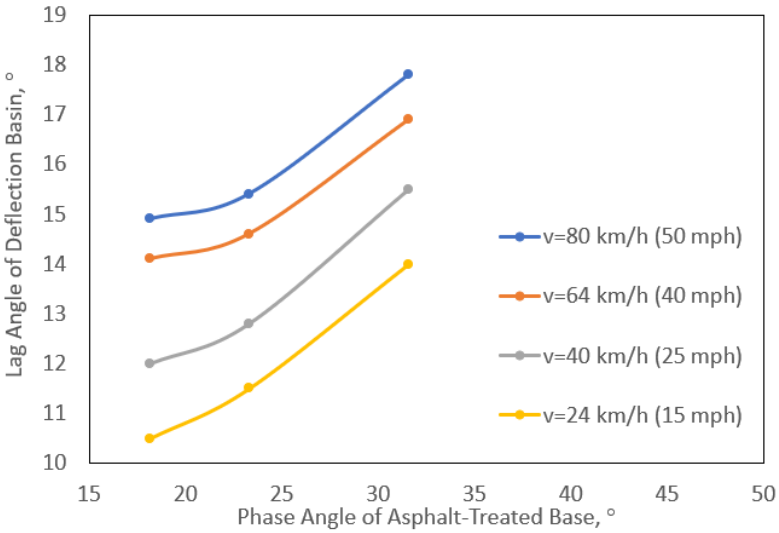


**(b) Base Course**

**Figure 3.12 Relationship between Lag Angle and Phase Angle of Pavement Materials**

Recently, a project was conducted to simulate pavements under moving loads and compare numerical results with data measured from field tests with the RWD and the TSD (Rada et al., 2016; Nasimifar et al., 2017). As introduced in previous sections, the RWD measures the deflection of a pavement while the TSD applies the Doppler technique to measure the vertical deflection velocity. The slope of the deflection basin is the ratio of the deflection velocity to the moving velocity (Soren et al., 2008). Based on the simulation results and field measurements from this project, a comparative study is performed. A new 3D pavement model is constructed following the method presented in Section 3.2. The pavement model has the same structure and material properties as those in the project using the RWD and the TSD. The viscoelastic material properties of the surface layer were measured from the laboratory tests; the elastic properties of the base and subgrade were obtained from the FWD measurements (Rada et al., 2016; Nasimifar et al., 2017). Furthermore, the material properties such as the inertial damping and density which are not available in the literature are considered in the 3D pavement model and taken typical values.

Figure 3.13 shows the results of the comparison. The FE data are provided by the 3D pavement model considering material viscoelasticity and structural inertial damping. The asymmetry of the deflection basin can be seen clearly and the lag distance occurs between locations of the loading center and the maximum deflection from Figure 3.13. The two discrete data points in Figure 3.13(a) are measured by the RWD, and six discrete data points of the deflection slope in Figure 3.13(b) are measured by the TSD. Considering the variability in the field measurements by the RWD and TSD, the match

between the FE simulation results and field data is good, which proves the simulation method described in this section is correct.

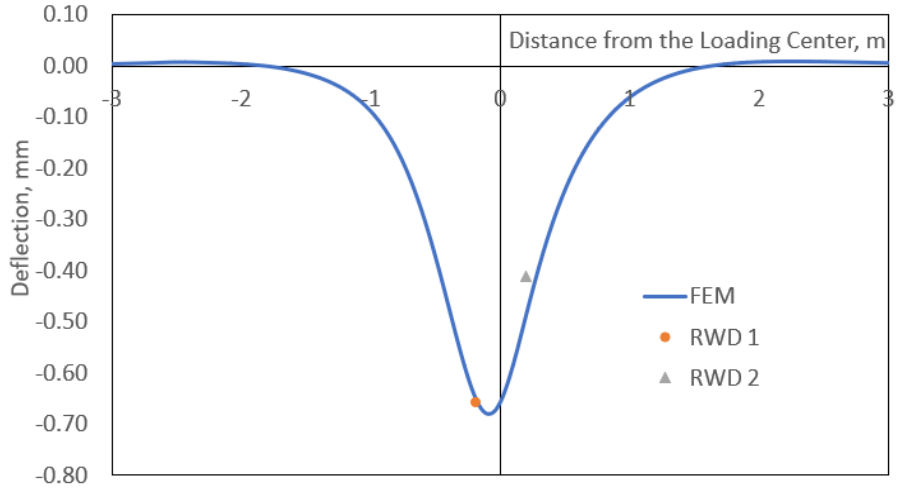


**(a) RWD Data**

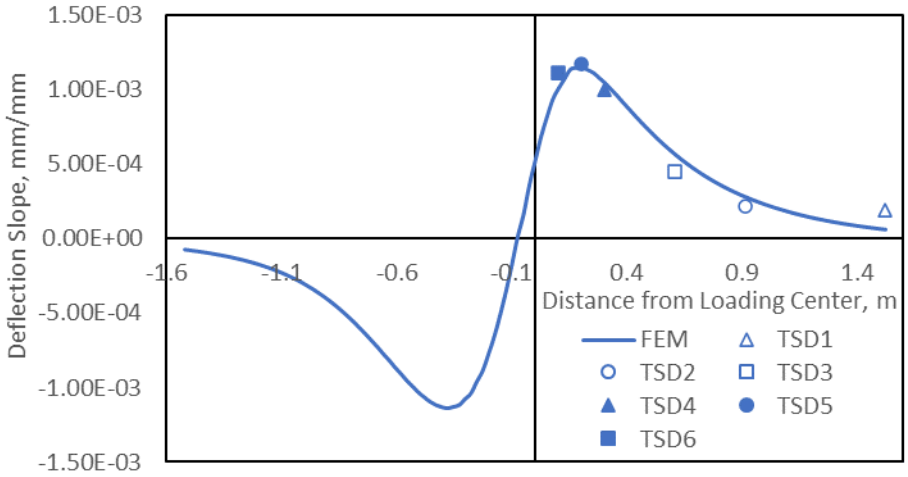


**(b) TSD Data**

**Figure 3.13 Comparison of the 3D FE Model Results and Field Data**

### 3.4 Determination of Fatigue Damage in Flexible Pavements Using Pavement Responses under Equivalent Stationary Dynamic Loads

Considering applications of NDT devices like the FWD and 2D axisymmetric FE models in simulating pavements in service, determination of fatigue damage from pavement responses under stationary dynamic loads is still of necessity. Moreover, with the load equivalency built in Section 2, fatigue damages determined from 3D FE models with moving vehicular loads and 2D axisymmetric models with equivalent stationary dynamic loads should correlate with each other. Such correlation is likely to provide evidences for evaluating flexible pavement conditions directly from 2D axisymmetric models, which can save much time and storage space than using 3D models.

FE models are the same as those in Section 2.2. Instead of using obtained equivalent relationship between moving vehicular loads and stationary dynamic loads, a revision is made in the FE model updating introduced in Section 2. As illustrated in Figure 2.4, once the FE model updating with the AI algorithm starts, it will stop until the criterion is satisfied, which can be the total iteration number reaching the upper limit or the objective function value meeting the requirement. However, if researchers want to do the sensitivity analysis for different objective functions or for parameters in the AI algorithm, they have to start over. Therefore, the kriging model is implemented in the model updating as a surrogate model in this section.

The kriging model is a half-parameterized interpolation model which includes parametric and non-parametric parts (Qin et al., 2018a). It provides an explicit relationship for the implicitly-related parameters. Different from the curve fitting

technique or models based on simple functions (i.e. the response surface model which is based on a polynomial function), the kriging model considers the global trend as well as the random errors of data samples (Liu et al., 2014; Qin et al., 2018a). The relationship between model inputs and predicted outputs is expressed as Equation 3.7 (Qin et al., 2018a),

$$Y(x) = \sum_{i=1}^{n} \beta_i f_i(x) + Z(x) \tag{3.7}$$

where $Y$ are predicted outputs; $x$ are model inputs; $\beta$ is kriging model coefficient; $f$ is simple fitting function (i.e. constant, linear function or quadratic function, etc.); $Z$ is a model of a Gaussian and stationary random process with zero mean; and $n$ is the number of fitting functions. In this study, model inputs are the pressure magnitude and cycle of the stationary dynamic load and outputs are the deflection magnitude and the time to reach it. The training of the kriging model can be summarized as solving for the kriging coefficients using pairs of model inputs and outputs obtained from FE models.

The kriging model is popular in geostatistics and spatial statistics, which sketch a domain from sampled data. Similarly, we assumed the kriging model trained with data which are sampled from the solution domain can be used for prediction. The sampling method used in this study is Latin hypercube sampling (LHS), which was first proposed by McKay in 1979 (McKay et al., 1979). It proved to be a good method to select representative input values in computer experiments since it considers the total number of required samples and their relative positions to avoid data concentration as random sampling (McKay et al., 1979; Qin et al., 2018b).

Accordingly, the flow chart of the new FE model updating is changed to Figure 3.14, in which results of 400 2D axisymmetric FE models are separated into 300 for kriging model training and 100 for kriging model validation. Figure 3.15 shows the results of the kriging model validation, which is the comparison of structural responses obtained from the FE models and predicted by the trained kriging model. The $R^2$ for both responses are close to 1, which reflects high accuracy of the trained kriging model. The trained kriging model can be called anytime to predict pavement responses within seconds. It further improves the efficiency of the FE model updating with more flexibility.

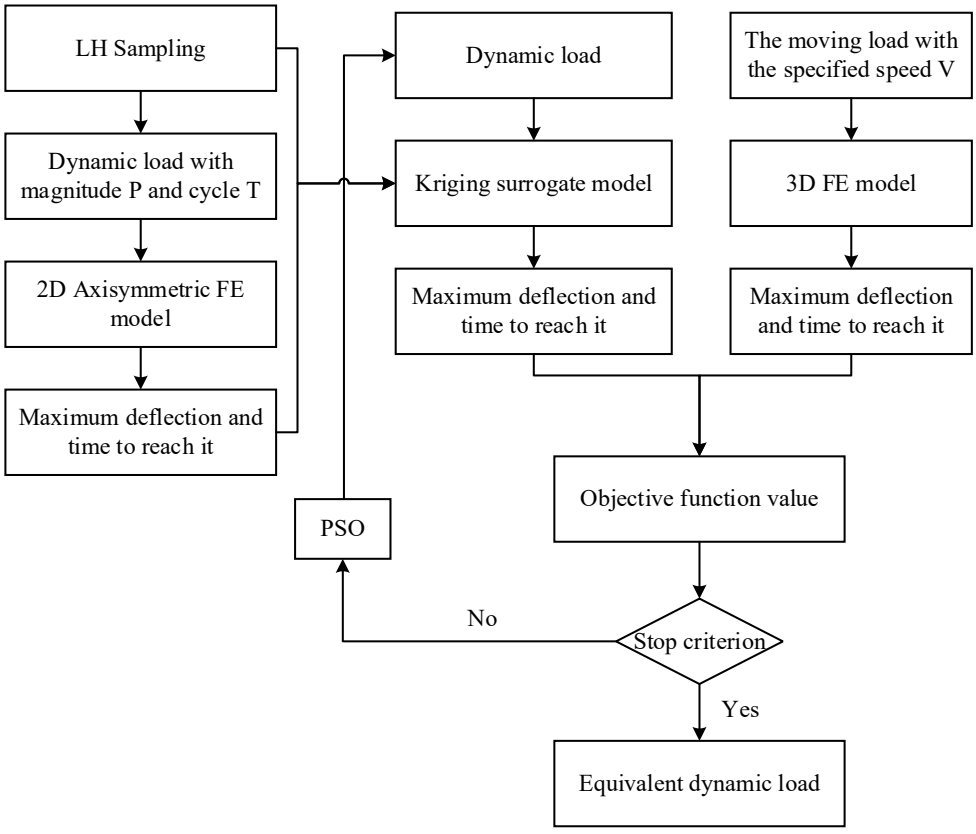


**Figure 3.14 Flow Chart of the FE Model Updating with Kriging Model and PSO Algorithm**

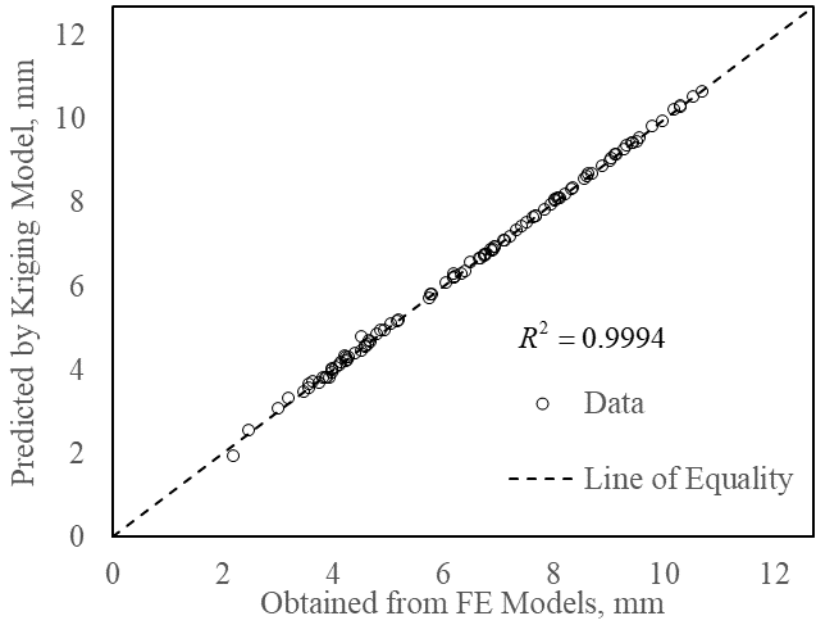


**(a) The Maximum Deflection**

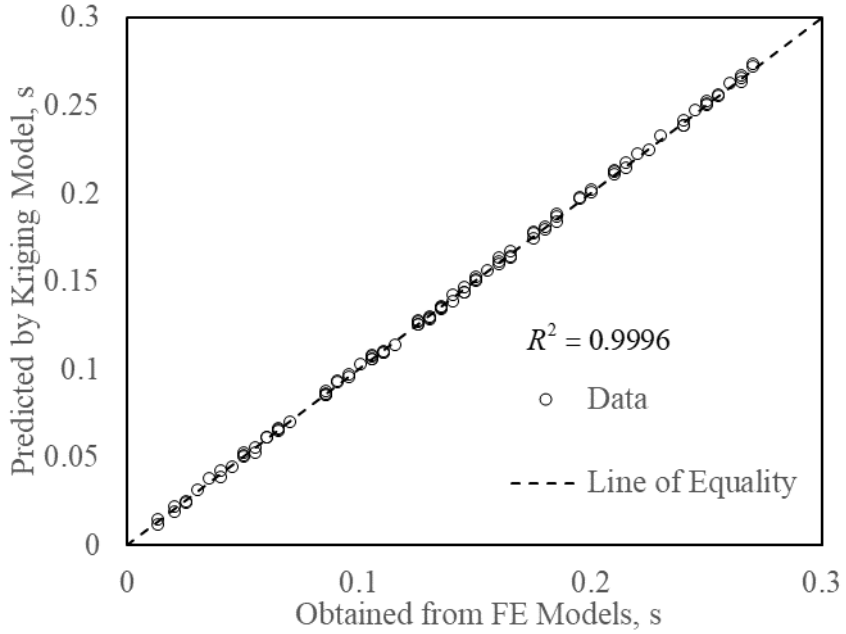


**(b) Time to Reach the Maximum Deflection**

**Figure 3.15 Comparison of Model Responses Obtained from FE Models and Predicted by Kriging Model**

With the new model updating, equivalent stationary dynamic loads for moving vehicular loads with pressure magnitude 0.7 MPa and 8 moving speeds are presented in Table 3.5. To check the accuracy, these parameters are used in the newly-built 2D axisymmetric FE models to compare the vertical deflection magnitude and time to reach it with those in the 3D FE models. Results are shown in Figure 3.16. The high values of $R^2$ validates the success of the new model updating.

**Table 3.5 Magnitudes and Cycles of Equivalent Dynamic Loads for Moving Loads**

| Speed of the Moving Load, km/h | Equivalent Dynamic Load Parameters | |
|---|---|---|
| | Pressure Magnitude P, MPa | Cycle T, s |
| 40.23 | 0.4886 | 0.3163 |
| 56.33 | 0.4841 | 0.2219 |
| 72.42 | 0.4748 | 0.1687 |
| 80.47 | 0.4750 | 0.1500 |
| 96.56 | 0.4821 | 0.1204 |
| 112.65 | 0.4825 | 0.1018 |
| 128.75 | 0.4800 | 0.0856 |
| 160.93 | 0.4697 | 0.0635 |

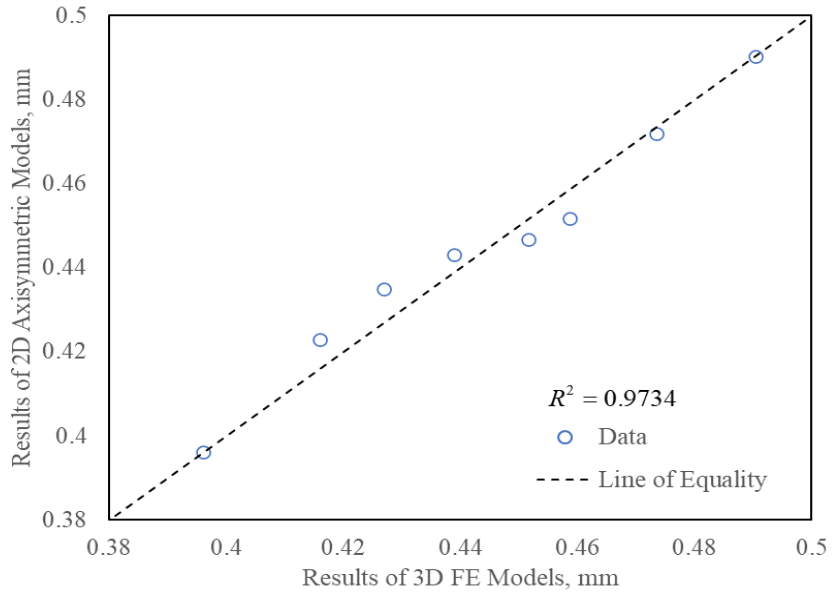


**(a) The Maximum Deflection**

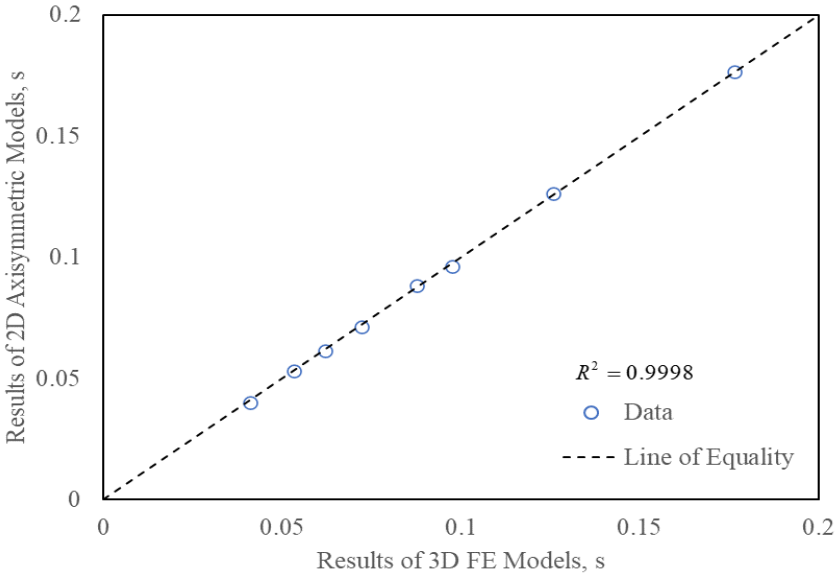


**(b) Time to Reach the Maximum Deflection**

**Figure 3.16 Comparison of Model Responses of 3D FE Models and 2D Axisymmetric FE Model**

For different deterioration conditions, the modulus and phase angle of the pavement surface material are adjusted to follow the similar trends as Figure 3.10. With the deteriorating condition of the material, the dynamic modulus decreases while the phase angle increases. Ratios of the dynamic modulus and the phase angle at different deterioration conditions are presented in Table 3.6, in which the reference condition is presented in Table 2.1 and the measuring frequency is assumed to be 10 Hz.

**Table 3.6 Dynamic Modulus and Phase Angle of Pavement Surface Material at Different Deterioration Levels**

| Deterioration Level $i$ | $\left\|E^*\right\|_i / \left\|E^*\right\|_0$ | $\left\|E^*\right\|_i$, MPa | $\varphi_i / \varphi_0$ | $\varphi_i$, ° |
|---|---|---|---|---|
| 0 | 1.0 | 2.99E+3 | 1.0 | 29.44 |
| 1 | 0.9 | 2.68E+3 | 1.1 | 32.38 |
| 2 | 0.8 | 2.39E+3 | 1.3 | 38.27 |
| 3 | 0.7 | 2.09E +3 | 1.4 | 41.21 |
| 4 | 0.6 | 1.79E +3 | 1.6 | 47.10 |
| 5 | 0.5 | 1.49E +3 | 1.8 | 52.99 |

To implement the material properties at Deterioration Level 1-5 in Table 3.6 into ABAQUS, the Prony Series coefficients are obtained by minimizing the differences between the dynamic modulus $\left|E^*\right|$ and phase angle $\varphi$ listed in Table 3.6 and predicted by Equation 3.8 and Equation 3.9 (Zhang et al., 2016),

$$\left|E^*(\omega)\right| = \sqrt{[E'(\omega)]^2 + [E''(\omega)]^2} \tag{3.8}$$

$$\varphi = \tan^{-1}\left[\frac{E''(\omega)}{E'(\omega)}\right] \tag{3.9}$$

in which,

$$E'(\omega) = E_\infty + \sum_{i=1}^{N} \frac{\omega^2 \tau_i^2 E_i}{1 + \omega^2 \tau_i^2} \tag{3.10}$$

$$E''(\omega) = \sum_{i=1}^{N} \frac{\omega \tau_i E_i}{1 + \omega^2 \tau_i^2} \tag{3.11}$$

where $E'(\omega)$ is the storage modulus; $E''(\omega)$ is the loss modulus; $\omega$ is the loading frequency; and $E_\infty$, $E_i$, $\tau_i$, $N$ are Prony series parameters as those in Equation 2.1.

The pavement structures with surface materials representing 6 deterioration conditions are applied with 8 equivalent dynamic loads representing the moving loads at 8 different speeds. 48 2D axisymmetric FE models in total are built and the deflection histories at the loading center are analyzed. Following the idea of the lag angle which is defined from the dimension of the deflection basins of the pavement surface under moving loads in 3D FE models, a similar concept is proposed to evaluate the deterioration condition of the pavement using its deflected profile in the 2D axisymmetric model.

Figure 3.17 shows the histories of normalized load and deflection under the dynamic load of equivalent magnitude and cycle time for a moving load of 80.47 km/h. There is an obvious time lag between the maximum load and deflection in the plot. In order to utilize this characteristic to evaluate the deterioration condition of the flexible pavement, a similar term is defined as Equation 3.12 and called the equivalent lag angle since it is also from the deflection of the pavement surface but in the 2D axisymmetric model with the equivalent dynamic load.

$$\delta_{equi} = 2\pi \frac{\Delta t}{T} \tag{3.12}$$

where $\delta$ is the equivalent lag angle of the pavement (radius); $\Delta t$ is the time lag between the maximum load and deflection; and $T$ is the cycle time of the deflection basin.

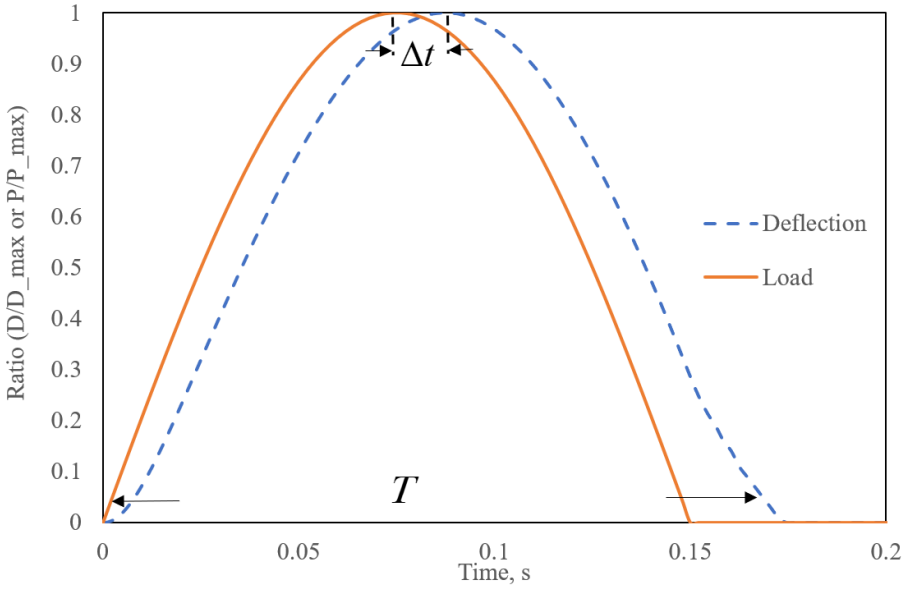


**Figure 3.17 Normalized Load and Deflection Histories under the Moving Load of 80.47 km/h**

Table 3.7 presents the calculated equivalent lag angles for a total of 48 cases and Figure 3.18 shows the correlations between the equivalent lag angle of the pavement and the phase angle of the surface material under different moving loads. The figure shows that the equivalent lag angle increases with the increase of the phase angle and the speed of the moving load. Such trend is similar to and can also be found in the lag angle calculated from 3D models with moving loads. It indicates that a causal relation between the material properties of the flexible pavement surface and the structural response of the pavement.

**Table 3.7 Equivalent Lag Angle (°) of Pavements of Different Deterioration Conditions under Moving Loads of Different Speeds**

| Phase Angle, ° | Speed of the Moving Load, km/h | | | | | | | |
|---|---|---|---|---|---|---|---|---|
| | 40.23 | 56.33 | 72.42 | 80.47 | 96.56 | 112.65 | 128.75 | 160.93 |
| 29.44 | 19.00 | 24.27 | 26.44 | 27.39 | 29.81 | 32.99 | 37.38 | 43.35 |
| 32.38 | 19.01 | 24.26 | 26.48 | 27.33 | 29.94 | 33.21 | 37.58 | 43.87 |
| 38.27 | 19.83 | 25.50 | 27.86 | 28.83 | 31.44 | 34.67 | 38.98 | 45.18 |
| 41.21 | 19.86 | 25.62 | 28.14 | 29.13 | 31.64 | 34.90 | 39.30 | 45.44 |
| 47.10 | 21.41 | 27.48 | 30.04 | 31.08 | 33.62 | 36.82 | 41.06 | 47.22 |
| 52.99 | 23.14 | 29.15 | 31.64 | 32.57 | 34.91 | 38.06 | 42.17 | 48.13 |

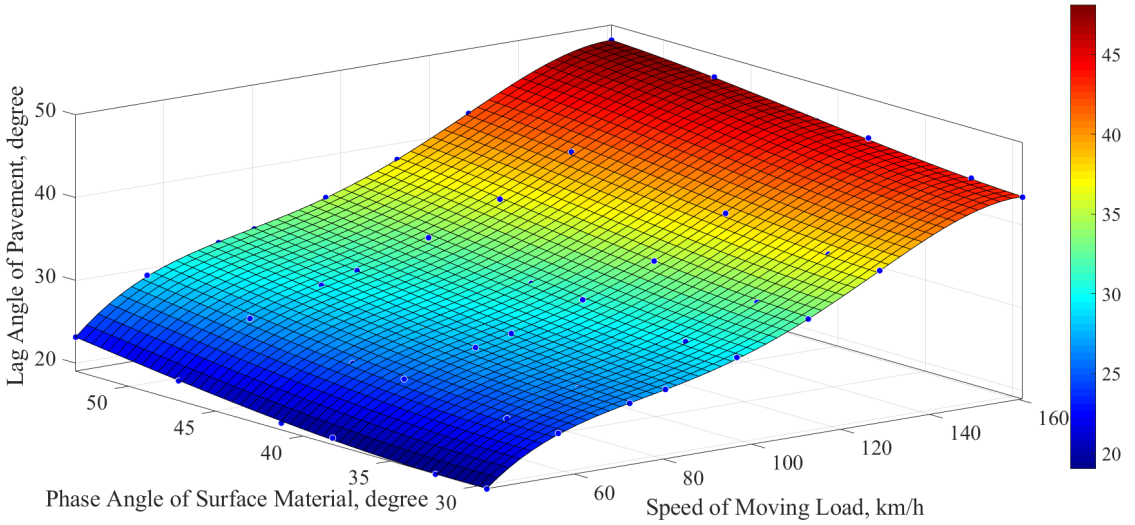


**Figure 3.18 Relationship between Phase Angle, Equivalent Lag Angle and Moving Speed**

# 4. INVERSE ANALYSIS OF AGING IN FLEXIBLE PAVEMENTS

## 4.1 Introduction

As introduced in Section 1.1, asphalt mixtures closer to the pavement surface are more affected by aging and have higher stiffness, which results in a modulus decrease and contributes to a modulus gradient with depth in the AC layer of flexible pavements. The modulus gradient of asphalt concrete (AC) layers is a characteristic of flexible pavements. Numerous studies have revealed that it results from the synthetical effect of material properties, the service time of pavements, loading and environmental conditions. As viscoelastic materials, material properties of AC layers are sensitive to the temperature and frequency of the applied load (Lakes, 2009). The temperature gradient in AC layers was observed and studied in many researches (Kim et al., 1995; Buttlar et al., 2006; Nazarian and Alvarado, 2006; Wang and Al-Qadi, 2010b). It has been considered in the pavement design and evaluation for its effects on the modulus and critical responses in the AC layer (Houston et al., 2005; Zapata and Houston, 2008; Li et al., 2013). Similarly, the loading frequency significantly affects AC layers in terms of the stiffness and distress modes. Different from the laboratory condition in which samples can be under a uniform loading frequency, the frequency spectrum caused by traffic loads in the AC layer depends on the load and depth (Barksdale 1971; Brown 1973; McLean 1974; Al-Qadi et al., 2008; Ulloa et al., 2013; Wang and Li, 2016). Moreover, nonuniform distributions of the air void (Koohi et al., 2012; Yin et al., 2017;

Luo et al., 2018a) and the compaction degree (Hu, 2018) can contribute to the modulus variation in the AC layer as well.

It seems that the modulus gradient has potentials to serve as an indicator for the aging degree of flexible pavements. It was measured in the laboratory and associated with the aging degree of field cores in some researches (Koohi et al., 2012; Ling et al., 2017b). Therefore, this section aims to propose a method in determining the modulus gradient of the asphalt layer of flexible pavements from FWD tests, which are nondestructive to pavements. Moreover, as viscoelastic materials, the obtained modulus gradient using the proposed method is frequency-dependent.

### 4.2 Backcalculation of Asphalt Layer Properties Using FWD Tests

In addition to the structural indices, more information can be obtained from FWD tests. For example, deflection peaks or deflection histories at sensor locations can be used to backcalculate layer moduli and other pavement properties via inverse analysis (Magnuson et al., 1991; Meier and Rix, 1994; Hadidi and Gucunski, 2010; Kutay et al., 2011; Li and Wang, 2019).

Backcalculation methods can be divided into static backcalculation methods and dynamic backcalculation methods based on how the method considers the FWD load and pavement responses. In static backcalculation methods, the pavement is treated as a layered elastic system under a static load, which equals the magnitude of the FWD load. The pavement parameters are obtained by matching deflection peaks at sensor locations measured by the FWD and predicted by layered elastic theories. The programs

iteratively call the layered elastic solution with updated parameters or searching the database created by possible parameters, which is called the forward calculation scheme (Ameri et al., 2009). Representative static backcalculation softwares are Modulus (Liu and Scullion, 2001), ELMOD (The Dynatest Group, 2001), BAKFAA (2017), etc. Static backcalculation methods are widely used for the simplicity and fast computational speed. However, two characteristics of pavements may cause unreliable results, of which one is the shallow bedrock since most layered elastic theories assume a semi-infinite subgrade (Ameri et al., 2009). The other one is the discontinuity such as joints, cracks, thick and stiff surface layers (Ameri et al., 2009; Hadidi and Gucunski, 2010). Moreover, the modulus of AC layers cannot be entirely represented by an elastic modulus and layered elastic solutions cannot fully characterize flexible pavement responses under the FWD load.

Dynamic backcalculation methods can be further categorized into the time-domain backcalculation and frequency-domain backcalculation. The goal of the frequency-domain backcalculation is matching measured and predicted pavement responses under the unit load at different frequencies. The measured unit pavement responses are obtained from the complex division of the Fast Fourier Transform (FFT)-processed FWD load and deflection histories. The predicted unit pavement responses are typically obtained from forward frequency-domain computer programs (Magnuson, 1988; Uzan, 1994). As for the time-domain backcalculation, the match is required between deflection histories measured by the FWD and predicted from time-domain forward calculation schemes. In the software DBSID (Dynamic Backcalculation with

System Identification Method) (Fernando and Liu, 1999), pavement responses under the unit load at different frequencies are obtained from a frequency-domain forward computer program. These unit responses are then multiplied by the FFT-processed FWD load history to obtain the corresponding frequency-domain deflections. Following that, an inverse FFT is conducted to transfer deflections back to the time domain. The deflection histories in the time domain are finally applied in a sensitivity matrix to update pavement parameters (Uzan, 1994; Ameri et al., 2009). Alternatively, a layered viscoelastic solution based on the Boltzmann's superposition integral and Schapery's quasi-elastic theory was used in a forward calculation scheme to predict time-domain deflection histories under the FWD load (Kutay et al., 2011; Varma and Kutay, 2016). Typical backcalculated material properties of AC layers are the creep compliance (Fernando and Liu, 1999) and relaxation modulus (Kutay et al., 2011), which better describe time-dependent (or frequency-dependent) properties of AC layers.

In this section, the determination of the complex modulus gradient in AC layers is based on time histories of the load and deflections measured in an FWD test. Time histories of the load $F(t)$ (or the pressure $P(t)$) and deflections $Z(t)$ recorded in the FWD are processed as the reference (Magnuson, 1988). First, correct the discontinuity at the tail of the dataset and supplement the dataset with zeros to a normal size (1024) for the FFT. Next, apply FFTs to the revised $F(t)$ (or $P(t)$) and $Z(t)$ to obtain their expressions $F(\omega)$ and $Z(\omega)$ in the frequency domain. Following that, calculate the unit pavement deflection magnitude $H(\omega)$ as Equation 4.1. It is then multiplied by a standard FWD load magnitude $F_0$ (or pressure magnitude $P_0$) to obtain the

corresponding deflection magnitude $|Z(\omega)|$ as Equation 4.2. These deflection magnitudes are successively used in the finite element updating to calibrate layer moduli and modulus gradients. Finally, the complex modulus gradient is obtained by combining calibrated model parameters at different frequencies. Test results used in this section are presented in Figure 4.1, in which Figure 4.1(a) shows time histories of the pressure and deflections recorded by the FWD and Figure 4.1(b) shows deflection magnitudes under pressures with the magnitude 565 kPa at different frequencies.

$$H(\omega) = Z(\omega) / F(\omega) \tag{4.1}$$

$$|Z(\omega)| = F_0 |H(\omega)| \tag{4.2}$$

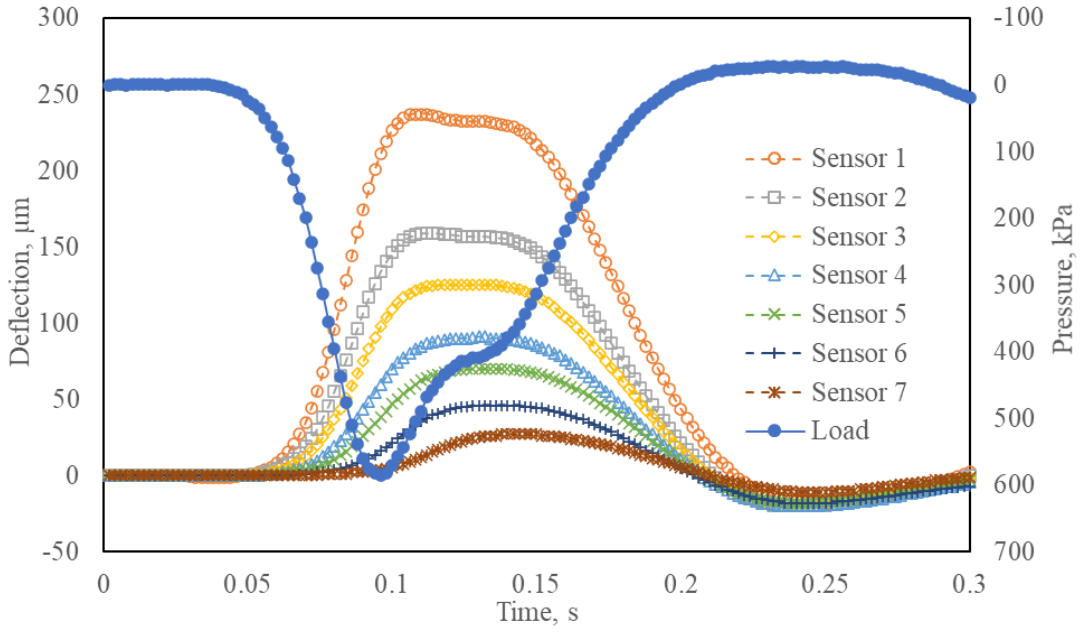


**(a) Time Histories of Pressure and Deflections in an FWD Test**

**Figure 4.1 FWD Test Results before and after Process**

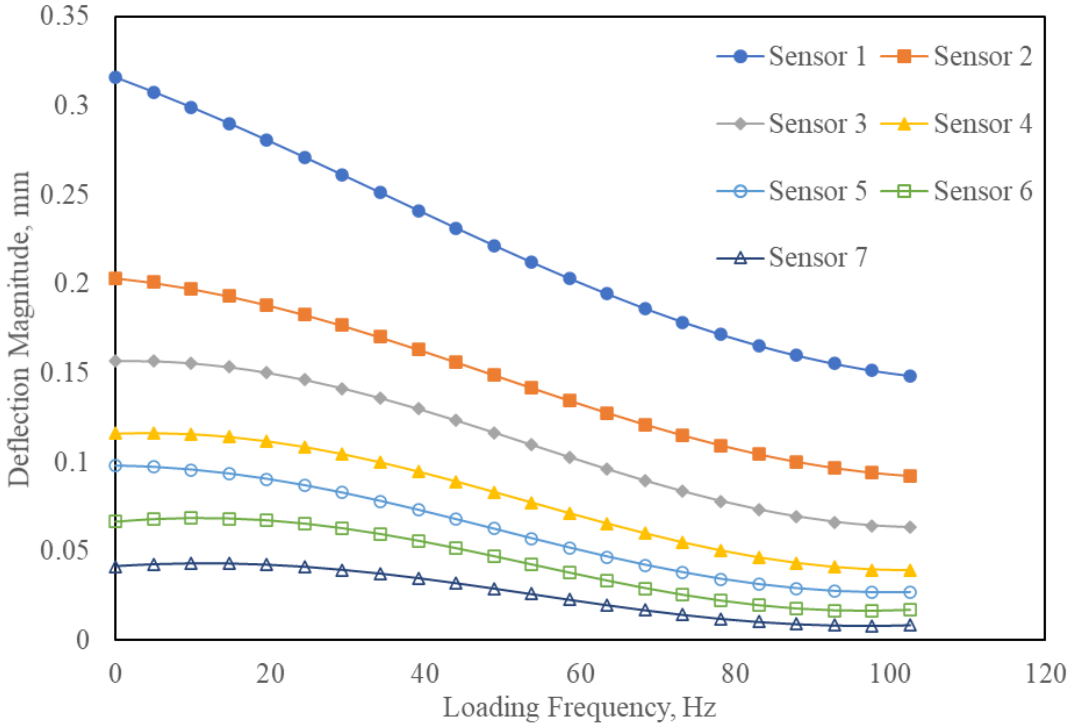


**(b) Deflection Magnitudes at Pressure Magnitude 565 kPa and Different Frequencies**

**Figure 4.1 Continued**

### 4.3 FE Model Updating for Layer Moduli

As FE models in previous sections simualting pavements in FWD tests, a 2D axisymmetric model is built in ABAQUS. Figure 4.2 shows the geometry and material properties of the pavement. According to the sensitivity analysis in which the deflection magnitude at the loading center is used as the indicator, the model radius is 5 m and the total element number is 1300. Results are presented in Table 4.1.

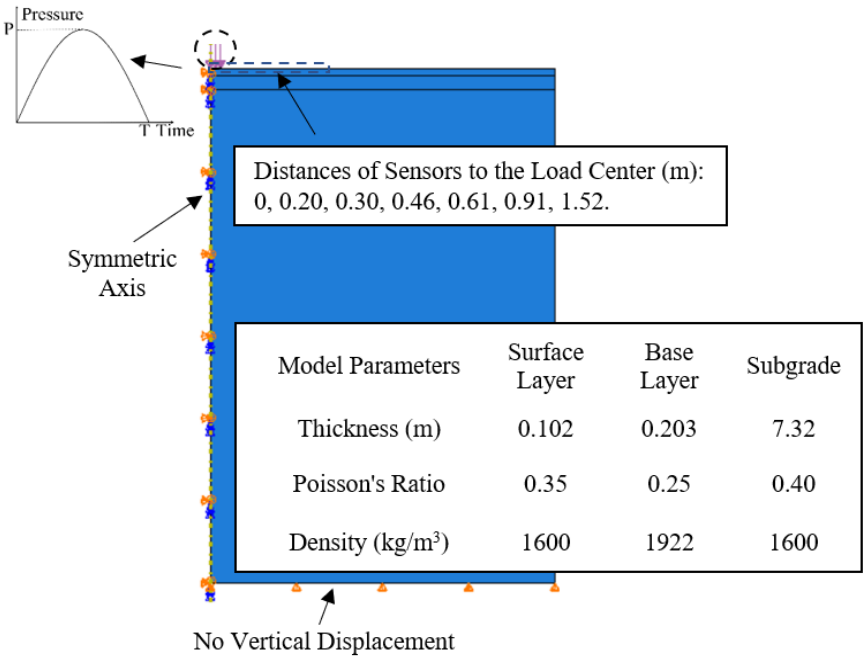


**Figure 4.2 Pavement Structural Parameters and Material Properties**

**Table 4.1 Sensitivity Analysis for Model Radius and Mesh Size**

**(a) Comparison of Different Model Radii**

| R, m | Maximum Deflection at the Loading Center, mm | Relative Error, % |
|---|---|---|
| 3 | 0.227661 | - |
| 4 | 0.238299 | 4.67 |
| 5 | 0.236692 | -0.67 |

**(b) Comparison of Different Mesh Sizes**

| Mesh | Maximum Deflection at the Loading Center, mm | Relative Error, % |
|---|---|---|
| Coarse | 0.206190 | - |
| Fine | 0.233884 | 13.43 |
| Finer | 0.236692 | 1.20 |

The base layer and subgrade are considered as elastic with 5% damping ratio. Since pavement responses at different loading frequencies have been determined separately in Figure 4.1(b), the modulus gradient of the surface layer can be considered as elastic at each specified loading frequency. Following previous studies on the modulus gradient of flexible pavements (Dave et al., 2008; Dave et al., 2010; Luo et al., 2018a), a typical shape of the elastic modulus gradient is used and expressed in Equation 4.3,

$$E(z) = E_b + (E_s - E_b)(\frac{d-z}{d})^n \tag{4.3}$$

where $E(z)$ is the modulus at depth z; $E_b$ and $E_s$ are the modulus at the bottom and top of the layer; $d$ is the thickness of the layer; and $n$ is model parameter controlling the shape of the gradient. This model can represent the shape of the modulus gradient caused by aging. In this section, this model is implemented into ABAQUS using the user-defined material subroutine (UMAT) for the surface layer.

Figure 4.1(b) shows deflection magnitudes at all 7 sensor locations, several of which are selected to obtain model parameters based on a sensitivity analysis conducted in ABAQUS. In the sensitivity analysis, model parameters such as the modulus of the base layer and subgrade, modulus gradient parameters $E_b$, $E_s$ and $n$ are adjusted individually. Corresponding changes in deflection magnitudes are evaluated and shown in Figure 4.3 and Table 4.2. It can be seen from the Figure 4.3 that as the distance to the load center becomes greater, effects of upper layers on deflections decrease. Deflection magnitudes at locations of Sensor 2, Sensor 3 and Sensor 4 nearly stay as the surface

layer modulus gradient changes. Deflection magnitude at Sensor 4 are insensitive to surface layer and base layer moduli. In other words, the deeper the layer is placed, the wider its impact range is on the pavement surface. In this section, deflection magnitudes at Sensor 1, Sensor 2, Sensor 3 and Sensor 4 are used to obtain moduli of three layers for reasons that from the sensitivity analysis, sensors with further distances to the load center have the same use as Sensor 4, which is to calibrate the subgrade modulus. Besides, the noise in the collected data becomes dominant when the deflections are small (Magnuson, 1988).

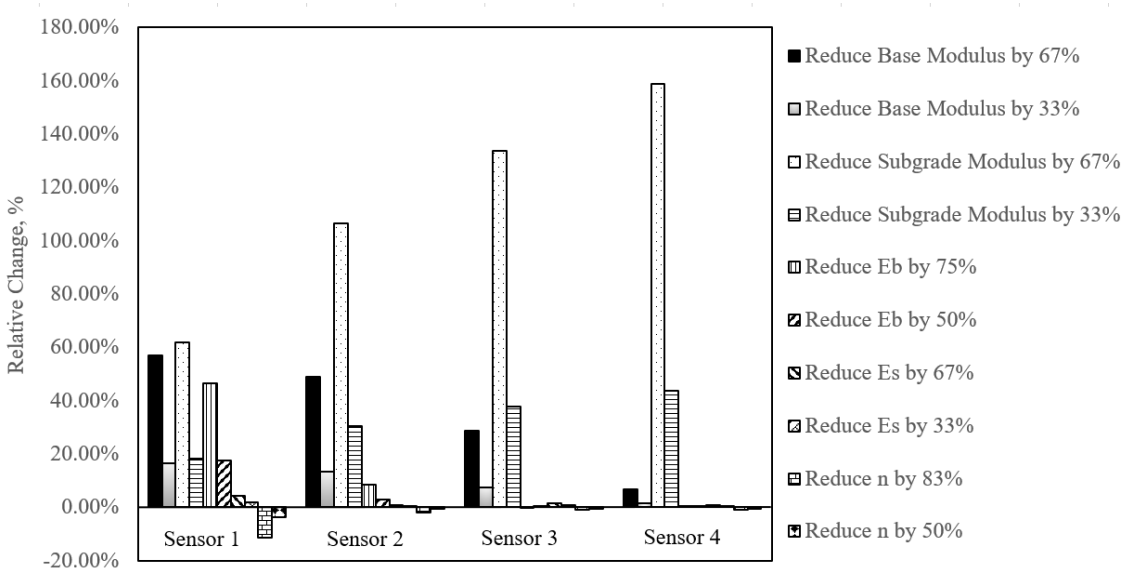


**Figure 4.3 Sensitivity Analysis of Material Property Effects on Deflection at Sensor Locations**

**Table 4.2 Maximum Deflection at the Loading Center with Different Model Moduli**

| Case No. | Material Property | | Deflection Magnitude, mm | | | |
|---|---|---|---|---|---|---|
| | | | Sensor 1 | Sensor 2 | Sensor 3 | Sensor 4 |
| Case 0 | Eb, MPa | 800 | 0.24109 | 0.13172 | 0.09627 | 0.068589 |
| | Es, MPa | 3000 | | | | |
| | n | 6 | | | | |
| | Base Modulus, MPa | 600 | | | | |
| | Subgrade Modulus, MPa | 300 | | | | |
| Case 1 | Base Modulus, MPa | 200 | 0.37851 | 0.19600 | 0.12392 | 0.073148 |
| Case 2 | Base Modulus, MPa | 400 | 0.28068 | 0.14907 | 0.10325 | 0.069643 |
| Case 3 | Subgrade Modulus, MPa | 100 | 0.39033 | 0.27218 | 0.22487 | 0.177453 |
| Case 4 | Subgrade Modulus, MPa | 200 | 0.28497 | 0.17203 | 0.13277 | 0.098495 |
| Case 5 | Eb, MPa | 200 | 0.35349 | 0.14265 | 0.09588 | 0.068733 |
| Case 6 | Eb, MPa | 400 | 0.28344 | 0.13574 | 0.09636 | 0.068783 |
| Case 7 | Es, MPa | 1000 | 0.25143 | 0.13288 | 0.09768 | 0.069234 |
| Case 8 | Es, MPa | 2000 | 0.24526 | 0.13232 | 0.09691 | 0.068896 |
| Case 9 | n | 1 | 0.21376 | 0.12892 | 0.09534 | 0.067833 |
| Case 10 | n | 3 | 0.23221 | 0.13100 | 0.09567 | 0.068199 |

Based on the sensitivity analysis described above, a layer-by-layer calibration method using FE model updating for material properties is proposed. The procedures are described as follows.

Step 1: treat the modulus of subgrade and deflection magnitude at Sensor 4 as 'Model Parameter' and 'Deflection Magnitudes at Sensor Locations' in Figure 4.4. Typical values are selected for the base layer modulus and modulus gradient parameters of the surface layer. In this step, the subgrade modulus is obtained;

Step 2: implement the subgrade modulus obtained from Step 1 into the FE model. Treat the modulus of the base layer and deflection magnitudes at Sensor 2 and Sensor 3

as ‘Model Parameter’ and ‘Deflection Magnitudes at Sensor Locations’ in Figure 4.4. In this step, the base layer modulus is obtained;

Step 3: implement the base layer and subgrade modulus obtained from Step 1 and Step 2 into the FE model. Treat the modulus gradient parameters of the surface layer and deflection magnitude at Sensor 1 as ‘Model Parameter’ and ‘Deflection Magnitudes at Sensor Locations’ in Figure 4.4. In this step, the modulus gradient parameters of the surface layer are obtained.

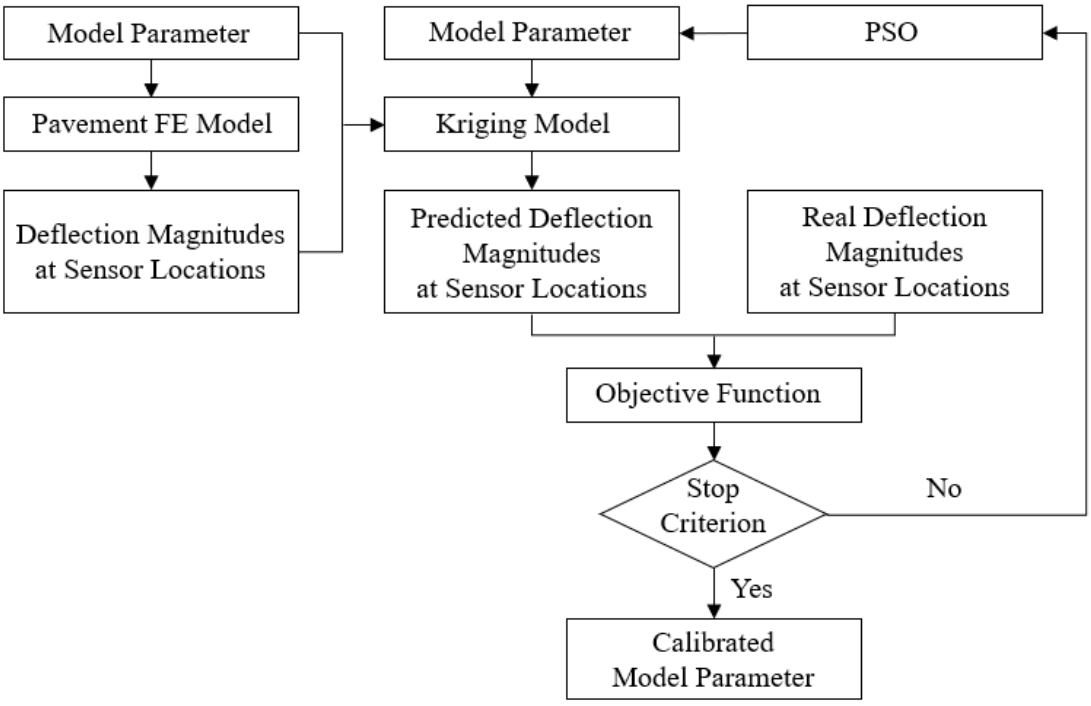


**Figure 4.4 Flow Chart of FE Model Updating for Layer Modulus**

In this FE model updating, 200 FE cases in total are run for the subgrade modulus, in which 150 are used for the kriging model training and 50 are used for the kriging model validation. As shown in Figure 4.5 which is the comparison between

deflection magnitudes at Sensor 4 using subgrade moduli obtained from FE models and predicted by the kriging model at the loading frequency 34.18 Hz, the performance of the kriging model is desirable.

In Figure 4.4, the model parameter keeps updating until the stop criterion is satisfied, which is the total iteration number reaching 100. Figure 4.6 shows the objective function value of the global best particle at each iteration in the search for the subgrade modulus at the loading frequency 34.18 Hz. It can be seen that the objective function value decreases continuously, which proves the successful use of the PSO algorithm in this paper.

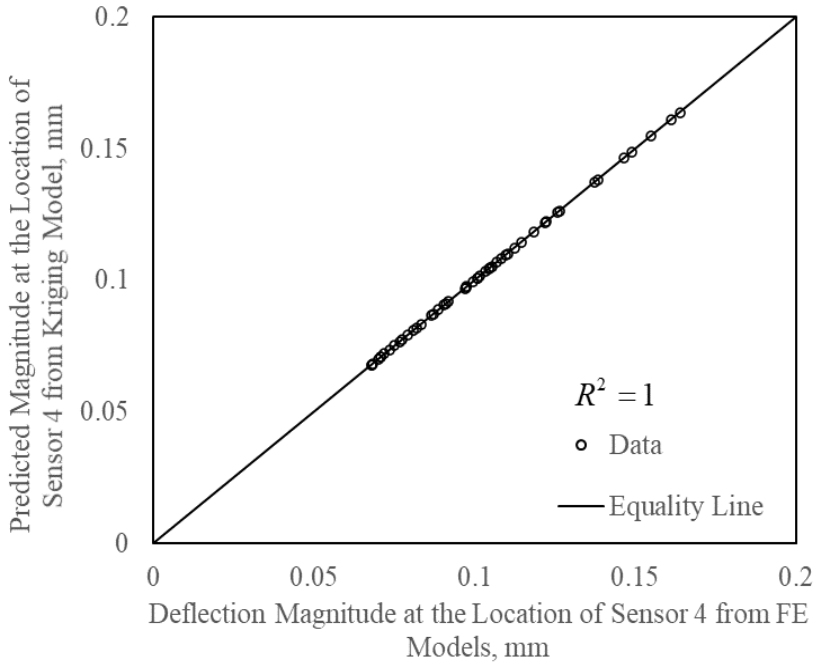


**Figure 4.5 Validation of Kriging Model**

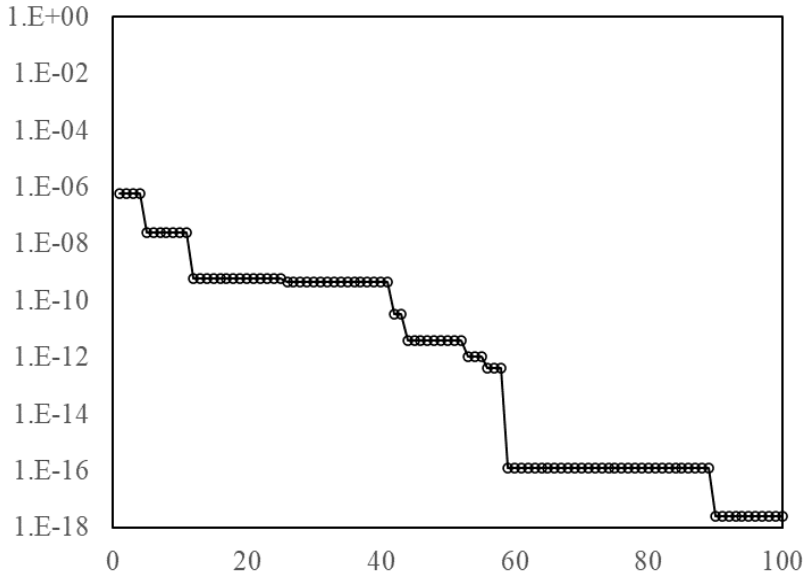


**Figure 4.6 Performance of PSO**

### 4.4 Results and Analysis of Layer Moduli from FE Model Updating

The FE model updating is applied to obtain material properties of the pavement under the loading frequencies 4.88 Hz, 34.18 Hz, 53.71 Hz, 73.24 Hz and 102.54 Hz. Corresponding base layer and subgrade moduli, modulus gradient parameters of the surface layer are combined for their complex expressions. Deflection magnitudes at sensor locations from FE models with calibrated material properties are compared with field data presented in Figure 4.1(b). Such validation is necessary because the construction of the kriging model is based on limited data and objective function values in Figure 4.6 cannot fully represent the relative difference between the field conditions and FE models. Besides, the layer-by-layer calibration scheme is provided based on Figure 4.3, in which upper layers still have very limited effects on deflection magnitudes

at sensor locations far from the load center. Such scheme achieves a targeted and quick calibration, of which the accuracy requires validation.

**Table 4.3 Comparison of Deflection Magnitudes at Sensor Locations Using Material Properties Obtained from Three Methods**

| Loading Frequency, Hz | Field Deflection Magnitude at Sensor Location, mm | | | | Relative Error of Results from BAKFAA, % | | | |
|---|---|---|---|---|---|---|---|---|
| | 1 | 2 | 3 | 4 | 1 | 2 | 3 | 4 |
| 4.88 | 0.31 | 0.20 | 0.16 | 0.12 | | | | |
| 34.18 | 0.25 | 0.17 | 0.14 | 0.10 | -2.78 | 2.33 | 2.76 | 1.49 |
| 53.71 | 0.21 | 0.14 | 0.11 | 0.08 | | | | |
| 73.24 | 0.18 | 0.12 | 0.08 | 0.05 | | | | |
| 102.54 | 0.15 | 0.09 | 0.06 | 0.04 | | | | |
| Loading Frequency, Hz | Relative Error of Results from DBSID, % | | | | Relative Error of Results from FE Model Updating, % | | | |
| | 1 | 2 | 3 | 4 | 1 | 2 | 3 | 4 |
| 4.88 | 27.33 | 8.65 | 6.82 | 5.26 | 0.02 | 1.09 | 1.15 | 1.45 |
| 34.18 | 2.30 | 2.76 | 1.49 | 2.30 | -0.05 | 0.25 | -1.18 | 0.48 |
| 53.71 | 0.31 | 2.80 | 3.27 | 6.06 | -0.01 | -0.72 | -1.74 | 0.82 |
| 73.24 | 1.28 | 8.51 | 15.77 | 26.42 | 0.02 | -1.79 | -1.46 | 2.03 |
| 102.54 | -0.70 | 10.81 | 24.46 | 42.58 | -0.01 | -2.39 | -0.71 | 3.16 |

### *4.4.1 Comparison with BAKFAA*

As a static backcalculation software, BAKFAA requires deflection magnitudes at sensor locations to backcalculate elastic layer moduli. Since no viscoelastic solution is considered in the software, a potential way to obtain the dynamic modulus of the surface layer is running the software multiple times using FFT-processed FWD data in Figure 4.1(b). Table 4.3 shows the comparison between deflection magnitudes measured by the FWD and predicted by FE models with material properties backcalculated from BAKFAA at the loading frequency 34.18 Hz. There is no need to compare results at other frequencies since the accuracy level BAKFAA can achieve is presented in this case.

From Table 4.3, it can also be seen that material properties obtained from FE model updating are more accurate than those from BAKFAA.

Besides, Figure 4.7 shows the comparison of obtained base layer and subgrade moduli at different loading frequencies. Both BAKFAA and FE model updating can capture the sensitivity of the supporting layer moduli to the loading frequency, which is due to moisture accumulated in the layer. However, from BAKFAA, variations of moduli are exaggerated and subgrade modulus can be greater than base modulus, which are unusual. As comparison, the FE model updating used in this section strikes a balance between the accuracy and rationality.

### *4.4.2 Comparison with DBSID*

As a dynamic backcalculation software, DBSID treats the surface layer as viscoelastic and supporting layers as elastic. Equation 4.4 is the expression describing the creep compliance of viscoelastic materials used in DBSID (Ameri et al., 2009),

$$D(t) = D_0 + D_1 t^m \tag{4.4}$$

where $D_0$, $D_1$ and $m$ are model parameters. To apply the backcalculated parameters from DBSID in FE models, the time-domain compliance is transferred to the frequency domain first and then to obtain the dynamic modulus $E^*(\omega)$ as Equation 4.5 – Equation 4.7 (Lytton, 1989),

$$D'(\omega) = D_0 + D_1\Gamma(1+m)\omega^{-m}\cos(m\pi/2) \tag{4.5}$$

$$D''(\omega) = D_1\Gamma(1+m)\omega^{-m}\sin(m\pi/2) \tag{4.6}$$

$$\left|E^*(\omega)\right| = 1/\sqrt{[D'(\omega)]^2 + [D''(\omega)]^2} \tag{4.7}$$

where $\Gamma$ is the gamma function; and $\omega$ is the loading frequency.

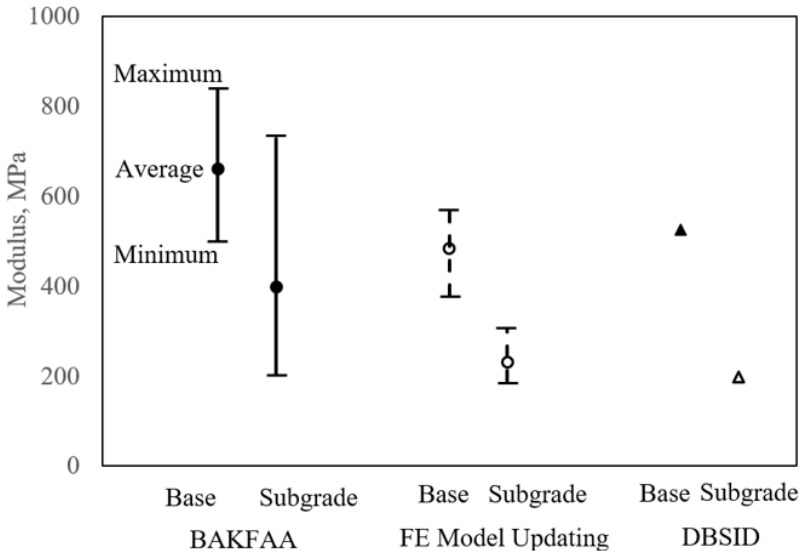


**Figure 4.7 Comparison of Supporting Layer Properties**

As shown in Figure 4.7, moduli of the base layer and subgrade backcalculated from DBSID are close to those from FE model updating. However, constant values from DBSID cannot characterize the modulus variation with the loading frequency in supporting layers. In Table 4.3, relative errors at Sensor 2, Sensor 3 and Sensor 4 from DBSID are much higher than other two methods. Deflection magnitudes at these locations are controlled by supporting layer moduli according to Figure 4.3, which indicates moduli of supporting layers should not be constant at different loading frequencies.

Figure 4.3 also shows that material properties of the surface layer mainly affect deflection magnitudes at Sensor 1. Desirable accuracy at this location indicates a validation for the creep compliance obtained from DBSID. Table 4.4 shows results of FE

models with surface layer properties from DBSID and supporting layer properties from FE model updating. Relative errors significantly decrease at Sensor 2, Sensor 3 and Sensor 4 and remain tolerable at Sensor 1. It indicates the creep compliance is the property DBSID focuses on. Further studies are worthwhile to improve accuracy of DBSID in terms of viscoelastic properties at a wider loading frequency range since results at the frequency 4.88 Hz are not as accurate as other frequencies in Table 4.3.

**Table 4.4 Results of DBSID with Revised Supporting Layer Properties**

| Loading Frequency, Hz | Relative Error of Results from Revised DBSID Method, % | | | |
|---|---|---|---|---|
| | 1 | 2 | 3 | 4 |
| 4.88 | 26.41 | 8.03 | 6.48 | 5.15 |
| 34.18 | 2.52 | 1.63 | -0.77 | -1.26 |
| 53.71 | -0.68 | 0.83 | 0.52 | 2.34 |
| 73.24 | -2.23 | -0.82 | 0.83 | 3.66 |
| 102.54 | -4.96 | -2.29 | 1.67 | 5.15 |

Comparisons with static and dynamic backcalculation softwares BAKFAA and DBSID show that layer moduli calibrated from FE model updating have the optimum match with the field condition. Besides, by using FE model updating, the complex modulus gradient in the AC layer can be obtained, which is the purpose of this section and not considered in other methods. Figure 4.8 shows model parameters of the modulus gradient at different loading frequencies. The modulus at the top and bottom of the surface layer increase with the loading frequency and the shape parameter decreases with the loading frequency, which match the laboratory results in previous researches (Koohi et al., 2012; Ling et al., 2017a; Ling et al., 2017b). Figure 4.9 shows the plot of

the modulus gradient at different loading frequencies. As the loading frequency increases, the gap between the modulus at the top and bottom of the surface layer increases, which was also observed in a previous laboratory test (Ling et al., 2017a).

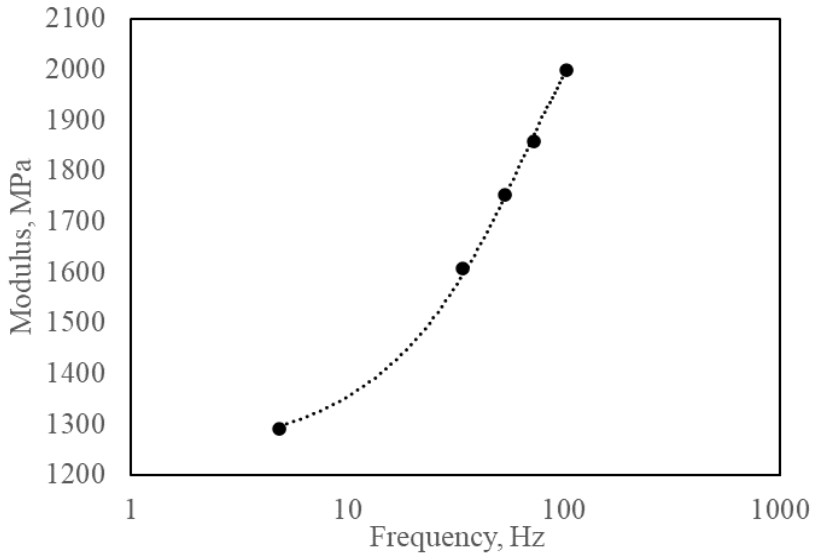


**(a) Modulus at Bottom of Surface Layer**

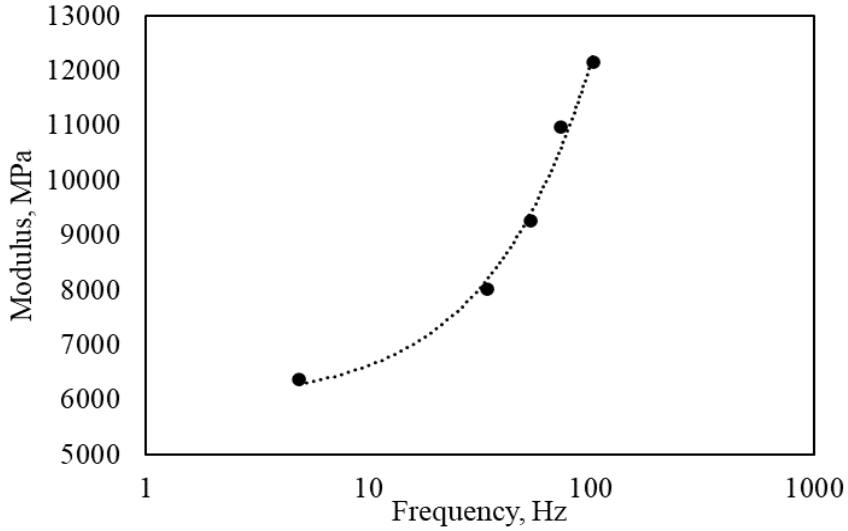


**(b) Modulus at Top of Surface Layer**

**Figure 4.8 Modulus Gradient Model Parameters at Different Loading Frequencies**

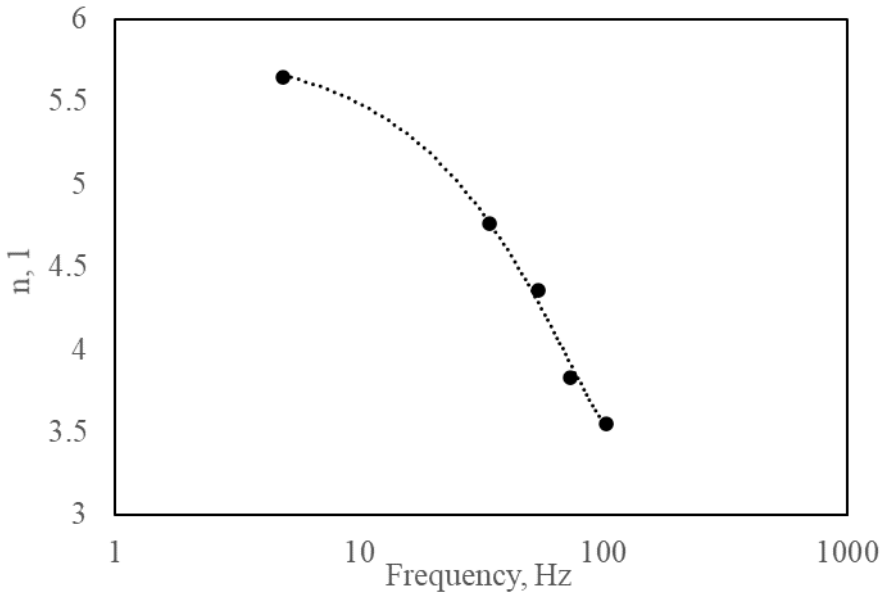


**(c) Modulus Gradient Shape**

**Figure 4.8 Continued**

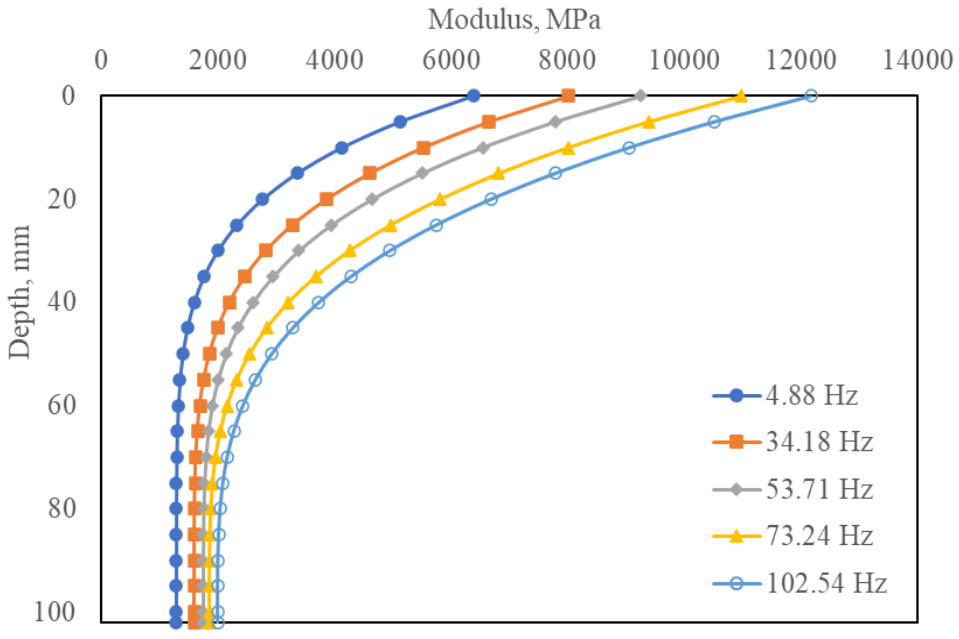


**Figure 4.9 Modulus Gradient with AC Layer Depth at Different Loading Frequencies**

With the proposed method, the aging degree of the flexible pavement can be determined from FWD tests on the same location of the pavement at different service times. Differences between calibrated modulus gradients indicate the aging effects on the pavement. However, an important preconditon should be satisfied that the environmental condition such as the temperature should be similar in different FWD tests. Effects of the temperature can be eliminated by selecting the same date of a year as the testing date. Besides, the location of the pavement should be unaffected by other deteriorations such as the fatigue damage. Because the modulus gradient in the AC layer of flexible pavemnts is sensitive to all factors mentioned above – the temperature, deterioration type, and loading frequency/speed. All these factors and their effects are clarified in the next section.

# 5. DETERMINATION OF FLEXIBLE PAVEMENT DETERIORATION CONDITIONS USING LTPP DATABASE

## 5.1 Introduction

From previous sections, some essential points in evaluation of flexible pavements have been clarified. First, evaluating pavement condition is a significant process for the pavement design, maintenance and rehabilitation. Second, a comprehensive evaluation and a timely advanced warning can effectively avoid impending costly levels of future distresses. Third, in flexible pavements, the deterioration is a gradual process synthetically caused by the environment and traffic. Forth, two typical distresses aging and fatigue damage have different causes and effects on flexible pavements.

As introduced in Section 1, modulus or modulus-associated factors are among the mostly applied indicators of pavement conditions. As a direct indicator of the material strength, modulus occurs in many mechanistic-empirical (ME) models to predict the total number of load repetitions the pavement can bear (ARA-ERES, 2004; Sadeghi and Fathali, 2007). Deflection, directly controlled by the modulus, is used in indexes to determine the pavement condition such the structural number (SN) (Martin, 2011; Crook et al., 2012), the structural condition index (SCI) (Elbagalati et al., 2016), the structural index of a pavement (SIP) (Zhang et al., 2003) and the deflection slope index (DSI) (Nasimifar et al, 2016). The development of the FWD, the RWD and the TSD contributes to the obtain and applications of these indexes. Pavement responses at critical locations, which consider both the mechanism of distresses and the material

strength, are used in ME models for individual distress modes (ARA-ERES, 2004). The tensile strain at the surface of the asphaltic layer, for example, is for the top-down cracking while the tensile strain at the bottom of the asphaltic layer is for the bottom-up cracking.

Different from rigid pavements, the modulus of surface materials of flexible pavements is greatly affected by the temperature and loading frequency. Their relationships have been studied comprehensively in laboratory tests (Bonaquist, 2008) and considered increasingly in field pavements (Nazarian and Alvarado, 2006; Ulloa et al., 2013). Compared with the loading frequency, effects of the temperature are easier to be implemented into models since the temperature changing with time and pavement depth has been characterized thoroughly (Han et al., 2011). The temperature is considered either in the modulus prediction and calibration (Ling et al., 2019a) or explicitly as a parameter in the ME models (Luo et al, 2019; Ling et al., 2019b). The traffic loads in these models are characterized in terms of the axle number and axle weight. It is practical and understandable since the speed variation is marginal compared with the load magnitude, especially with the speed limit in highways. However, for those structural indexes obtained from NDT devices and used for the pavement monitoring, effects of the temperature and loading frequency should be considered and eliminated for better comparison and evaluation.

The main purpose of this section is to provide a methodology in determining the deterioration condition of flexible pavements from the modulus considering effects of

- temperature gradient in the asphalt layer;

- loading frequency spectrum in the asphalt layer; and
- variation of material properties in laboratory and in-situ tests.

Taking advantages of rich and timely information stored in the Long-Term Pavement Performance (LTPP) database, study in this section is based on real pavement structures and their environmental conditions in the US. Pavement structure and construction, layer properties, climatic conditions and pavement performance can be obtained and used to determine the deterioration degree of flexible pavements over time. FE simulations of NDT and FE model updating with AI algorithms and kriging models are applied as well.

## 5.2 Pavement Information in the LTPP Database

Similar to Section 4, the basic ideas of this section are simulating responses of flexible pavements in NDT tests and calibrating model parameters based on the comparison between simulated and measured responses. Two pavement sections in Texas are selected in this study. Available information in the LTPP database to build FE models are listed in Table 5.1. Figure 5.1 shows structural configurations and properties of supporting layers except the modulus. According to the record, such layer settings are maintained until the first reconstruction occurred.

**Table 5.1 Summary of Information Retrieved from the LTPP Database**

| Type | Location | Information |
|---|---|---|
| Structure | Pavement Structure and Construction – Pavement Layer Type and Thickness – Representative Pavement Structure | Layer type; Layer thickness; Layer order; Construction type |
| Material | Pavement Structure and Construction – Material - Layer Properties and Field Sampling – AC Mixture Properties (Calculated ESTAR) – Calculated ESTAR Modulus | Dynamic modulus of AC mixtures with original binders at different loading frequencies and temperatures |
| Climate | Performance – Backcalculation and Deflection – Deflection – Temperature Data | Temperatures within the AC layer on the dates/times of field testing |
| NDT Results | Performance – Backcalculation and Deflection – Deflection – Deflection Raw Data | Load (pressure) magnitudes of the FWD; Deflection peaks at sensor locations |

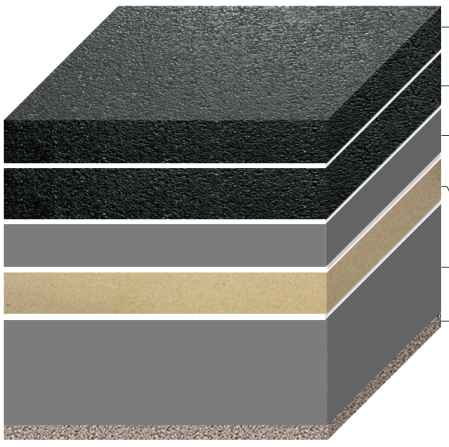

| Layer No. | Type | Thickness, mm | Density, kg/m³ | Poisson's Ratio | Damping Ratio, % |
|---|---|---|---|---|---|
| 1 | Asphalt Concrete | 55.9 | 2243 | 0.35 | |
| 2 | Asphalt Concrete | 134.6 | 2243 | 0.35 | |
| 3 | Bound Base | 101.6 | 2195 | 0.35 | 5 |
| 4 | Unbound Base | 88.9 | 1922 | 0.35 | 5 |
| 5 | Bound Subbase | 304.8 | 1922 | 0.4 | 5 |
| 6 | Subgrade | Infinite | 1922 | 0.4 | 5 |

**(a) Section 48-0117**

**Figure 5.1 Pavement Structural Parameters and Material Properties**

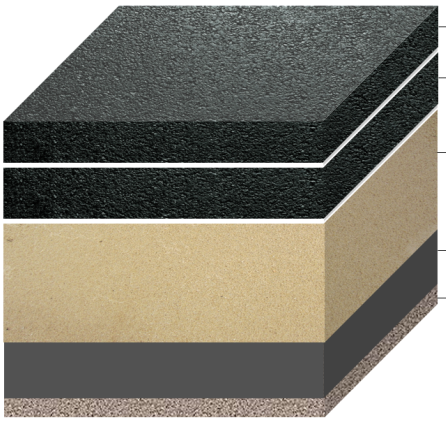

| Layer No. | Type | Thickness, mm | Density, kg/m³ | Poisson's Ratio | Damping Ratio, % |
|---|---|---|---|---|---|
| 1 | Asphalt Concrete | 61.0 | 2243 | 0.35 | |
| 2 | Asphalt Concrete | 66.0 | 2243 | 0.35 | |
| 3 | Unbound Base | 330.2 | 1922 | 0.35 | 5 |
| 4 | Bound Subbase | 304.8 | 1922 | 0.4 | 5 |
| 5 | Subgrade | Infinite | 1922 | 0.4 | 5 |

**(b) Section 48-0167**

**Figure 5.1 Continued**

The dynamic modulus of AC mixtures with original binders is assumed as undamaged and reference modulus in this study. In the LTPP database, the dynamic modulus predicted at the loading frequencies 0.1 Hz, 0.5 Hz, 1 Hz, 5 Hz, 10 Hz, 25 Hz and temperatures -10 °*C* , 4.4 °*C* , 21.1 °*C* , 37.8 °*C* , 54.4 °*C* are provided. As for the modulus at an arbitrary loading frequency and temperature, the master curve shown in Equation 5.1 is constructed following procedures presented in a previous research (Zhang et al., 2016),

$$\log(\left|E^*(f_r)\right|) = \delta + \frac{\alpha}{1+e^{\eta-\gamma\log(f_r)}} \tag{5.1}$$

in which,

$$f_r = a_T f \tag{5.2}$$

$$\log(a_T) = aT^2 + bT + c \tag{5.3}$$

where $E^*(f_r)$ is the dynamic modulus at the reduced frequency $f_r$ in Hz; $f$ is the loading frequency in Hz; $T$ is the temperature in kelvin; $a_T$ is the time-temperature shift factor; and $\delta$, $\alpha$, $\eta$, $\gamma$, $a$, $b$, $c$ are fitting parameters.

According to the record in Figure 5.1, two AC layers are constructed separately in each pavement. Figure 5.2 shows master curves of two layers at the reference temperature using Equations 5.1 – 5.3. It can be seen that two layers are made of identical materials in both pavements. Therefore, two AC layers are combined in the corresponding FE models for simplicity.

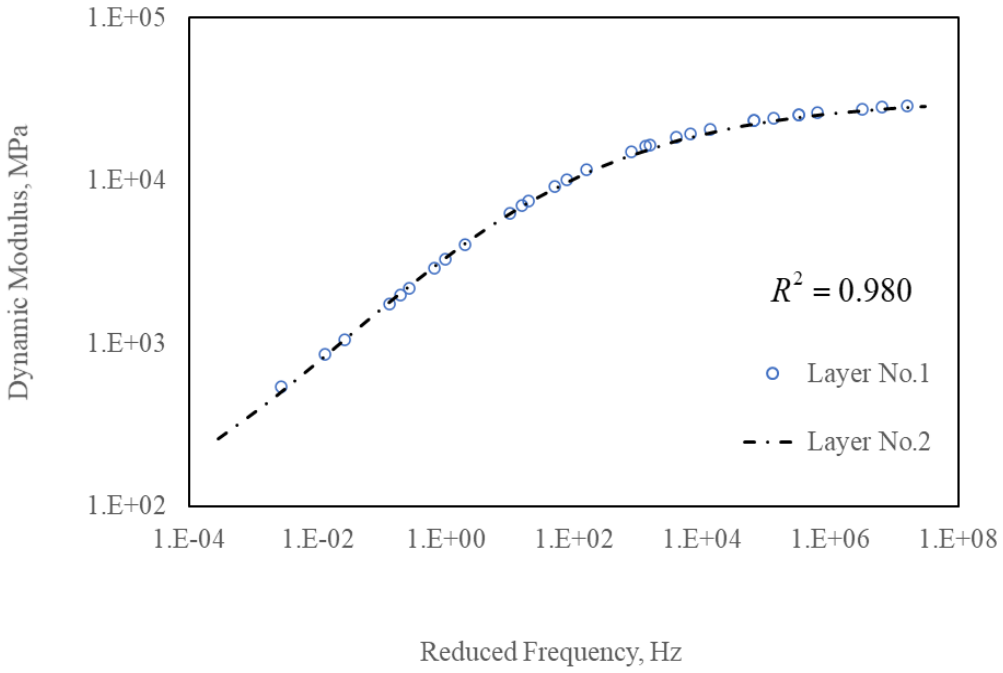


**(a) Section 48-0117**

**Figure 5.2 Comparison of Master Curves of Two Layers at the Reference Temperature**

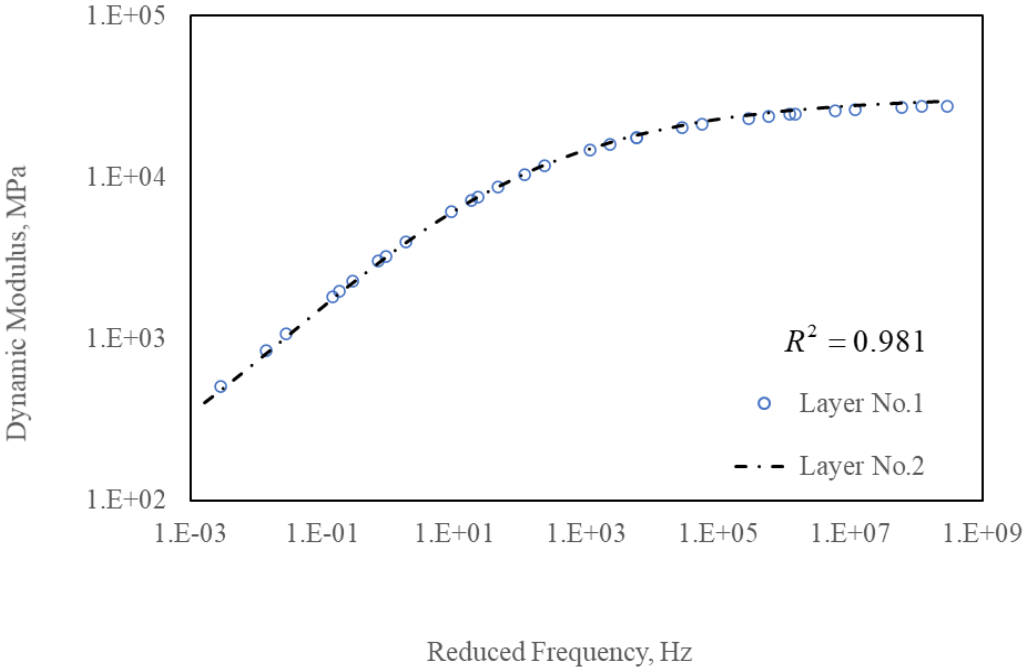


**(b) Section 48-0167**

**Figure 5.2 Continued**

Table 5.2 shows an example of climatic data and FWD test results for two pavement sections from the LTPP database and supplementary materials (Schmalzer, 2006). In the field, FWD tests are conducted at different locations of the pavement surface. Moreover, FWD tests with different pressure magnitudes are conducted at each testing location, which is achieved by adjusting the drop height of the loading plate. In the transverse direction, the location "Flexible pavement outer wheel path" is selected to fully consider the fatigue damage induced by traffic loads. In the longitudinal direction, random points are selected for two pavement sections, of which the "POINT_LOC" (point location) are 0 and 137.2 for the section 48-0117 and 48-0167, respectively. Among three different pressure magnitudes, the Level 2 with the nominal pressure

magnitude 570 kPa is selected. The main reason is that the drop height of the loading plate affects the pressure magnitude as well as the loading duration, in another word, the loading frequency (Sebaaly et al., 1986). Without any explicit records, it is reasonable to select 0.03 s as the loading duration for pressure magnitudes of Level 2, which is generally acknowledged and applied in most studies (Wang and Li, 2016).

**Table 5.2 Climate and NDT Results Retrieved from the LTPP Database**

| Section | Testing Date | Layer Depth, mm | Temperature, degree C | Pressure Magnitude of the FWD, kPa |
|---|---|---|---|---|
| 48-0117 | 1999/8/18 | 25.4 | 57.2 | 574 |
| | | 190.5 | 45.6 | |
| | 2000/5/9 | 25.4 | 30.0 | 548 |
| | | 190.5 | 32.0 | |
| | 2002/2/12 | 25.4 | 27.4 | 598 |
| | | 188.0 | 21.0 | |
| 48-0167 | 1999/8/19 | 25.4 | 54.4 | 567 |
| | | 63.5 | 51.9 | |
| | 2000/5/9 | 25.4 | 46.8 | 532 |
| | | 63.5 | 42.4 | |
| | 2002/2/13 | 25.4 | 21.8 | 583 |
| | | 63.5 | 21.1 | |

**Table 5.2 Continued**

| Section | Sensor Distance to the Loading Center (Line 1) (mm) and Deflection Peak (Line 2) (mm) | | | | | | | |
|---|---|---|---|---|---|---|---|---|
| Sensor No. | 1 | 2 | 3 | 4 | 5 | 6 | 7 | 8 |
| 48-0117 | 0 | 203 | 305 | 457 | 610 | 914 | 1524 | |
| | 0.194 | 0.109 | 0.076 | 0.058 | 0.049 | 0.036 | 0.023 | |
| | 0 | 203 | 305 | 457 | 610 | 914 | 1219 | 1524 |
| | 0.105 | 0.072 | 0.058 | 0.047 | 0.040 | 0.030 | 0.025 | 0.020 |
| | 0 | 203 | 305 | 457 | 610 | 914 | 1219 | 1524 |
| | 0.091 | 0.070 | 0.062 | 0.054 | 0.047 | 0.036 | 0.029 | 0.023 |
| 48-0167 | 0 | 203 | 305 | 457 | 610 | 914 | 1524 | |
| | 0.305 | 0.177 | 0.124 | 0.082 | 0.058 | 0.037 | 0.022 | |
| | 0 | 203 | 305 | 457 | 610 | 914 | 1219 | 1524 |
| | 0.239 | 0.149 | 0.113 | 0.078 | 0.056 | 0.036 | 0.028 | 0.022 |
| | 0 | 203 | 305 | 457 | 610 | 914 | 1219 | 1524 |
| | 0.223 | 0.182 | 0.151 | 0.112 | 0.081 | 0.048 | 0.031 | 0.023 |

In this section, the FE model updating is used in determinations of the equivalent frequency spectrum of the FWD load in the AC layer and moduli of pavement layers. Figure 5.3 shows basic procedures of the FE model updating used in this section. Details of the kriging model and PSO algorithm have been introduced in previous sections.

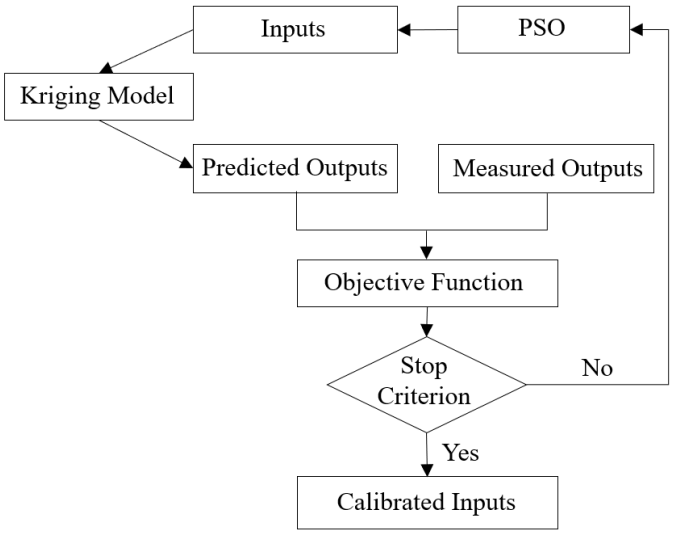


**Figure 5.3 Flow Chart of the FE Model Updating**

2D axisymmetric models are selected to simulate pavements in FWD tests as in previous sections, of which the basic parameters are listed in Figure 3.1 and Table 3.2. Also, sensitivity analysis is required to determine the model radius, mesh size, depth of subgrade, etc. Figure 5.4 shows the 2D axisymmetric FE model of Section 48-0167 built in ABAQUS and results of the sensitivity analysis to determine the subgrade depth. In the sensitivity analysis, the pressure magnitude is 565 kPa and layer moduli are averaged backcalculation moduli recorded in the LTPP database. The vertical deflection at the loading center is selected as the model output. The model outputs are compared in the models with different subgrade depths and element types, in which the infinite element is applied as well at boundaries to reduce the element number without losing significant accuracy (Wang and Li, 2016). It can be seen from Figure 5.4(b) that variations of results caused by the subgrade depth decrease as the subgrade depth increases. The differences between the linear element, quadratic element and infinite element dropped below 0.5 % when the subgrade depth is 7238 mm. Finally, the model radius, subgrade depth and element number are 5.0 m, 7238 mm and 4200 for Section 48-0167. Such numbers are 5.0 m, 7315.2 mm and 5760 for Section 48-0117.

As described above, one goal of the FE model updating is to calibrate layer moduli based on measured pavement responses in FWD tests, which are the deflection peaks at sensor locations in Table 5.2. A two-step calibration process is proposed as Section 4 based on different sensitivities of surface vertical deflections to layer moduli according to their distances to the loading center. Figure 5.5 shows the results of a similar sensitivity analysis for Section 48-0117. In each case the modulus of one layer is

adjusted and the surface vertical deflection at each sensor location is recorded and compared with the original case. It can be seen that as the distance to the loading center becomes greater, the surface vertical deflection is more affected by lower layers. The extreme cases are that the vertical deflection at the loading center is sensitive to all layer moduli and the vertical deflection at Sensor 8 depends merely on the subgrade modulus. Accordingly, vertical deflections at Sensor 4 – Sensor 8 are used to calibrate moduli of supporting layers first. Vertical deflections at Sensor 1 – Sensor 3 along with the calibrated supporting layer moduli are used to calibrate the modulus gradient of the AC layer then.

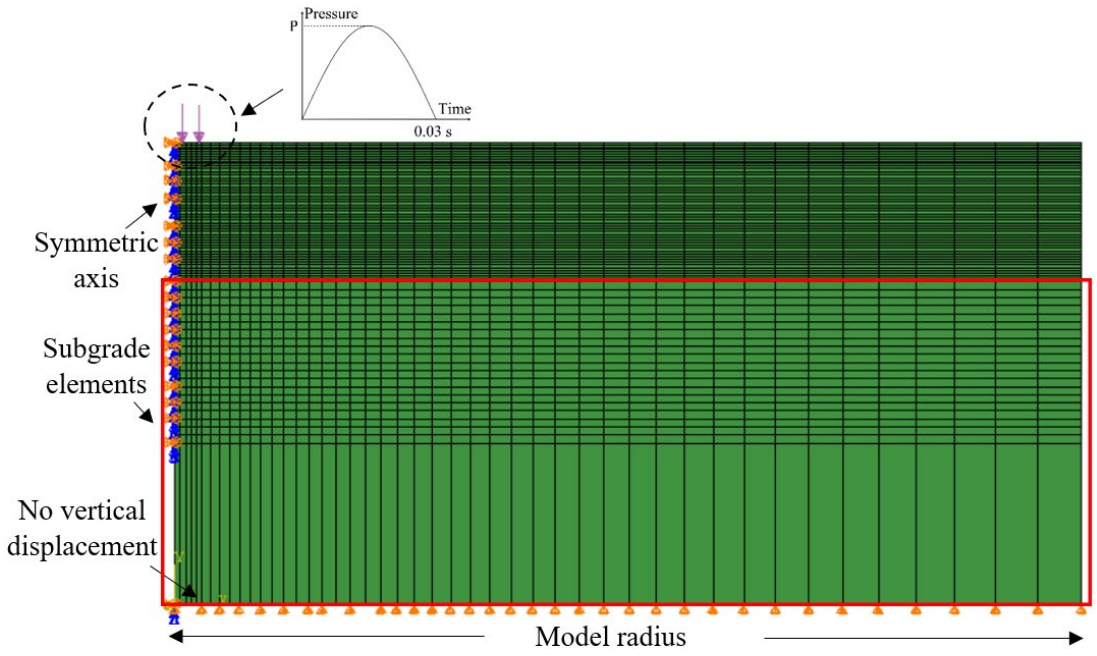


**(a) 2D Axisymmetric Model**

**Figure 5.4 2D Axisymmetric FE Model of Section 48-0167**

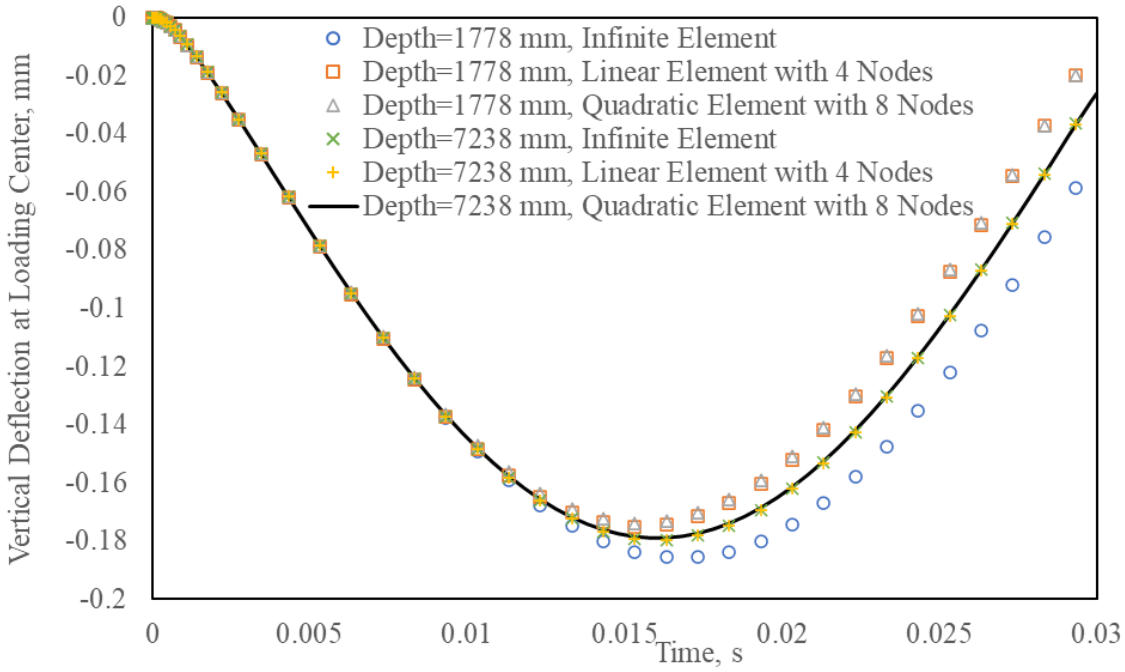


**(b) Sensitivity Analysis for Subgrade Depth**

**Figure 5.4 Continued**

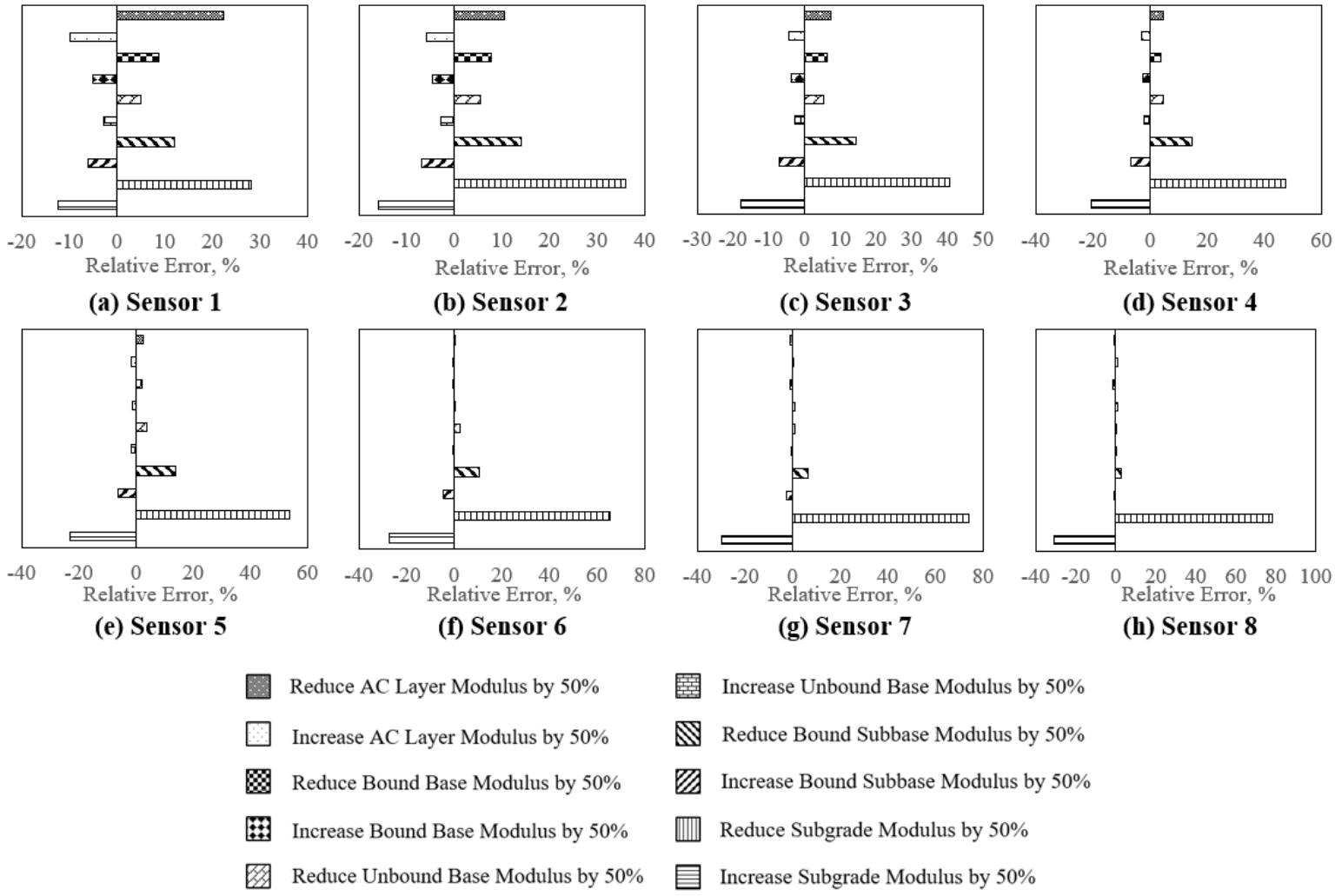


**Figure 5.5 Sensitivity Analysis of Layer Moduli on Surface Deflections in Section 48-0117**

## 5.3 FE Model Updating for Equivalent Frequency Spectrum and Layer Moduli

A step-by-step procedure for the FE model updating in this study is presented as follows.

1) Obtain the equivalent frequency spectrum of the FWD load in the AC layer.
   a) use the built FE model, in which the supporting layers are elastic and the AC layer is viscoelastic as Equation 5.1. Apply the FWD load with the duration 0.03 s and extract vertical deflections under the loading center along the AC layer, which are the "Measured Outputs" in Figure 5.3;
   b) change the material model of the AC layer from Equation 5.1 to Equation 4.3, which is elastic but can characterize the modulus variation with depth. The model coefficients $E_b$, $E_s$ and $n$ are "Inputs" in Figure 5.3;
   c) train the kriging model with sampled inputs and corresponding outputs obtained from the FE model in Step 1.b. With trained kriging model and "Measured Outputs", find the "Calibrated Inputs" via PSO algorithm;
   d) from the "Calibrated Inputs" and master curve expressed in Equation 5.1, calculate the corresponding frequencies along the AC layer, which form the equivalent frequency spectrum of the FWD load for this pavement section.
2) Obtain the moduli of supporting layers.
   a) use the built FE model, in which the modulus of the AC layer is calculated from Equation 5.1 with temperatures in Table 5.2 and frequencies from Step 1. Apply the FWD load with the duration 0.03 s and pressure magnitude in Table 5.2;

b) treat supporting layer moduli as inputs and vertical deflections at Sensor 4 – Sensor 8 as outputs. Train the kriging model with sampled inputs and corresponding outputs from FE models in Step 2.a;

c) calibrate supporting layer moduli with trained kriging model and "Measure Outputs" in Table 5.2.

3) Obtain the modulus of the deteriorated AC layer.

a) use the built FE model, in which moduli of supporting layers are obtained from Step 2 and the modulus model of the AC layer is Equation 4.3. Apply the FWD load with the duration 0.03 s and pressure magnitude in Table 5.2;

b) treat model coefficients $E_b$, $E_s$ and $n$ as inputs and vertical deflections at Sensor 1 – Sensor 3 as outputs. Train the kriging model with sampled inputs and corresponding outputs from FE models in Step 3.a;

c) calibrate model coefficients of the AC layer modulus with trained kriging model and "Measure Outputs" in Table 5.2.

The deterioration degree of the pavement is determined from the comparison between moduli of the AC layer obtained from Step 1 and Step 3, which come from undamaged and damaged pavements. Results and analysis of the method are presented in the next section.

## 5.4 Results and Analysis of the FE Model Updating

In this section, results obtained from the previous section such as the equivalent frequency spectrum of the FWD load and layer moduli are presented and validated. The average deterioration degree of the pavement is introduced and discussed.

### *5.4.1 Equivalent Frequency Spectrum of the FWD Load*

The equivalent frequency spectrum in the AC layer is proposed for the sensitivity of asphalt mixtures to the loading frequency (Zhang et al., 2016) and nonuniform predominant frequencies observed in a previous research (Ulloa et al., 2013). The vertical deflection is selected as the indicator for the equivalency since it is used for the modulus calibration in this study.

Figure 5.6 shows obtained frequency spectrums at 25 $°C$ in two sections. Obvious gradients can be observed with the depth in both sections and the descending trend is similar with the previous research (Ulloa et al., 2013). Specifically, the gradient varies with the pavement structure and equivalent frequencies in Section 48-0117 are significantly different from the commonly used value 10 Hz. A more straightforward comparison is conducted and presented in Figure 5.7, in which obtained frequency spectrums, 10 Hz and 33 Hz ($1/T$) are used and vertical deflections are compared. It can be seen that cases with equivalent frequency spectrums have the optimal accuracy. Moreover, it indicates any constant value cannot replace loading frequencies of the FWD load in the AC layer, at least in terms of the vertical deflection.

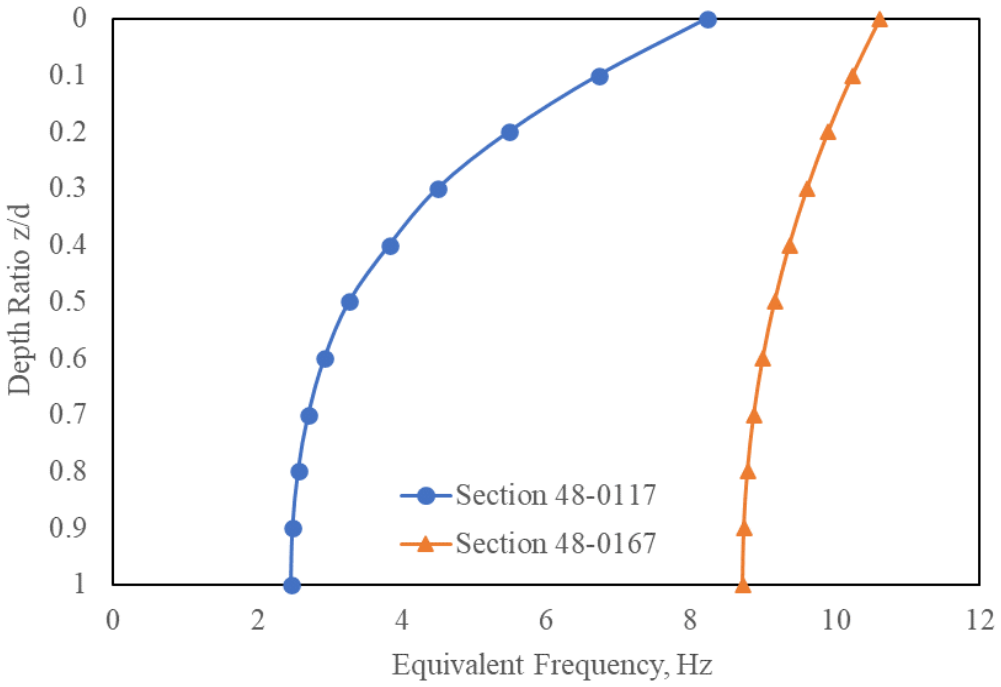


**Figure 5.6 Equivalent Frequency Spectrum of the FWD Load at 25 Degree C**

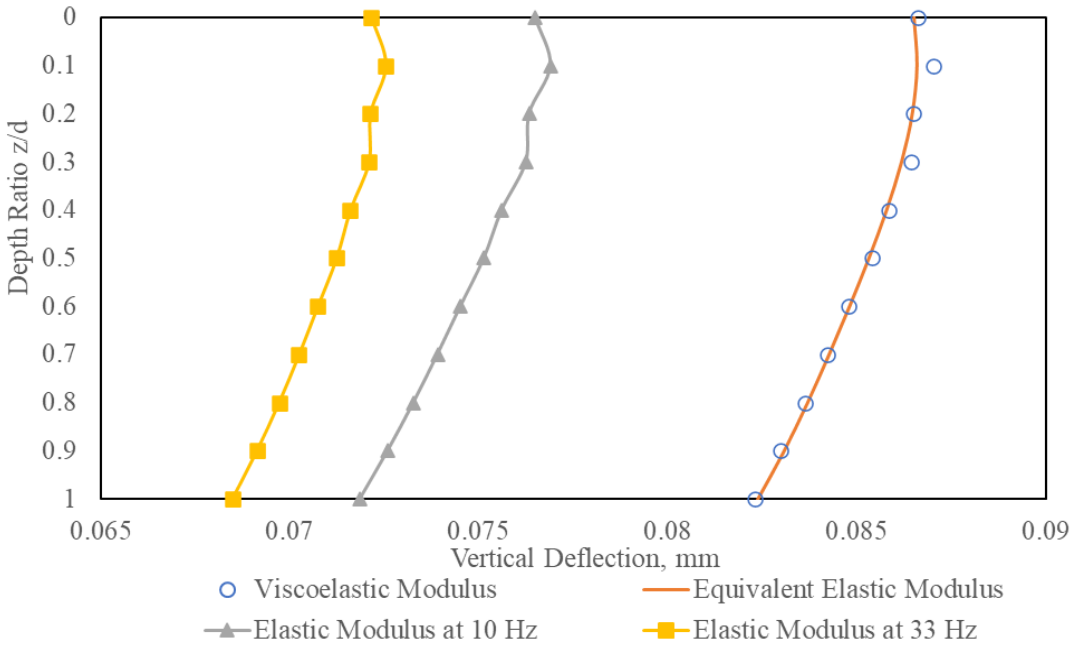


**(a) Section 48-0117**

**Figure 5.7 Comparison of the Frequency Spectrum with Constant Frequencies**

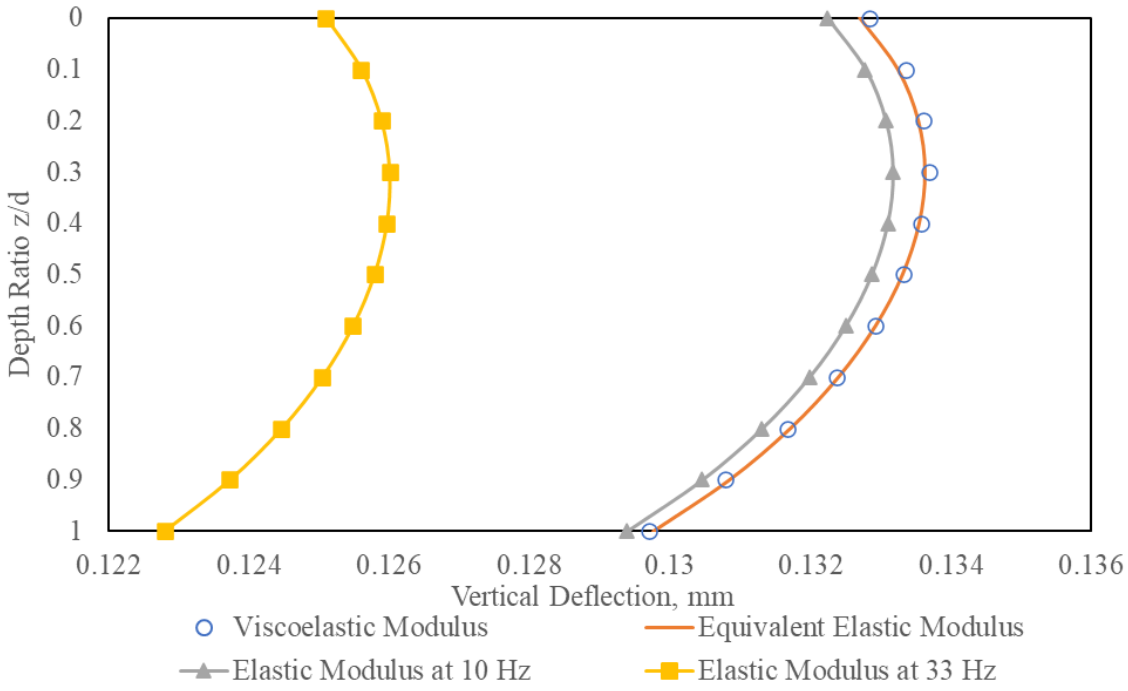


**(b) Section 48-0167**

**Figure 5.7 Continued**

Furthermore, equivalent frequency spectrums obtained at 25 $°C$ are applied in different temperatures. Temperatures 40 $°C$ , 60 $°C$ with frequencies in Figure 5.6 are substituted into Equation 5.1 and vertical deflections are compared with cases using viscoelastic moduli at corresponding temperatures. Two conclusions can be drawn from Figure 5.8 that the equivalent frequency spectrum for a certain load is independent of the temperature; it is reasonable and practical to apply the equivalent frequency spectrum obtained at one temperature to any other temperature or temperature gradient, which is exactly the method in this section.

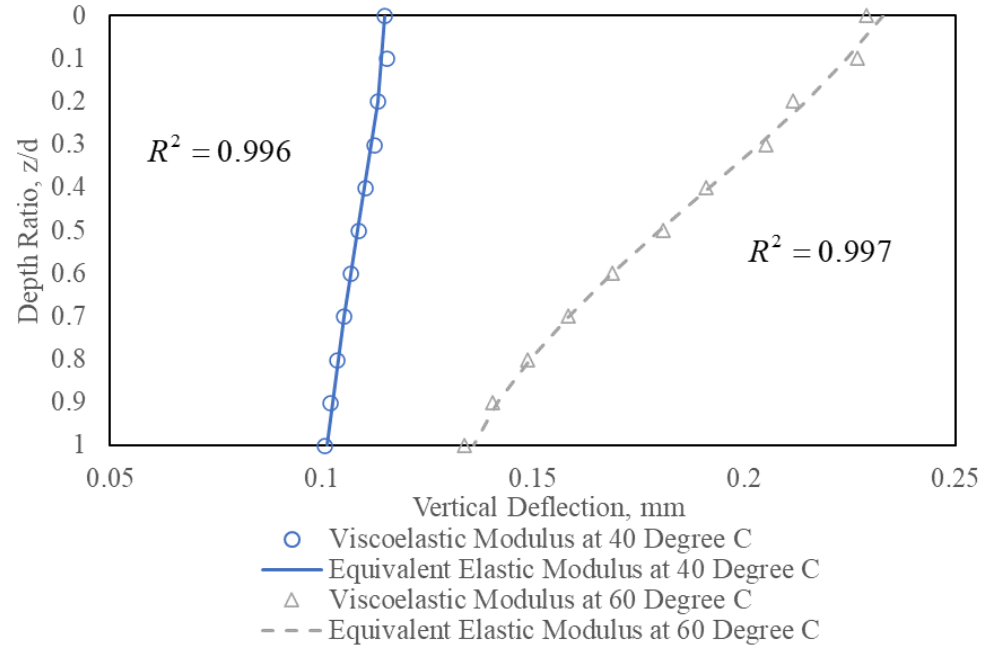


**(a) Section 48-0117**

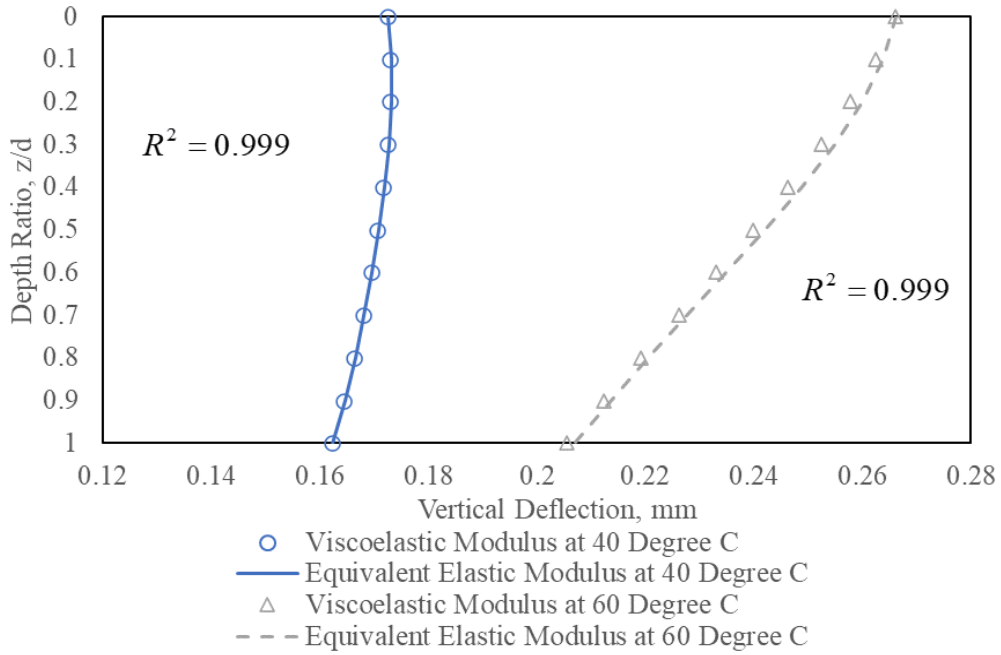


**(b) Section 48-0167**

**Figure 5.8 Application of the Frequency Spectrum in Different Temperatures**

### *5.4.2 Modulus Gradient of the AC Layer*

Since values of supporting layer moduli are out of interest in this section, main contents of this section are validations of the FE model updating and two-step calibration method.

Desirable performance of the kriging model and PSO algorithm can be seen from Figure 5.9(a) and Figure 5.9(c). Measured vertical deflections at Sensor 4 – Sensor 8 are compared with those predicted by the FE models, in which supporting layer moduli are calibrated by the FE model updating. Comparisons of Figure 5.9(a) with Figure 5.9(b) and Figure 5.9(c) with Figure 5.9(d) validate the two-step method. The only difference between FE models in Step 2 and Step 3 is the modulus of the AC layer. Adjustments in the AC layer do not affect deflections at Sensor 4 – Sensor 8 much as indicated in Figure 5.9.

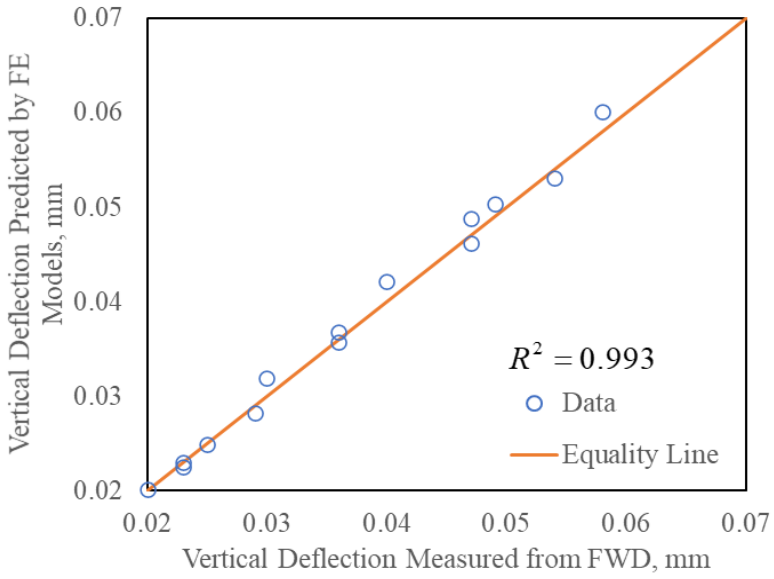


**(a) Section 48-0117 in Step 2**

**Figure 5.9 Validation of Supporting Layer Moduli from the FE Model Updating**

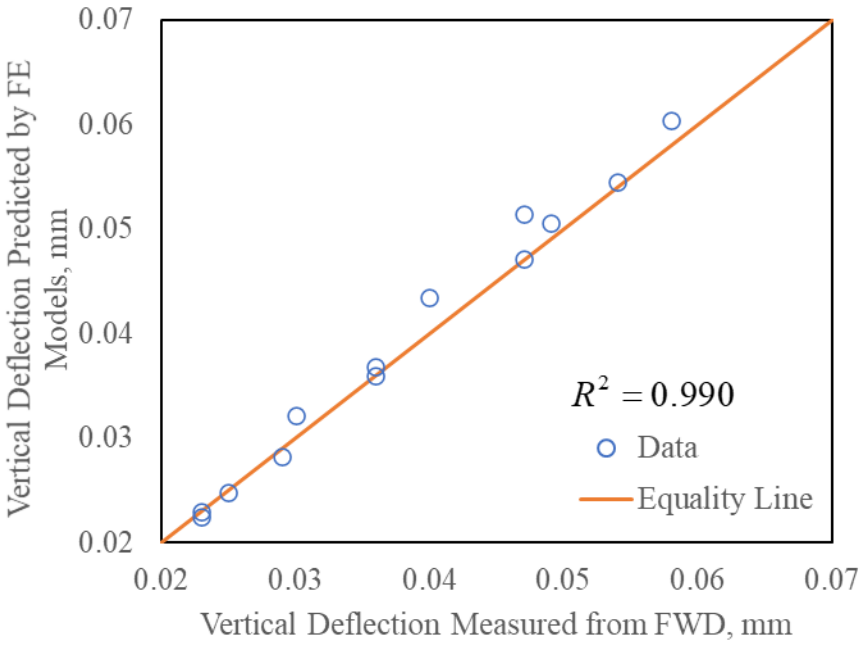


**(b) Section 48-0117 in Step 3**

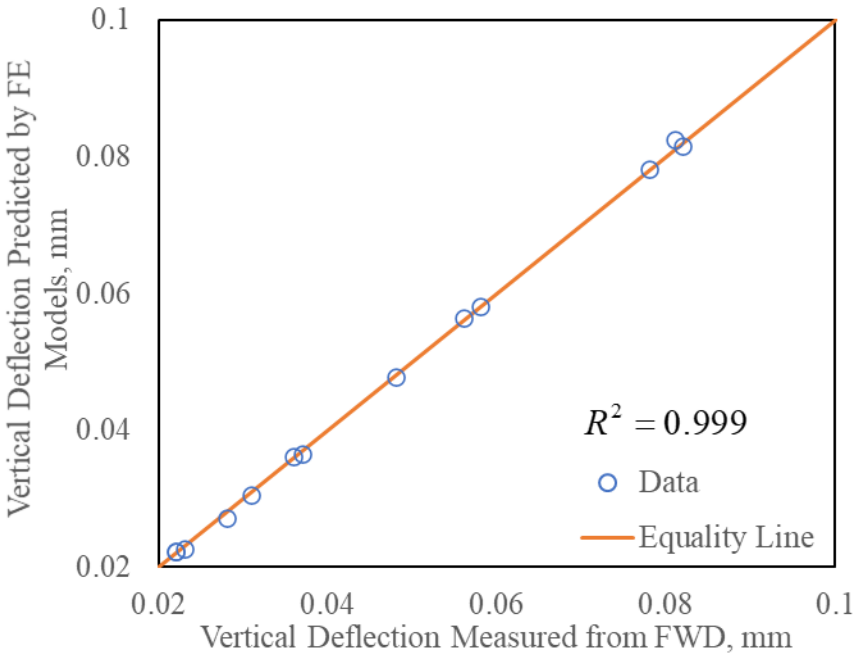


**(c) Section 48-0167 in Step 2**

**Figure 5.9 Continued**

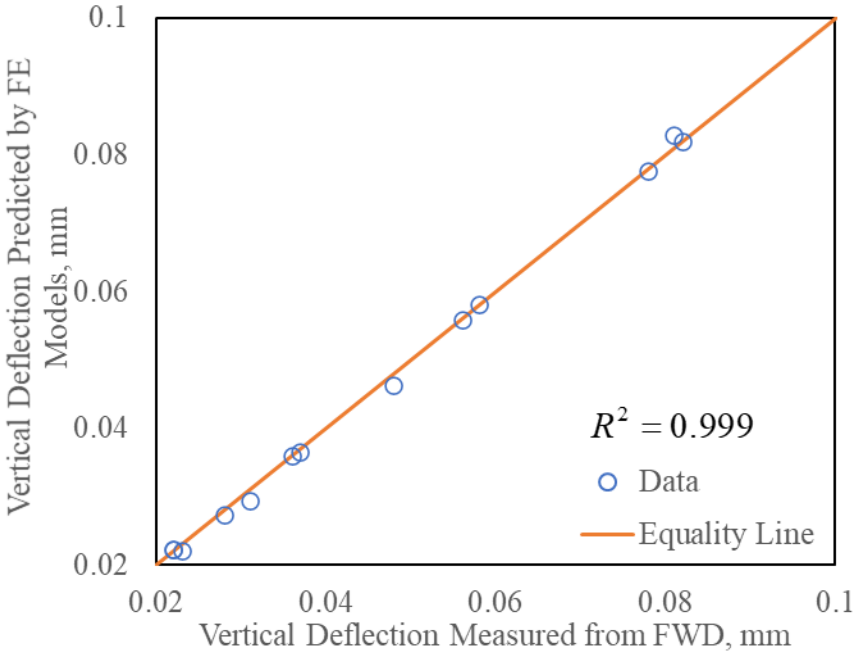


**(d) Section 48-0167 in Step 3**

**Figure 5.9 Continued**

The modulus of the AC layer used in Step 2 is illustrated in Figure 5.2. Figure 5.2 is the master curve constructed from laboratory tests on asphalt mixtures with original binders. These undamaged moduli are supposed to result in predictions with lower accuracy, which can be observed in Figure 5.10. The deterioration of the AC layer reflected on the modulus and then on the surface deflection. The FE model updating takes advantages of these variations in deflections and calibrated damaged moduli.

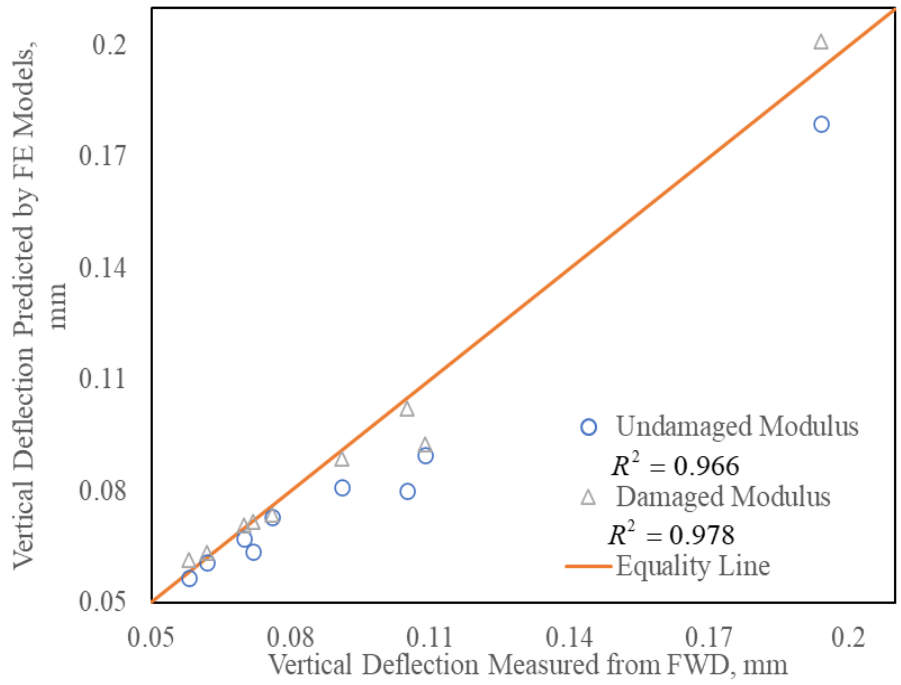


**(a) Section 48-0117**

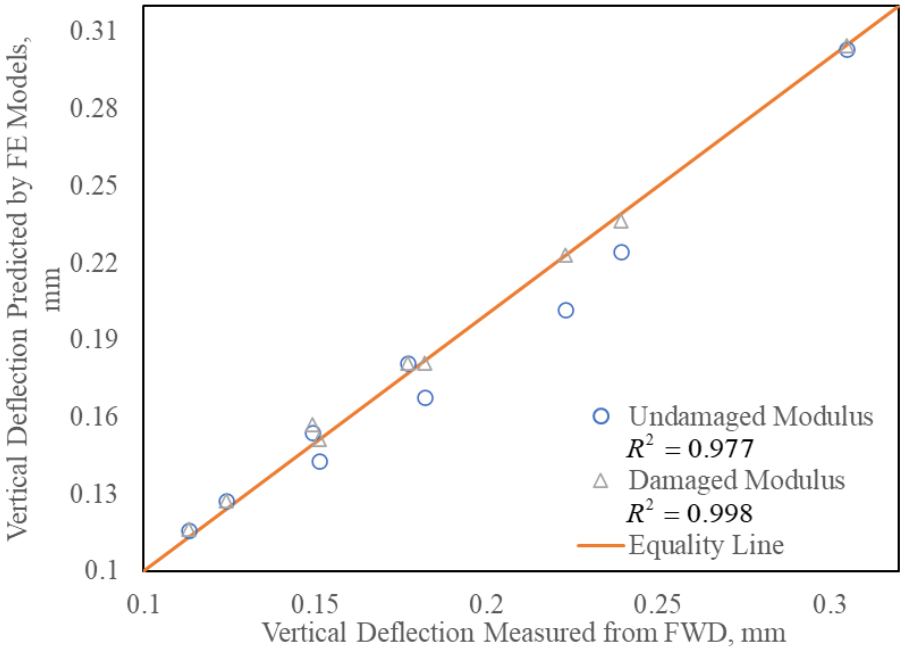


**(b) Section 48-0167**

**Figure 5.10 Validation of AC Layer Moduli from the FE Model Updating**

## 5.5 Average Deterioration Degree

The average deterioration degree is determined from the modulus change in the AC layer between undamaged and damaged moduli. Figure 5.11 shows modulus gradients of undamaged and damaged AC layers under the FWD load and at field temperatures. With effects of the temperature, it is meaningless to directly use or compare these values, which come from tests on different dates. The average deterioration degree is defined in Equation 5.4, which averages deterioration degrees within the AC layer,

$$\varphi = \frac{1}{d}\int_{z=0}^{z=d} \frac{E_d(z) - E_u(z)}{E_u(z)} dz \times 100\% \tag{5.4}$$

where $E_d(z)$ is the damaged modulus at depth z; $E_u(z)$ is the undamaged modulus at depth z; and $d$ is the thickness of the layer. The average deterioration degree

- considers opposite effects of the aging and load-induced fatigue damage on the modulus by keeping the sign of the difference between the damaged and undamaged moduli; and
- eliminates effects of the temperature and frequency on the modulus by dividing the undamaged modulus for the relative difference.

Additionally, the undamaged modulus is calculated from Equation 5.1, which works for laboratory tests, while the damaged modulus is directly calibrated from field tests. Discrepancies between material properties from laboratory and field tests (33) can be also eliminated by using the relative difference.

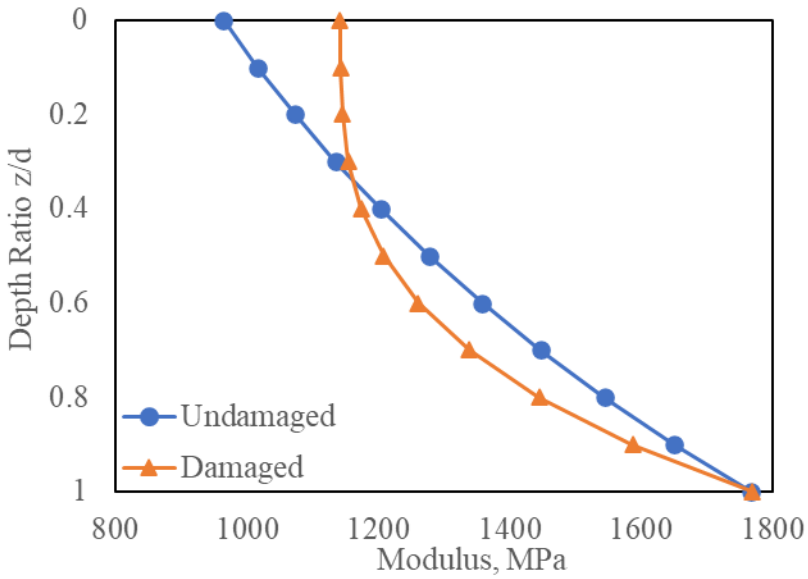


**(a) 1999-8-19**

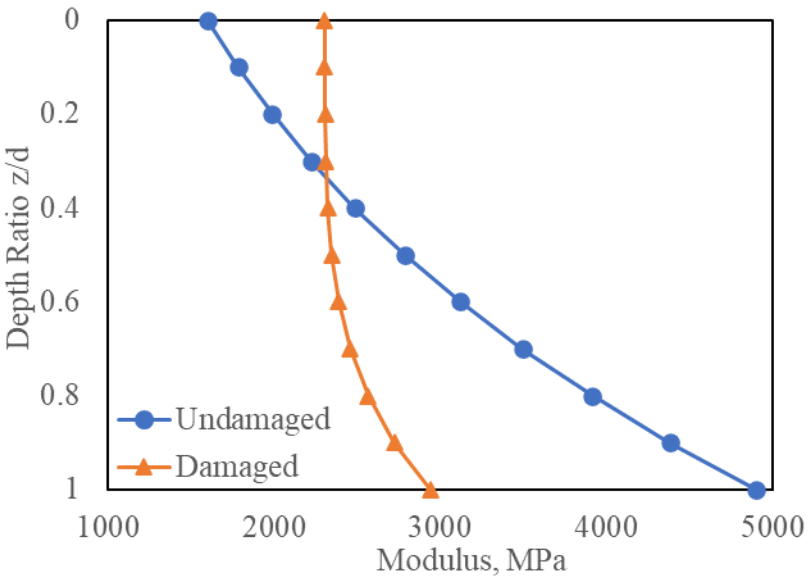


**(b) 2000-5-9**

**Figure 5.11 Comparison of Undamaged and Damaged AC Layer Moduli in Section 48-0167**

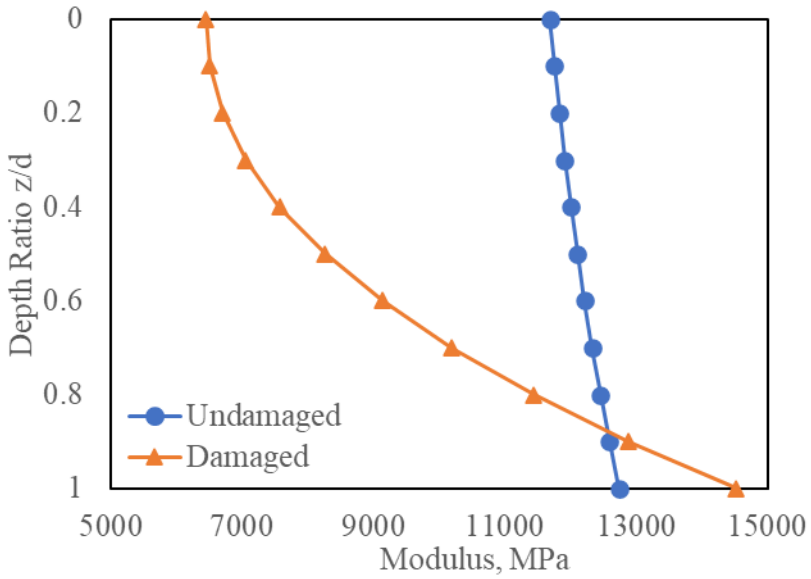


**(c) 2002-2-13**

**Figure 5.11 Continued**

Figure 5.12 shows average deterioration degrees of two pavement sections at different service times. Overall, the major deterioration resultes from load repetitions, which reduce the modulus of the AC layer. Meanwhile, the aging effects can still be explicitly detected from the average deterioration degree of Section 48-0167 in 1999 and the difference between average deterioration degrees of Section 48-0117 in 2000 and 2002. Literatures introduced in the Section 5.1 show the modulus and associated terms are popular in the pavement evaluation and management. However, results in Figure 12(a) indicate the modulus change with the service time is not always consistent. The modulus or associated terms as indicators seems not enough for a comprehensive evaluation of flexible pavements. Consider the limited case number in this section, a

more general relationship between the modulus and deterioration degree of the AC layer is required in the future.

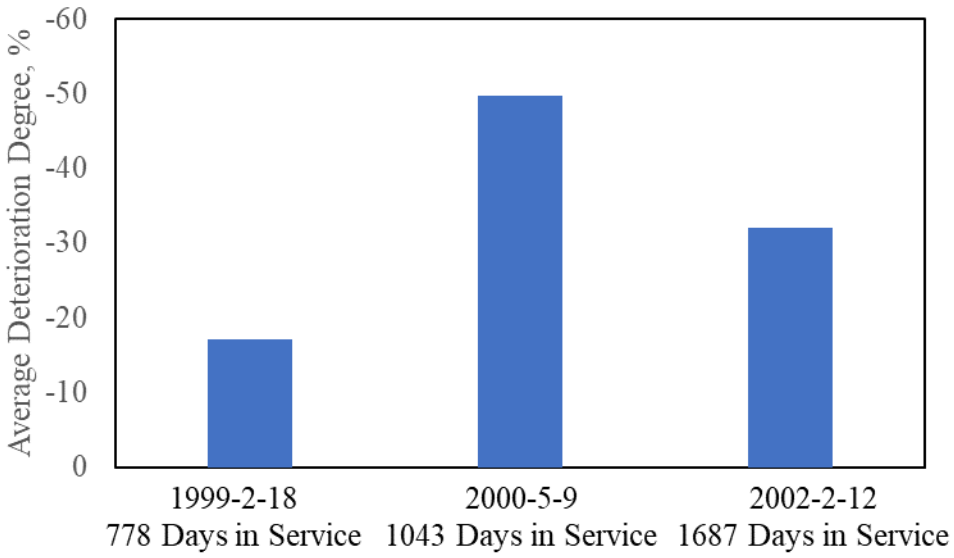


**(a) Section 48-0117**

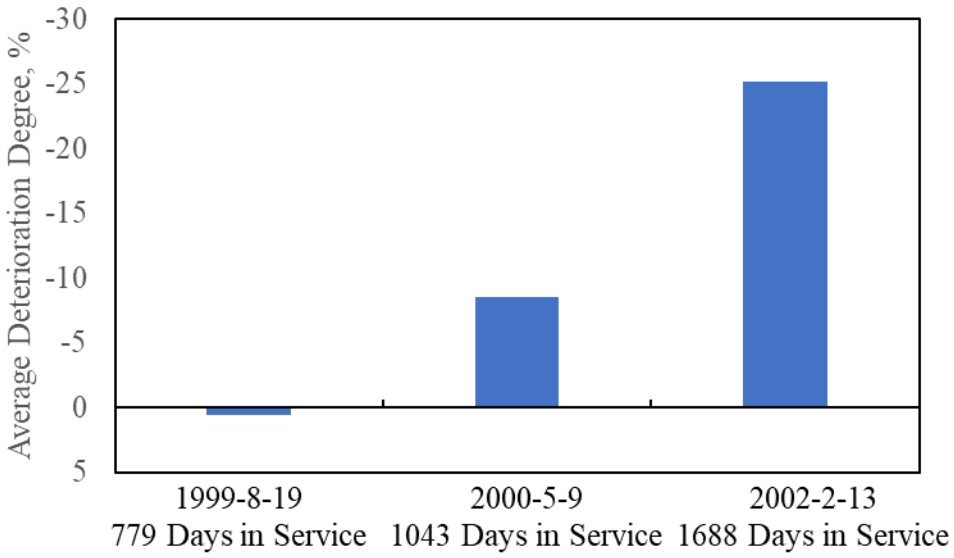


**(b) Section 48-0167**

**Figure 5.12 Average Deterioration Degree with Service Time**

# 6. CONCLUSIONS AND RECOMMENDATIONS

## 6.1 Conclusions

First, this dissertation proposes an AI-based FE model updating method to determine the equivalent stationary dynamic load for the moving load at a specified speed. Four different AI algorithms are introduced and compared for an efficient and intelligent construction of the equivalency between the dynamic load and the moving load. The 2D axisymmetric FE model with the equivalent dynamic load can predict similar pavement responses as the 3D FE model with the moving load. The relationship is also applied in various pavements to check its applicability. The work and findings in this part are summarized as follows.

- The PSO, the GA and their improved algorithms the QPSO, the SSGA-MGA are applied to automatically find the equivalent dynamic load for the moving load. Based on values of the objective function during iterations, two improved algorithms have improved convergence rates at the initiate stage of iterations. The PSO, the GA and the SSGA-MGA have similar and desirable accuracy after a limited number of iterations. Consider the computational efficiency and the algorithm setting, the PSO is selected to deal with the problem in this paper;
- The cycle of the equivalent dynamic load is directly related to the speed of the moving load by a power-law function. The pressure magnitude of the equivalent dynamic load is strictly linear with the contact stress magnitude of the moving

load when the loading areas are specified. The relationship is validated by pavement responses predicted by FE models;

- The relationship between the dynamic load and the moving load is independent of pavement parameters such as the thickness and material properties of supporting layers. As for the material properties of the asphalt layer, further researches are required for their effects on the equivalent relationship.

Next, flexible pavements under moving loads are simulated using FE software ABAQUS. The 3D FE pavement model is constructed and analyzed with different material properties and moving speeds. The work and findings in this part are summarized as follows.

- The 3D FE model under the moving load reveals that the deflection basin of a flexible pavement exhibits an asymmetric shape under the moving load. It has a steep leading edge and a shallow trailing edge along the direction of the moving load;
- The 3D FE model shows that there is a time lag between the maximum deflection and the center of the load for flexible pavements and some rigid pavements. This time lag is utilized to define a new term of "lag angle" following the concept of the phase angle of viscoelastic materials;
- The viscoelasticity of the pavement materials and structural inertial damping of the pavement structure affect the shape and lag angle of the deflection basin. Both of them need to be considered in order to accurately capture the features of the deflection basin under moving loads;

- The speeds of the moving loads influence the shape and lag angle of the deflection basin of pavements. A higher speed results in a higher lag distance between the maximum deflection and the loading center in flexible pavements and some rigid pavements;
- The pavement deterioration conditions affect the shape and lag angle of the deflection basin. As the severity of pavement distresses increases, the time lag of the deflection basin increases. This is attributed to the increasing loss of viscos dissipated energy due to the growing microcracks in the pavement surface layer and the accumulation of moisture and plastic deformation in the base course layer;
- It is found that the lag angle of the deflection basin is closely related to the phase angle of the viscoelastic pavement materials, which indicates the lag angle can be used as an indicator for advanced warning of flexible pavement deterioration in terms of the initiation and propagation of micro-cracks;
- The deflection basin predicted by the 3D FE analysis is compared to the field measurements made with the RWD and TSD. The simulation has the same pavement structure and laboratory-measured material properties as the real pavement tested by the RWD and TSD. Based on the limited RWD and TSD data, the simulation results are comparable to the field deflections obtained at high speed.

Then, a similar method of evaluating the microcracking deterioration condition of flexible pavements is proposed in 2D axisymmetric FE models with equivalent

stationary dynamic loads. A revised FE model updating with the kriging model is applied to construct the equivalent 2D axisymmetric FE model for the 3D FE model. The work and findings in this part are summarized as follows.

- The new FE model updating with the kriging model works as well as the original model updating but with more flexibility. The equivalent relationship between moving loads and stationary dynamic loads are similar to the one obtained from the original model updating;
- The 2D axisymmetric FE model also shows that there is a time lag between the load and deflection peaks. The time lag is used to define the "equivalent lag angle" as the lag angle from 3D FE models with moving loads;
- The deterioration degree of the flexible pavement affects the value of the equivalent lag angle. With the increase of the deterioration severity, the equivalent lag angle increases. The increase of the phase angle of the material is attributed to the initiation and propagation of micro-cracks in the material;
- The speed of the moving load affects the value of the equivalent lag angle. With the increase of the moving speed, the lag angle increases. The causal relationship between the equivalent lag angle, phase angle and moving speed indicates a potential use of the equivalent lag angle to determine the pavement deterioration condition from NDT devices with stationary dynamic loads.

Then, a methodology in obtaining layer properties of flexible pavements using FWD test results and the revised FE model updating is proposed. The complex modulus gradient of the AC layer can be determined and used for the aging degree of the flexible

pavements. Also, the calibrated layer properties are compared with static and dynamic backcalculation softwares. The work and findings in this part are summarized as follows.

- A layer-by-layer calibration scheme is provided based on a sensitivity analysis of layer moduli on pavement surface deflections. It shows layers closer to the pavement surface have weaker effects on locations away from the loading center. Accordingly, the calibration is conducted from pavement bottom to top and each layer is calibrated using specified sensor data;
- The FE model updating with the kriging model and PSO algorithm also works well for the calibration of layer moduli. The performance of the kriging model and PSO algorithm is validated;
- Compared with the static backcalculation software BAKFAA and dynamic backcalculation software DBSID, layer properties obtained from FE model updating better represent field conditions. Besides, FE model updating in this paper can capture the sensitivity of supporting layer moduli to the loading frequency and calibrate a continuous modulus gradient model for the AC layer;
- Complex modulus gradient of the AC layer is obtained in this study, in which the modulus at the top and bottom of the AC layer increase and the gradient shape parameter decreases with the increase of the loading frequency. Same trends were observed in previous researches;
- With fixed testing date and testing location, calibrated complex modulus gradients at different service times can be used to characterize aging effects on flexible pavements and aging degrees of flexible pavements.

Finally, the revised FE model updating is applied in calibrating layer moduli of damaged flexible pavements and determining their deterioration degrees using an open database. Factors affecting flexible pavement behaviors and deterioration degrees are clarified. The work and findings in this part are summarized as follows.

- The revised FE model updating has as desirable performance in the determination of the equivalent frequency spectrum of the FWD load in the AC layer as calibrations of layer moduli;
- The equivalent frequency of the FWD load decreases with the layer depth. For a certain dynamic/moving load, the equivalent frequency spectrum in the AC layer is temperature-independent and structure-dependent;
- In FWD tests, the closer the sensor location is to the loading center, the more the vertical deflection is affected by the upper layers. A two-step calibration method is proposed accordingly and applied successfully;
- The average deterioration degree defined from the comparison between the undamaged and damaged modulus can capture effects of the aging and fatigue damage on the pavement. It also indicates opposite effects of the aging and fatigue damage on the modulus make the modulus change with the service time inconsistent. The modulus used as an indicator for the deterioration degree of the pavement should be accompanied with other indicators or evaluating methods.

## 6.2 Recommendations for Future Research

This dissertation focuses on innovative methodologies in determining deteriorations of flexible pavements. NDT devices, advanced numerical methods, large databases and AI algorithms are applied to achieve this goal. To make this research work completer and more practical, some research directions are recommended.

The relationship between the dynamic load and the moving load provides a potential tool to validate data from field testing devices applying moving loads. Also, the 2D axisymmetric FE pavement model with the equivalent dynamic load can serve as an alternative to the 3D FE pavement model with the moving load. Directions of future researches are summarized as follows.

- Based on the vehicle configuration and the type of collected data, different relationships can be built for different NDT devices such as the RWD and the TSD. The stability and accuracy of these tests can be validated by 2D axisymmetric FE models or FWD tests with modified loading configurations;
- Factors affecting the relationship can be studied such as the viscoelasticity of flexible pavement surfaces and the tire configuration (multi-wheel and multi-axle effects, etc.).

The newly defined lag angle and equivalent lag angle from corresponding NDT devices and FE models can be used to determine the fatigue damage degree of flexible pavements. In addition to the application in the practice, a comprehensive parametric study and sensitivity analysis can be conducted for relationships between lag angle and

equivalent lag angle and pavement parameters such as supporting layer moduli, layer thickness, etc.

Since the complex modulus gradient in the AC layer can be obtained, this method can be applied in FWD tests to determine the aging degree of the pavement. Similar to the relationship between model parameters of the modulus gradient and the loading frequency, the relationship between model parameters, the aging time and environmental conditions can be determined and applied for prediction. As for the average deterioration degree, it can be applied in more pavement sections for general correlations with other indicators.

Last but not the least, as a powerful tool, the FE model updating with the kriging model and AI algorithms can be further applied to deal with other problems in pavement materials and structures, in which such applications are very limited.

# REFERENCES


AASHTO. (1999). *Provisional Standards*. Interim Edition. American Association of State Highway and Transportation Officials, Washington, D.C.

*ABAQUS version 6.12* [Computer software]. (2012). Dassault Systemes, Waltham, MA.

ARA-ERES (Applied Research Associates, Inc., ERES Consultants Division). (2004). Guide for mechanistic–empirical design of new and rehabilitated pavement structures, *Final report, NCHRP Project 1-37A*, Transportation Research Board, Washington, D.C.

ASTM International. (2017). Standard test methods for quantitative extraction of asphalt binder from asphalt mixtures. *D2172/D2172M-17*. West Conshohocken, PA.

Al-Qadi, I. L., Elseifi, M. A., and Yoo, P. J. (2005). Characterization of pavement damage due to different tire configurations. *Journal of the Association of Asphalt Paving Technologists*, 74, 921-962.

Al-Qadi, I. L., Xie, W., and Elseifi, M. A. (2008). Frequency determination from vehicular loading time pulse to predict appropriate complex modulus in MEPDG. *Asphalt Paving Technology-Proceedings*, 77, 739.

Al-Qadi, I. L., and Wang, H. (2009). Pavement damage due to different tire and loading configurations on secondary roads. *NEXTRANS Project No. 008IY01*, NEXTRANS, West Lafayette.

Al-Qadi, I. L., Wang, H., Yoo, P. J., and Dessouky, S. H. (2008). Dynamic analysis and in situ validation of perpetual pavement response to vehicular loading. *Transportation Research Record*, 2087(1), 29-39.

Ameri, M., Yavari, N., and Scullion, T. (2009). Comparison of static and dynamic backcalculation of flexible pavement layers moduli, using four software programs. *Asian Journal of Applied Sciences*, 2(3), 197-210.

Ahmed, T. M., and Khalid, H. A. (2015). A new approach in fatigue testing and evaluation of hot mix asphalt using a dynamic shear rheometer. In *Proc., 6th Int. Conf. on Bituminous Mixtures and Pavements*, pp. 351-359.

BAKFAA. (2017). Retrieved from https://www.airporttech.tc.faa.gov/Products/Airport-Safety-Papers-Publications/Airport-Safety-Detail/ArtMID/3682/ArticleID/11/BAKFAA-version-2101.

Baek, C., Underwood, B. S., and Kim, Y. R. (2012). Effects of oxidative aging on asphalt mixture properties. *Transportation Research Record*, 2296(1), 77-85.

Brill, E. D., Flach, J. M., Hopkins, L. D., and Ranjithan, S. M. G. A. (1990). MGA: A decision support system for complex, incompletely defined problems. *IEEE Transactions on Systems, Man, and Cybernetics*, 20(4), 745-757.

Bergh, F. V. D. (2001). An analysis of particle swarm optimizers. *Doctoral Dissertation*, University of Pretoria, Pretoria, South Africa.

Baugh Jr, J. W., Caldwell, S. C., and Brill Jr, E. D. (1997). A mathematical programming approach for generating alternatives in discrete structural optimization. *Engineering Optimization*, 28(1-2), 1-31.

Boudabbous, M., Millien, A., Petit, C., and Neji, J. (2013). Energy approach for the fatigue of thermoviscoelastic materials: application to asphalt materials in pavement surface layers. *International Journal of Fatigue*, 47, 308-318.

Bonaquist, R. (2008). Refining the simple performance tester for use in routine practice. *No. NCHRP Project 9-29*, National Cooperative Highway Research Program, Transportation Research Board of the National Academies, Washington, D.C.

Barksdale, R. D. (1971). Compressive stress pulse times in flexible pavements for use in dynamic testing. *Highway Research Record*, 345(4), 32-44.

Brown, S. F. (1973). Determination of Young's modulus for bituminous materials in pavement design. *Highway Research Record*, 431.

Buttlar, W. G., Paulino, G. H., and Song, S. H. (2006). Application of graded finite elements for asphalt pavements. *Journal of Engineering Mechanics*, 132(3), 240-249.

Cocurullo, A., Airey, G. D., Collop, A. C., and Sangiorgi, C. (2008). Indirect tensile versus two-point bending fatigue testing. In *Proceedings of the Institution of Civil Engineers-Transport*, Vol. 161, No. 4, pp. 207-220, Thomas Telford Ltd.

Collop, A. C., and Cebon, D. (1996). Stiffness reductions of flexible pavements due to cumulative fatigue damage. *Journal of Transportation Engineering*, 122(2), 131-139.

Crook, A. L., Montgomery, S. R., and Guthrie, W. S. (2012). Use of falling weight deflectometer data for network-level flexible pavement management. *Transportation Research Record*, 2304(1), 75-85.

Caicedo, J. M., and Yun, G. (2011). A novel evolutionary algorithm for identifying multiple alternative solutions in model updating. *Structural Health Monitoring*, 10(5), 491-501.

Carlson, P., Storey, B., Poorsartep, M., Stevens, C., Ettelman, B., Lindheimer, T.E., Dastgiri, M., Khodakarami, A., Miles, J., Song, D. and Lytton, R.L. (2017). Advancing innovative high-speed remote-sensing highway infrastructure assessment using emerging technologies: technical report (*No. FHWA/TX-16/0-6869-1*). Texas A&M Transportation Institute.

Carpenter, S. H., Ghuzlan, K. A., and Shen, S. (2003). Fatigue endurance limit for highway and airport pavements. *Transportation Research Record*, 1832(1), 131-138.

Dave, E. V., Buttlar, W. G., Paulino, G. H., and Hilton, H. H. (2008). Graded viscoelastic approach for modeling asphalt concrete pavements. In *AIP Conference Proceedings*, Vol. 973, No. 1, pp. 736-741. American Institute of Physics.

Dave, E. V., Buttlar, W. G., and Paulino, G. H. (2010). Asphalt pavement aging and temperature dependent properties through a functionally graded viscoelastic model, part-II: Applications. In *Materials Science Forum*, Vol. 631, pp. 53-58. Trans Tech Publications Ltd.

Di Benedetto, H., de La Roche, C., Baaj, H., Pronk, A., and Lundstrom, R. (2003). Fatigue of bituminous mixtures: different approaches and RILEM group contribution. In *Sixth International RILEM Symposium on Performance Testing and Evaluation of Bituminous Materials*, pp. 15-38. RILEM Publications SARL.

Di Benedetto, H., Nguyen, Q. T., and Sauzéat, C. (2011). Nonlinearity, heating, fatigue and thixotropy during cyclic loading of asphalt mixtures. *Road Materials and Pavement Design*, 12(1), 129-158.

De Beer, M., Fisher, C., and Jooste, F. J. (2002). Evaluation of non-uniform tyre contact stresses on thin asphalt pavements. In *Ninth International Conference on Asphalt Pavements*, Vol. 5, pp. 19-22.

Das, P. K., Kringos, N., and Birgisson, B. (2015). Numerical study on the effect of mixture morphology on long-term asphalt mixture ageing. *International Journal of Pavement Engineering*, 16(8), 710-720.

Deng, Y. (2017). Three-dimensional numerical simulation of pavements deflection basins under moving loads, *Master Thesis*, Texas A&M University, College Station.

Deng, Y., Luo, X., Gu, F., Zhang, Y., and Lytton, R. L. (2019). 3D simulation of deflection basin of pavements under high-speed moving loads. *Construction and Building Materials*, 226, 868-878.

Elseifi, M. A., Abdel-Khalek, A. M., Gaspard, K., Zhang, Z., and Ismail, S. (2011). Evaluation of continuous deflection testing using the rolling wheel deflectometer in Louisiana. *Journal of Transportation Engineering*, 138(4), 414-422.

Elseifi, M. A., Gaspard, K., Wilke, P. W., Zhang, Z., and Hegab, A. (2015). Evaluation and validation of a model for predicting pavement structural number with rolling wheel deflectometer data. *Transportation Research Record*, 2525(1), 13-19.

Elbagalati, O., Elseifi, M. A., Gaspard, K., and Zhang, Z. (2016). Prediction of in-service pavement structural capacity based on traffic-speed deflection measurements. *Journal of Transportation Engineering*, 142(11), 04016058.

Elbagalati, O., Elseifi, M. A., Gaspard, K., and Zhang, Z. (2017). Implementation of the Structural Condition Index into the Louisiana Pavement Management System Based on Rolling Wheel Deflectometer Testing. *Transportation Research Record*, 2641(1): 39-47.

Eberhart, R., and Kennedy, J. (1995). Particle swarm optimization. In *Proceedings of the IEEE International Conference on Neural Networks*, Vol. 4, pp. 1942-1948.

Fernando, E. G., and Liu, W. (1999). *User's Manual for Pavement Dynamic Back-Calculation Procedure with Systems Identification Method (DBSID)*. Texas Transportation Institute, Texas A&M University, College Station, Texas.

Flintsch, G. W., Ferne, B., Diefenderfer, B., Katicha, S., Bryce, J., and Nell, S. (2012). Evaluation of traffic-speed deflectometers. *Transportation Research Record*, 2304(1), 37-46.

Friswell, M., and Mottershead, J. E. (2013). *Finite element model updating in structural dynamics* (Vol. 38). Springer Science & Business Media, Berlin, Germany.

Gandomi, A. H., Yang, X. S., Talatahari, S., and Alavi, A. H. (2013). *Metaheuristic applications in structures and infrastructures*. Newnes, London, UK.

Gedafa, D., Hossain, M., Miller, R., and Steele, D. (2012). Surface Deflections of Perpetual Pavement Sections. In *Pavement Performance: Current Trends, Advances, and Challenges*. ASTM International.

Gu, F., Luo, X., Luo, R., Lytton, R. L., Hajj, E. Y., and Siddharthan, R. V. (2016). Numerical modeling of geogrid-reinforced flexible pavement and corresponding validation using large-scale tank test. *Construction and Building Materials*, 122, 214-230.

Gu, F., Ma, W., West, R. C., Taylor, A. J., and Zhang, Y. (2019). Structural performance and sustainability assessment of cold central-plant and in-place recycled asphalt pavements: A case study. *Journal of Cleaner Production*, 208, 1513-1523.

Gillespie, T. D. (1992). *Fundamentals of vehicle dynamics*. Society of Automotive Engineers (SAE).

Hagos, E. T. (2008). The effect of aging on binder properties of porous asphalt concrete. *PhD Dissertation*. Delft University of Technology, Delft, Netherlands.

Hao, H., and Xia, Y. (2002). Vibration-based damage detection of structures by genetic algorithm. *Journal of Computing in Civil Engineering*, 16(3), 222-229.

Howard, I. L., and Warren, K. A. (2009). Finite-element modeling of instrumented flexible pavements under stationary transient loading. *Journal of Transportation Engineering*, 135(2), 53-61.

Holland, J. H. (1992). *Adaptation in natural and artificial systems: an introductory analysis with applications to biology, control, and artificial intelligence*. MIT press, Cambridge, MA.

Hardy, M. S. A., and Cebon, D. (1994). Importance of speed and frequency in flexible pavement response. *Journal of Engineering Mechanics*, 120(3), 463-482.

Hadidi, R., and Gucunski, N. (2010). Comparative study of static and dynamic falling weight deflectometer back-calculations using probabilistic approach. *Journal of Transportation Engineering*, 136(3), 196-204.

Han, R., Jin, X., and Glover, C. J. (2011). Modeling pavement temperature for use in binder oxidation models and pavement performance prediction. *Journal of Materials in Civil Engineering*, 23(4), 351-359.

Hu, W. (2018). Evaluation of intelligent compaction technology in asphalt pavement construction and laboratory compaction. *PhD Dissertation*. University of Tennessee, Knoxville.

Herr, W. J., Hall, J. W., White, T. D., and Johnson, W. (1995). Continuous deflection basin measurement and backcalculation under a rolling wheel load using scanning laser technology. *Proc., ASCE 1995 Transportation Congress*, Vol. 1 and 2, San Diego, California, pp. 600–611.

Houston, W. N., Mirza, M. W., Zapata, C. E., and Raghavendra, S. (2005). Environmental effects in pavement mix and structural design systems. *NCHRP Project 9-23*. TRB, National Research Council, Washington, D.C.

Huang, Y. H. (2004). *Pavement analysis and design*. Pearson/Prentice Hall, Upper Saddle River, NJ.

Khazanovich, L., and Booshehrian, A. (2015). Dynamic viscoelastic analysis of falling weight deflectometer deflections for rigid and flexible pavements. *Transportation Research Record*, 2525(1), 31-39.

Kim, M. (2007). Three-dimensional finite element analysis of flexible pavements considering nonlinear pavement foundation behavior. *PhD Dissertation*. University of Illinois, Urbana-Champaign, Urbana, IL.

Kutay, M. E., Chatti, K., and Lei, L. (2011). Backcalculation of dynamic modulus mastercurve from falling weight deflectometer surface deflections. *Transportation Research Record*, 2227(1), 87-96.

Kondner, R. L., and Ho, M. M. (1965). Viscoelastic response of a cohesive soil in the frequency domain. *Transactions of the Society of Rheology*, 9(2), 329-342.

Katicha, S. W., Flintsch, G. W., Ferne, B., and Bryce, J. (2014). Limits of agreement method for comparing TSD and FWD measurements. *International Journal of Pavement Engineering*, 15(6), 532-541.

Kim, Y. R., Hibbs, B. O., and Lee, Y. C. (1995). Temperature correction of deflections and backcalculated asphalt concrete moduli. *Transportation Research Record*, (1473).

Kim, Y. R., Little, D. N., and Lytton, R. L. (2003). Fatigue and healing characterization of asphalt mixtures. *Journal of Materials in Civil Engineering*, 15(1), 75-83.

Koohi, Y., Lawrence, J. J., Luo, R., and Lytton, R. L. (2012). Complex stiffness gradient estimation of field-aged asphalt concrete layers using the direct tension test. *Journal of Materials in Civil Engineering*, 24(7), 832-841.

Loulizi, A., Al-Qadi, I. L., Lahouar, S., and Freeman, T. E. (2002). Measurement of vertical compressive stress pulse in flexible pavements: representation for dynamic loading tests. *Transportation Research Record*, 1816(1), 125-136.

Loughlin, D. H., Ranjithan, S. R., Brill Jr, E. D., and Baugh Jr, J. W. (2001). Genetic algorithm approaches for addressing unmodeled objectives in optimization problems. *Engineering Optimization*, 33(5), 549-569.

Levenberg, E., Pettinari, M., Baltzer, S., and Christensen, B. M. L. (2018). Comparing traffic speed deflectometer and falling weight deflectometer data. *Transportation Research Record*, 2672(40), 22-31.

Leiva-Villacorta, F., and Timm, D. (2013). Falling weight deflectometer loading pulse duration and its effect on predicted pavement responses. In *Transportation Research Board 92nd Annual Meeting*, Washington DC, United States.

Ling, M., Luo, X., Gu, F., and Lytton, R. L. (2017a). Time-temperature-aging-depth shift functions for dynamic modulus master curves of asphalt mixtures. *Construction and Building Materials*, 157, 943-951.

Ling, M., Luo, X., Gu, F., and Lytton, R. L. (2017b). An inverse approach to determine complex modulus gradient of field-aged asphalt mixtures. *Materials and Structures*, 50(2), 138.

Ling, M., Luo, X., Hu, S., Gu, F., and Lytton, R. L. (2017c). Numerical modeling and artificial neural network for predicting J-integral of top-down cracking in asphalt pavement. *Transportation Research Record*, 2631(1), 83-95.

Ling, M., Chen, Y., Hu, S., Luo, X., and Lytton, R. L. (2019a). Enhanced model for thermally induced transverse cracking of asphalt pavements. *Construction and Building Materials*, 206, 130-139.

Ling, M., Luo, X., Chen, Y., Hu, S., and Lytton, R. L. (2019b). A calibrated mechanics-based model for top-down cracking of asphalt pavements. *Construction and Building Materials*, 208, 102-112.

Ling, M., Luo, X., Chen, Y., Gu, F., and Lytton, R. L. (2020). Mechanistic-empirical models for top-down cracking initiation of asphalt pavements. *International Journal of Pavement Engineering*, 21(4), 464-473.

Li, M., and Wang, H. (2019). Development of ANN-GA program for backcalculation of pavement moduli under FWD testing with viscoelastic and nonlinear parameters. *International Journal of Pavement Engineering*, 20(4), 490-498.

Li, M., Wang, H., Xu, G., and Xie, P. (2017). Finite element modeling and parametric analysis of viscoelastic and nonlinear pavement responses under dynamic FWD loading. *Construction and Building Materials*, 141, 23-35.

Lu, P., Chen, S., and Zheng, Y. (2012). Artificial intelligence in civil engineering. *Mathematical Problems in Engineering*, vol. 2012.

Luo, R., and Lytton, R. L. (2010). Characterization of the tensile viscoelastic properties of an undamaged asphalt mixture. *Journal of Transportation Engineering*, 136(3), 173-180.

Lytton, R. L. (1989). Backcalculation of pavement layer properties. In *Nondestructive Testing of Pavements and Backcalculation of Moduli*. ASTM International.

Lytton, R. L., Luo, X., Ling, M., Chen, Y., Hu, S., and Gu, F. (2018). A mechanistic–empirical model for top–down cracking of asphalt pavements layers, *No. NCHRP Project 01-52*, National Cooperative Highway Research Program, Transportation Research Board of the National Academies, Washington, D.C.

Lakes, R. S. (2009). *Viscoelastic materials*. Cambridge University Press, New York.

Li, S., Guo, Z., and Yang, Y. (2016). Dynamic viscoelastic response of an instrumented asphalt pavement under various axles with non-uniform stress distribution. *Road Materials and Pavement Design*, 17(2), 446-465.

Lee, S. J., Amirkhanian, S. N., and Kim, K. W. (2009). Laboratory evaluation of the effects of short-term oven aging on asphalt binders in asphalt mixtures using HP-GPC. *Construction and Building Materials*, 23(9), 3087-3093.

Liu, W., and Scullion, T. (2001). Modulus 6.0 for Windows: User's manual. *No. FHWA/TX-05/0-1869-2*. Texas Transportation Institute, Texas A&M University System.

Luo, X., Birgisson, B., and Lytton, R. L. (2020). Kinetics of healing of asphalt mixtures. *Journal of Cleaner Production*, 252, 119790.

Luo, X., Gu, F., Ling, M., and Lytton, R. L. (2018a). Review of mechanistic-empirical modeling of top-down cracking in asphalt pavements. *Construction and Building Materials*, 191, 1053-1070.

Luo, X., Gu, F., and Lytton, R. L. (2015). Prediction of field aging gradient in asphalt pavements. *Transportation Research Record*, 2507(1), 19-28.

Luo, X., Gu, F., and Lytton, R. L. (2019). Kinetics-based aging prediction of asphalt mixtures using field deflection data. *International Journal of Pavement Engineering*, 20(3), 287-297.

Luo, X., Gu, F., Zhang, Y., Lytton, R. L., and Birgisson, B. (2018b). Kinetics-based aging evaluation of in-service recycled asphalt pavement. *Journal of Cleaner Production*, 200, 934-944.

Li, Y., and Nazarian, S. (1995). Evaluation of aging of hot-mix asphalt using wave propagation techniques. In *Engineering Properties of Asphalt Mixtures and the Relationship to Their Performance*. ASTM International.

Liu, Y., Wang, D. J., Ma, J., and Li, Y. (2014). Performance comparison of two meta-model for the application to finite element model updating of structures. *Journal of Harbin Institute Technology*, 21, 68-78.

Li, Z., Dufalla, N., Mu, F., and Vandenbossche, J. M. (2013). Bonded concrete overlay of asphalt pavements mechanistic-empirical design guide (BCOA-ME). User's Guide, *FHWA TFP Study*, 5, 165.

Magnuson, A. H. (1988). Dynamic analysis of falling-weight deflectometer data. *Report No. TX-89/1175-1*. Texas Transportation Institute, Texas A&M University System, College Station, Texas.

Magnuson, A. H., Lytton, R. L., and Briggs, R. C. (1991). Comparison of computer predictions and field data for dynamic analysis of falling weight deflectometer data. *Transportation Research Record*, 1293.

McLean, D. B. (1974). Permanent deformation characteristics of asphalt concrete. *PhD Dissertation*. University of California, Berkeley.

Maser, K., Schmalzer, P., Shaw, W., and Carmichael, A. (2017). Integration of traffic speed deflectometer and ground-penetrating radar for network-level roadway structure evaluation. *Transportation Research Record*, 2639(1), 55-63.

Mohammad, L. N., Nazzal, M. D., King, B., and Austin, A. (2013). Development of a design methodology for asphalt treated mixtures. *No. FHWA/LA. 09/453*. Louisiana Department of Transportation and Development.

McKay, M. D., Beckman, R. J., and Conover, W. J. (1979). Comparison of three methods for selecting values of input variables in the analysis of output from a computer code. *Technometrics*, 21(2), 239-245.

Mirza, M. W. and Witczak, M. W. (1995). Development of a global aging system for short and long term aging of asphalt cements. *Journal of the Association of Asphalt Paving Technologists*, 64, 393–430.

Moreno-Navarro, F., and Rubio-Gámez, M. C. (2016). A review of fatigue damage in bituminous mixtures: Understanding the phenomenon from a new perspective. *Construction and Building Materials*, 113, 927-938.

Mulungye, R. M., Owende, P. M. O., and Mellon, K. (2005). Analysis of response of flexible pavements using finite element method. *The ITB Journal*, 6(2), 5.

Meier, R. W. and Rix, G. J., Backcalculation of flexible pavement moduli using artificial neural networks. (1994). *Transportation Research Record*, 1448, National Research Council, Washington D.C.

Madsen, S. S., and Pedersen, N. L. (2019). Backcalculation of raptor (RWD) measurements and forward prediction of FWD deflections compared with FWD measurements. In *International Airfield and Highway Pavements Conference 2019*, pp. 382-391. American Society of Civil Engineers.

Martin, T. C. (2011). Experimental estimation of the relative deterioration of flexible pavements under increased axle loads. *International Journal of Pavement Engineering*, 12(1), 37-45.

Muller, W. B., and Roberts, J. (2013). Revised approach to assessing traffic speed deflectometer data and field validation of deflection bowl predictions. *International Journal of Pavement Engineering*, 14(4), 388-402.

Nasimifar, M., Thyagarajan, S., Siddharthan, R. V., and Sivaneswaran, N. (2016). Robust deflection indices from traffic-speed deflectometer measurements to predict critical pavement responses for network-level pavement management system application. *Journal of Transportation Engineering*, 142(3), 04016004.

Nasimifar, M., Siddharthan, R. V., Rada, G. R., and Nazarian, S. (2017). Dynamic analyses of traffic speed deflection devices. *International Journal of Pavement Engineering*, 18(5), 381-390.

Nazarian, S., and Alvarado, G. (2006). Impact of temperature gradient on modulus of asphaltic concrete layers. *Journal of Materials in Civil Engineering*, 18(4), 492-499.

Oliver, J. W. (2009). Changes in the chemical composition of Australian bitumens. *Road Materials and Pavement Design*, 10(3), 569-586.

Omkar, S. N., Khandelwal, R., Ananth, T. V. S., Naik, G. N., and Gopalakrishnan, S. (2009). Quantum behaved Particle Swarm Optimization (QPSO) for multi-objective design optimization of composite structures. *Expert Systems with Applications*, 36(8), 11312-11322.

Pronk, A. C., and Hopman, P. C. (1991). Energy dissipation: the leading factor of fatigue. In *Highway Research: Sharing the Benefits*, pp. 255-267. Thomas Telford Publishing.

Petersen, J. C., Branthaver, J. F., Robertson, R. E., Harnsberger, P. M., Duvall, J. J., and Ensley, E. K. (1993). Effects of physicochemical factors on asphalt oxidation kinetics. *Transportation Research Record*, (1391).

Poulikakos, L. D., Pittet, M., Dumont, A. G., and Partl, M. N. (2015). Comparison of the two-point bending and four-point bending test methods for aged asphalt concrete field samples. *Materials and Structures*, 48(9), 2901-2913.

Qabur, A. (2018). Fatigue characterization of asphalt mixes with polymer modified asphalt cement, *Master Thesis*, University of Waterloo, Waterloo, Ontario, Canada.

Qin, J. (2010). Predicting flexible pavement structural response using falling weight deflectometer deflections, *Master Thesis*, Ohio University, Athens, OH.

Qin, S., Zhou, Y. L., Cao, H., and Wahab, M. A. (2018a). Model updating in complex bridge structures using kriging model ensemble with genetic algorithm. *KSCE Journal of Civil Engineering*, 22(9), 3567-3578.

Qin, S., Zhang, Y., Zhou, Y. L., and Kang, J. (2018b). Dynamic model updating for bridge structures using the kriging model and PSO algorithm ensemble with higher vibration modes. *Sensors*, 18(6), 1879.

Rada, G. R., Nazarian, S., Visintine, B. A., Siddharthan, R. V., and Thyagarajan, S. (2016). Pavement structural evaluation at the network level. *No. FHWA-HRT-15-074*. United States. Federal Highway Administration. Office of Infrastructure Research and Development.

Reese, R. (1997). Properties of aged asphalt binder related to asphalt concrete fatigue life. *Journal of the Association of Asphalt Paving Technologists*, 66.

Susanna, A., Crispino, M., Giustozzi, F., and Toraldo, E. (2017). Deterioration trends of asphalt pavement friction and roughness from medium-term surveys on major Italian roads. *International Journal of Pavement Research and Technology*, 10(5), 421-433.

Sangghaleh, A., Pan, E., Green, R., Wang, R., Liu, X., and Cai, Y. (2014). Backcalculation of pavement layer elastic modulus and thickness with measurement errors. *International Journal of Pavement Engineering*, 15(6), 521-531.

Sebaaly, B. E., Mamlouk, M. S., and Davies, T. G. (1986). Dynamic analysis of falling weight deflectometer data. *Transportation Research Record*, 1070, 63-68.

Steele, D. A., and Vavrik, W. R. (2004). Rolling wheel deflectometer (RWD) demonstration and comparison to other devices in Texas. *ARA Project, 15874*.

Shabbir, F., and Omenzetter, P. (2015). Particle swarm optimization with sequential niche technique for dynamic finite element model updating. *Computer-Aided Civil and Infrastructure Engineering*, 30(5), 359-375.

Syswerda, G. (1991). A study of reproduction in generational and steady-state genetic algorithms. In *Foundations of Genetic Algorithms*, Vol. 1, pp. 94-101. Elsevier.

Sun, J., Feng, B., and Xu, W. (2004a). Particle swarm optimization with particles having quantum behavior. In *Proceedings of the 2004 Congress on Evolutionary Computation*, IEEE Cat. No. 04TH8753, Vol. 1, pp. 325-331. IEEE.

Sadeghi, J. M., and Fathali, M. (2007). Deterioration analysis of flexible pavements under overweight vehicles. *Journal of Transportation Engineering*, 133(11), 625-633.

Sun, J., Xu, W., and Feng, B. (2004b). A global search strategy of quantum-behaved particle swarm optimization. In *IEEE Conference on Cybernetics and Intelligent Systems*, Vol. 1, pp. 111-116. IEEE.

Saltan, M., Terzi, S., and Küçüksille, E. U. (2011). Backcalculation of pavement layer moduli and Poisson's ratio using data mining. *Expert Systems with Applications*, 38(3), 2600-2608.

Serrano, N. M. B., Nieto, P. J. G., Sánchez, A. S., Lasheras, F. S., and Fernández, P. R. (2018). A Hybrid algorithm for the assessment of the influence of risk factors in the development of upper limb musculoskeletal disorders. In *International Conference on Hybrid Artificial Intelligence Systems*, pp. 634-646. Springer, Cham.

Schmalzer, P. N. (2006). LTPP manual for falling weight deflectometer measurements, version 4.1. *Report No. FHWA-HRT-06-132*, Federal Highway Administration, US Department of Transportation.

Soren, R., Lisbeth, A., Susanne, B., and Jorgen, K. (2008). A comparison of two years of network level measurements with the Traffic Speed Deflectometer. In *2nd European Transport Research Arena*, Ljubljana.

Shen, S., Airey, G. D., Carpenter, S. H., and Huang, H. (2006). A dissipated energy approach to fatigue evaluation. *Road Materials and Pavement Design*, 7(1), 47-69.

The Dynatest Group. (2001). *ELMOD pavement evaluation manual* (Version 4.5), Dynatest, Denmark.

Tapsoba, N., Sauzéat, C., and Benedetto, H. D. (2012). Analysis of fatigue test for bituminous mixtures. *Journal of Materials in Civil Engineering*, 25(6), 701-710.

Tapsoba, N., Sauzéat, C., Di Benedetto, H., Baaj, H., and Ech, M. (2015). Three-dimensional analysis of fatigue tests on bituminous mixtures. *Fatigue & Fracture of Engineering Materials & Structures*, 38(6), 730-741.

Terzi, S., Saltan, M., Küçüksille, E. U., and Karaşahin, M. (2013). Backcalculation of pavement layer thickness using data mining. *Neural Computing and Applications*, 23(5), 1369-1379.

Ulloa, A., Hajj, E. Y., Siddharthan, R. V., and Sebaaly, P. E. (2013). Equivalent loading frequencies for dynamic analysis of asphalt pavements. *Journal of Materials in Civil Engineering*, 25(9), 1162-1170.

Uzan, J. (1994). Dynamic linear back calculation of pavement material parameters. *Journal of Transportation Engineering*, 120(1), 109-126.

Uddin, W., Zhang, D., and Fernandez, F. (1994). Finite element simulation of pavement discontinuities and dynamic load response. *Transportation Research Record*, (1448).

Varma, S., and Kutay, M. E. (2016). Backcalculation of viscoelastic and nonlinear flexible pavement layer properties from falling weight deflections. *International Journal of Pavement Engineering*, 17(5), 388-402.

Wang, H., and Al-Qadi, I. L. (2009). Combined effect of moving wheel loading and three-dimensional contact stresses on perpetual pavement responses. *Transportation Research Record*, 2095(1), 53-61.

Wang, H., and Al-Qadi, I. L. (2010a). Impact quantification of wide-base tire loading on secondary road flexible pavements. *Journal of Transportation Engineering*, 137(9), 630-639.

Wang, H., and Al-Qadi, I. L. (2010b). Near-surface pavement failure under multiaxial stress state in thick asphalt pavement. *Transportation Research Record*, 2154(1), 91-99.

Wang, H., and Al-Qadi, I. L. (2012). Importance of nonlinear anisotropic modeling of granular base for predicting maximum viscoelastic pavement responses under moving vehicular loading. *Journal of Engineering Mechanics*, 139(1), 29-38.

Wang, H., and Li, M. (2016). Comparative study of asphalt pavement responses under FWD and moving vehicular loading. *Journal of Transportation Engineering*, 142(12), 04016069.

Yin, F., Martin, A. E., Arámbula-Mercado, E., and Newcomb, D. (2017). Characterization of non-uniform field aging in asphalt pavements. *Construction and Building Materials*, 153, 607-615.

Yoo, P. J. and Al-Qadi, I. L. (2008). The truth and myth of fatigue cracking potential in hot-mix asphalt: numerical analysis and validation. *Asphalt Paving Technology-Proceedings*, 77, 549.

Yang, Z. L., Wu, A., and Min, H. Q. (2015). An improved quantum-behaved particle swarm optimization algorithm with elitist breeding for unconstrained optimization. *Computational Intelligence and Neuroscience*, 41.

Zofka, A., Sudyka, J., Maliszewski, M., Harasim, P., and Sybilski, D. (2014). Alternative approach for interpreting traffic speed deflectometer results. *Transportation Research Record*, 2457(1), 12-18.

Zapata, C. E., and Houston, W. N. (2008). Calibration and validation of the enhanced integrated climatic model for pavement design. *NCHRP Report 602*. TRB, National Research Council, Washington, D.C.

Zhang, D., Birgisson, B., Luo, X., and Onifade, I. (2019a). A new short-term aging model for asphalt binders based on rheological activation energy. *Materials and Structures*, 52(4), 68.

Zhang, D., Birgisson, B., Luo, X., and Onifade, I. (2019b). A new long-term aging model for asphalt pavements using morphology-kinetics based approach. *Construction and Building Materials*, 229, 117032.

Zhou, F., Newcomb, D., Gurganus, C., Banihashemrad, S., Park, E. S., Sakhaeifar, M., and Lytton, R. L. (2016). Experimental design for field validation of laboratory tests to assess cracking resistance of asphalt mixtures. *No. NCHRP Project 9-57*, National Cooperative Highway Research Program, Transportation Research Board of the National Academies, Washington, D.C.

Zaghloul, S. M., and White, T. (1993). Use of a three-dimensional, dynamic finite element program for analysis of flexible pavement. *Transportation Research Record*, (1388).

Zhang, Y., Birgisson, B., and Lytton, R. L. (2016). Weak form equation–based finite-element modeling of viscoelastic asphalt mixtures. *Journal of Materials in Civil Engineering*, 28(2), 04015115.

Zhang, Y., Gu, F., Luo, X., Birgisson, B., and Lytton, R. L. (2018). Modeling stress-dependent anisotropic elastoplastic unbound granular base in flexible pavements. *Transportation Research Record*, 2672(52), 46-56.

Zhang, Z., Manuel, L., Damnajanovic, I., and Li, Z. (2003). Development of a new methodology for characterizing pavement structural condition for network level applications. *Report No. FHWA/TX-04/0-4322-1*, Center for Transportation Research, University of Texas at Austin, Austin, TX.